Copyright

by

Marshall Caleb Johnson

2016

The Dissertation Committee for Marshall Caleb Johnson certifies that
this is the approved version of the following dissertation:

Spin-Orbit Misalignments, Planet Candidate Validation, and Nodal Precession via Doppler Tomography

Committee:

William D. Cochran, Supervisor

Andrew Collier Cameron

Michael Endl

Edward L. Robinson

Chris Sneden

Spin-Orbit Misalignments, Planet Candidate Validation, and Nodal Precession via Doppler Tomography

by

Marshall Caleb Johnson, B.A., M.A.

Dissertation

Presented to the Faculty of the Graduate School of
The University of Texas at Austin
in Partial Fulfillment
of the Requirements
for the degree of

Doctor of Philosophy

The University of Texas at Austin
August, 2016

Dedicated to my grandparents

Maxine and Walter Goad

who helped to set me on my current path

in so many ways.

Acknowledgments

I would like to begin by thanking my advisor, Bill Cochran. I still distinctly remember sitting down to talk with you as a prospective graduate student, and hearing about this Doppler tomography project with interest. It was thanks to your encouragement and support that I was able to take on this project, run with it, and really make it my own. You gave me the room to figure things out on my own, but at the same time you were always there if I needed help. Working with you has been a great pleasure, and I hope that our collaborations will continue for many years in the future. Thank you.

Thanks to my committee members–Mike Endl, Rob Robinson, Chris Sneden, Sally Dodson-Robinson (2012-13), and Andrew Collier Cameron (2013-16) for their guidance and advice. Thanks to Mike for inviting me to join the McDonald planet search group, giving me invaluable observational experience, and encouraging me to take on a couple of projects related to that work. Thanks to Rob for consulting on statistics, Chris on stellar spectroscopy, and Sally for helping me land on my feet as I was starting my research. Thanks to Andrew for hosting me in St. Andrews, and for suggesting that I undertake the project on WASP-33 that is described in Chapter 5.

Thanks also to my collaborators on various aspects of this project: Brett Addison, Daniel Bayliss, Kevin Gullikson, Chelsea Huang, Avi Shporer, Joshua Winn, and George Zhou. Special thanks to Simon Albrecht for invaluable advice and assistance as I was beginning this project. Thanks to Raphaëlle Haywood and Daniel Foreman-Mackey for productive discussions introducing me to Gaussian process regression, and the latter for technical suggestions regarding implementation in my

MCMC code. Finally, thanks to my collaborators on the various side-projects that I have undertaken unrelated to this dissertation, including: Juan Cabrera, Szilard Csizmadia, Hans Deeg, Malcolm Fridlund, Davide Gandolfi, Sascha Grziwa, Artie Hatzes, Adam Jensen, Greg Mace, Phillip MacQueen, Andrew Mann, Stefano Meschiari, Ivan Ramírez, Seth Redfield, and Paul Robertson.

Thanks to my friends and colleagues in the UT Astronomy Department, who have helped to make my five years in Austin an enjoyable and fulfilling time. In particular, Brian Mulligan and Kyle Kaplan for good times playing board games, Kyle for all of the hiking, Joel Green for the barbecues. Special shout-outs to those dedicated enough to play Ultimate Frisbee with me in 102°F heat, to the Ultra Deep Fielders, to happy hour at Crown.

Thanks to my parents, Donna and Paul, my brother Dustin, and my Aunt Marian for their encouragement and always being willing to listen. Thanks to you I had the best support network that I could have imagined (and occasionally chile when I couldn't get it in Austin).

Thanks to the resident astronomers and telescope operators at the Hobby-Eberly Telescope, who actually gathered most of the data used in this dissertation. Thanks also to Bill, Mike, and Caroline Caldwell, all of whom gathered the McDonald 2.7 m datasets that I used. Thanks to the staff at McDonald, in particular David Doss, for keeping things running smoothly during my many nights observing on the 2.7 m. And last but certainly not least, thanks to the Department staff who made sure that I got paid, was properly registered for classes, booked my official travel, and the thousand other things that needed to happen in the background; in particular, Rachel Walker, Terry Bruegging, Kelly Quinney, Susy Graves, and Lana Beranek.

I gratefully acknowledge funding from a NASA Earth and Space Science Fellow-

ship under Grant NNX12AL59H. I was also supported in part by the NASA K2 Guest Observer Program under grants NNX15AV58G (Cycle 1) and NNX16AE58G (Cycle 2) to the University of Texas at Austin. This work was also funded in part by NASA Origins of Solar Systems Program grant NNX11AC34G to William D. Cochran. This dissertation includes data taken at The McDonald Observatory of The University of Texas at Austin, and is based in part on observations obtained with the Hobby-Eberly Telescope, which is a joint project of the University of Texas at Austin, the Pennsylvania State University, Stanford University, Ludwig-Maximilians-Universität München, and Georg-August-Universität Göttingen. The HET is named in honor of its principal benefactors, William P. Hobby and Robert E. Eberly. This work makes use of observations from the LCOGT network.

Spin-Orbit Misalignments, Planet Candidate Validation, and Nodal Precession via Doppler Tomography

Marshall Caleb Johnson, Ph.D.
The University of Texas at Austin, 2016

Supervisor: William D. Cochran

Transiting planets around intermediate-mass stars ($1.5M_\odot < M_\star < 2.5M_\odot$, or 6500 K $< T_{\rm eff} <$ 10000 K on the main sequence) occupy a largely unexplored part of parameter space; these stars tend to rotate rapidly, and thus are unsuitable for the precise radial velocity observations that are typically used to follow up and confirm transiting planet candidates. In this dissertation I demonstrate the use of *Doppler tomography*, where I spectroscopically resolve the perturbation to the rotationally broadened stellar line profile during the transit due to the Rossiter-McLaughlin effect, to confirm transiting planet candidates around rapidly-rotating stars and to measure the (mis)alignment of the planetary orbit with respect to the stellar rotation. The demographics of planets around intermediate-mass stars are important for constraining models of planet formation as a function of stellar mass, while the distribution of spin-orbit misalignments of transiting planets is a powerful statistical tracer of planet migration processes.

Using Doppler tomography, I show that the hot Jupiter Kepler-13 Ab has a misaligned but prograde orbit; I improve upon the precision of the misalignment measurement for the hot Jupiter WASP-79 b, which has a nearly polar orbit; and I measure an aligned orbit for the warm Jupiter Kepler-448 b, and two degenerate solutions (both prograde) for the hot Jupiter HAT-P-41 b. I also analyze observations of several *Kepler* planet candidates–KOI-366.01, KOI-368.01, and KOI-972.01–in an attempt to validate them as *bona fide* planets. Unfortunately, due to small planetary radii and/or limited amounts of data, I am able to achieve only a $\sim 2\sigma$ detection of KOI-368.01, and am unable to detect KOI-366.01 or KOI-972.01.

I also analyze two epochs of Doppler tomographic observations of the highly inclined hot Jupiter WASP-33 b taken six years apart, and show that the path of the transit across the stellar disk has changed between the two epochs due to nodal precession of the planetary orbit. This allows me to measure the precession rate, and constrain the stellar gravitational quadrupole moment J_2.

Overall, I show that Doppler tomography is an effective tool for confirming and characterizing transiting planets around rapidly-rotating stars, where typical methods have difficulty.

Contents

List of Tables

List of Figures

Chapter One: Introduction

Attempts to discover planets orbiting other stars now have a more than half-century history, from the claim of van de Kamp (1963) to astrometrically detect planets around Barnard's Star (which was ultimately shown to be spurious; e.g., Gatewood & Eichhorn 1973), to the pioneering radial velocity survey of Walker et al. (1995), which began in 1980. It is only in the last two and a half decades, however, that the era of exoplanet astronomy has begun in earnest, with the discovery of the first exoplanets orbiting a pulsar (Wolszczan & Frail 1992) and subsequently the first orbiting a main sequence star (Mayor & Queloz 1995). Since the mid-1990s, the number of known exoplanets has grown drastically, in particular with over two thousand confirmed transiting planets discovered by the NASA *Kepler* mission (e.g., Rowe et al. 2014; Morton et al. 2016).

Most of the exoplanets discovered to date have been detected via two methods, the radial velocity method and the transit method. In the radial velocity method, precise radial velocity measurements (precision of a few to 10s of m s^{-1}) are used to detect the reflex motion of the host star due to the orbiting planet. Since the first detection of a hot Jupiter using this method by Mayor & Queloz (1995), continued technical, instrumental, and methodological improvements have steadily improved the achievable radial velocity precision (e.g., Fischer et al. 2016).

The transit method can only find planets that pass between their host star and the Earth each orbit, obscuring a small amount of starlight and causing a decrease in the flux from the star. Transit surveys obtain time series photometry of one or more stars, and monitor for the periodic decrements in flux due to the transiting planet.

Ground-based transit surveys have now discovered hundreds of planets, mostly hot Jupiters. The most successful surveys to date have been SuperWASP (Wide Angle Search for Planets; e.g., Pollacco et al. 2006; Collier Cameron et al. 2007) and HATNet (Hungarian Automated Telescope Network; e.g., Bakos et al. 2002, 2007), each of which has discovered dozens of planets. Other ground-based transit surveys include KELT (Kilodegree Extremely Little Telescope; e.g., Pepper et al. 2007; Beatty et al. 2012), the XO Project (e.g., McCullough et al. 2006), TrES (Trans-Atlantic Exoplanet Survey; e.g., Alonso et al. 2004), OGLE (Optical Gravitational Lensing Experiment; e.g., Konacki et al. 2003), MEarth (e.g., Charbonneau et al. 2009), and TRAPPIST (TRansiting Planets and PlanetIsimals Small Telescope; e.g., Gillon et al. 2016). WASP, HATNet, KELT, XO, and TrES all conduct or conducted wide-field surveys for transiting planets, attempting to maximize the yield of detected planets by observing as many stars as possible. OGLE is primarily a search for planetary microlensing events, but it has also produced several transiting planets as a by-product. MEarth and TRAPPIST target individual stars, nearby M and ultracool dwarfs, respectively.

Space-based transit surveys have yielded even more planets, due to the higher photometric stability and long uninterrupted viewing windows offered by the space environment; these allow the discovery of both smaller planets and longer-period planets than are possible from the ground. The first dedicated space-based transit mission was the CNES/ESA *CoRoT* mission (Convection Rotation et Transits planétaires; e.g., Barge et al. 2008), which to date has discovered several tens of transiting planets.

By far the most successful transit survey thus far, however, has been NASA's *Kepler* mission (Borucki et al. 2010). It monitored $\sim 150,000$ stars in the constellations Cygnus and Lyra for a little over four years, obtaining sufficiently high-quality photometry to detect the transits of Earth-sized planets around Sun-like stars. *Kepler* has produced more than 4,500 planet candidates (Coughlin et al. 2016), and more than 2,000 of these have now been confirmed or validated as *bona fide* planets (e.g., Rowe et al. 2014; Morton et al. 2016).

On 2013 May 11, however, just over four years into its prime mission, a second of four reaction wheels aboard the *Kepler* spacecraft failed. This rendered the spacecraft unable to keep pointing at its original field. Subsequently a new operating mode was developed, balancing solar radiation pressure across the spacecraft in concert with periodic thruster firings and the two remaining reaction wheels to enable pointing that, while not as precise as that during the *Kepler* prime mission, is more than sufficient for transit photometry. During this extended mission, dubbed K2, the *Kepler* spacecraft is pointing at a series of fields around the ecliptic for $\sim 75 - 80$ days at a time (Howell et al. 2014). It has already produced more than 200 planet candidates from its first year (four fields) of observations (Vanderburg et al. 2016), and more than 30 confirmed or validated planets (e.g., Johnson et al. 2016).

Transit survey photometry alone, however, is not sufficient to identify a secure sample of transiting planets. There are a host of instrumental and astrophysical false positive scenarios which can masquerade as a transiting planet. These include a background eclipsing binary blended with the light of a foreground star, diluting the eclipse depth to the point where they resemble transits (e.g., Colón & Ford 2011); an M dwarf or a brown dwarf (which have similar radii to giant planets) transiting the target star (e.g., Poleski et al. 2010); a main sequence star transiting a giant star which has been misclassified as a dwarf (e.g., Mann et al. 2012); or even internal reflections within the telescope, causing the light from a distant eclipsing binary to be added to a target star (e.g., Coughlin et al. 2014). Follow-up observations are therefore needed to exclude false positive scenarios and confirm that the transiting planet candidate is indeed a transiting planet.

Such follow-up observations generally begin with reconnaissance spectroscopy to determine approximate stellar parameters. Giant planet candidates, or short-period Neptunes and super-Earths, can then be detected with radial velocity observations, measuring their masses and confirming them as planets. Planet candidates that induce a stellar reflex motion too small to be detected can be validated by showing that they are unlikely to be a false positive. There are generally two flavors of validation: *validation by multiplicity*, which uses the fact that astrophysical false positives are highly unlikely to mimic systems with multiple transiting planets in order to validate multiplanet systems (e.g., Rowe et al. 2014); and *statistical validation*, which uses models of false positive scenarios to show that such scenarios are statistically unlikely (e.g., Morton et al. 2016).

Transiting planets are particularly scientifically important because they allow a host of follow-up observations to better characterize the planets. These range from simply measuring the planetary density (the transit data provide the planetary radius and radial velocity observations allow the measurement of the mass) to detailed studies of planetary atmospheric composition and structure (e.g., Redfield et al. 2008; Sing et al. 2016). In this dissertation I will discuss one type of follow-up observation: measuring the angle between the stellar spin and planetary orbital angular momentum vectors.

In our own solar system, these vectors are well aligned; for instance, the Sun's rotation axis is oriented at an angle of $\sim 7^\circ$ from the normal to the orbital plane of the Earth (e.g., Beck & Giles 2005). As I will describe in the next sections, however, this is not always the case for extrasolar planetary systems–and this fact can tell us a great deal about the formation and past evolution of these systems.

1.1 Doppler Tomography, the Rossiter-McLaughlin Effect, and Spin-Orbit Misalignments

All stars rotate, at least to some degree. The stellar absorption line profiles that we observe are the integral of the line profiles from each individual surface element over the stellar disk. Since rotation causes different surface elements to be differently Doppler shifted, rotation results in rotational broadening of the spectral line. The width of a star's spectral lines thus allows us to measure its rotation rate, once other forms of line broadening (thermal, microturbulent, macroturbulent, etc.) are accounted for. What is actually measured is $v \sin i_{\star}$, the stellar equatorial rotational velocity projected onto the plane of the sky, since the inclination of the stellar rotation axis with respect to the line of sight ($i_{\star}$) is generally unknown. Note that this is typically denoted $v \sin i$ in the literature, but I use $i_{\star}$ to avoid confusion with the inclination of the planetary orbital plane i_P, which is *also* typically denoted i in the literature.

What if a planet transits the star? The opaque planetary disk will obscure some stellar surface elements, which do not contribute to the formation of the rotationally broadened stellar line profile, resulting in a shallower line profile at the corresponding velocities. Equivalently, the obscuring planetary disk causes a decrease in the continuum flux at all wavelengths, as well as lessened absorption over a small range of velocities, again resulting in a shallower portion of the line profile. As the planetary disk moves during the transit, sequentially obscuring different stellar surface elements, the line profile perturbation moves in a corresponding manner.

This line profile perturbation is typically not observed directly, but rather as an anomalous radial velocity shift; the line profile perturbation changes the line centroid, which can be interpreted as a change in the stellar radial velocity. This is known as the Rossiter-McLaughlin effect after Rossiter (1924) and McLaughlin (1924), who produced the first well-sampled in-eclipse radial velocity curves for the eclipsing binaries β Lyr and β Per (Algol), respectively, although this effect had originally been predicted by Holt (1893).

In some cases, however, the stellar line profile and the line profile perturbation *can* be spectroscopically resolved (Fig. 1.1). This typically requires moderately rapid stellar rotation ($v \sin i_\star > 15-20$ km s^{-1}) and high spectral resolution (resolving power $R > 30,000$). Even more slowly rotating stars ($v \sin i_\star \sim 3-10$ km s^{-1}) may be observed if the spectral resolution is sufficient to resolve the line profile (e.g., Collier Cameron et al. 2010a). This technique, where the line profile is spectroscopically resolved, is known as Doppler tomography, but is sometimes also known as line-profile tomography or Doppler imaging. This technique is the focus of this dissertation.

The path of the planet across the stellar disk (relative to the stellar rotation axis) during the transit maps directly to the path of the line profile perturbation across the stellar line profile. The path of the transit, or transit chord, is governed by two parameters: the impact parameter b and the sky-projected spin-orbit misalignment λ. I show the definitions of these and other relevant parameters graphically in Fig. 1.2, and the effects of the transit geometry in b and λ upon the motion of the transit signature across the line profile in Figs. 1.3, 1.4, 1.5, and 1.6. The detection of the Doppler tomographic transit signature thus allows the measurement of b and λ. The impact parameter can also be measured using the transit lightcurve, but, except in

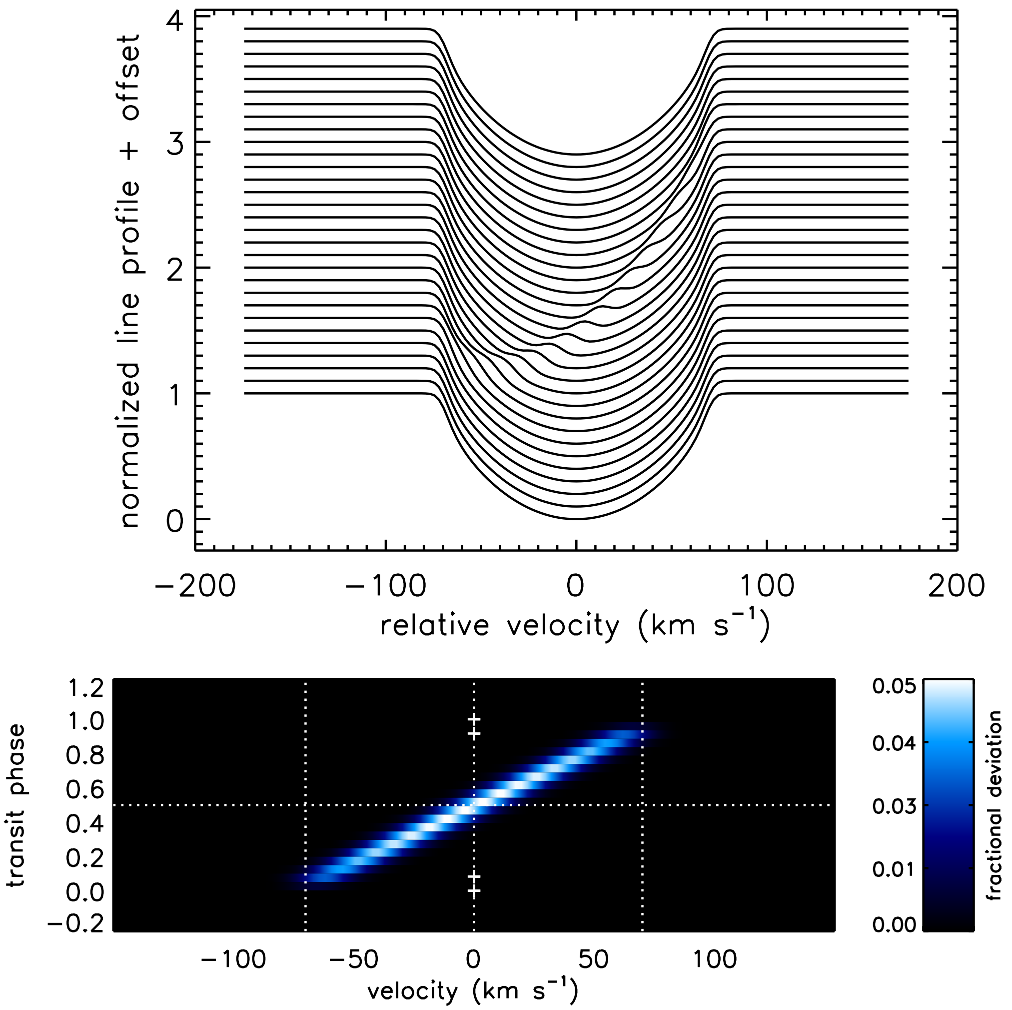

Figure 1.1 Top: model time series line profiles during a transit, showing the distortion due to the planetary shadow moving across the absorption line. Time increases from bottom to top, and each consecutive line profile is displaced upwards by an arbitrary amount for clarity. I produced the model using the methodology described in §2.3, for a planet with $R_P/R_\star = 0.09$ orbiting a star with $v \sin i = 70$ km s^{-1} with spin-orbit misalignment $\lambda = 0^\circ$ and impact parameter $b = 0$. Bottom: these same data once the out-of-transit line profile has been subtracted off, i.e., the time series line profile residuals. This is the format in which I will display Doppler tomographic data throughout this dissertation. The transit signature is the bright streak moving from lower left to upper right. Time increases from bottom to top. I define the "transit phase" such that it equals 0 at ingress and 1 at egress. Vertical dotted lines mark $v = 0, \pm v \sin i$, and a horizontal dotted line marks the time of mid-transit. Small crosses mark the times of first, second, third and fourth contacts. The units of the color scale are fractional deviation from the average out-of-transit line profile.

special circumstances (see §1.1.1), λ cannot be measured using the lightcurve.

It is important to note that the quantity λ is the *sky-projected* spin-orbit misalignment. The angle between the stellar spin and planetary orbital angular momentum vectors (or, equivalently, between the stellar spin axis and the normal to the planetary orbital plane) is typically denoted ψ. λ is ψ projected onto the plane of the sky. λ is relatively easy to measure using the Rossiter-McLaughlin effect or other methods, but ψ is not. ψ is not typically directly measurable, and, once λ is known, knowledge of i_P and $i_\star$, the inclination of the planetary orbital plane and the stellar rotation axis, respectively, with respect to the line of sight, is required to calculate ψ from λ. i_P can be measured directly from the transit lightcurve. $i_\star$, however, is typically very difficult to measure precisely. Thus, in most cases we are limited to analyzing the distribution of λ, rather than the more physically meaningful ψ. This is not a large impediment, however; Fabrycky & Winn (2009) showed how to convert distributions of λ into ψ for comparison to models, requiring the assumption that stellar spin axes are distributed randomly.

The amplitude of the Rossiter-McLaughlin radial velocity anomaly during a transit or eclipse is approximately,

$$dv \sim 52.8\,\mathrm{m\,s^{-1}}\left(\frac{v\sin i_\star}{5\,\mathrm{km\,s^{-1}}}\right)\left(\frac{R_P}{R_J}\right)^2\left(\frac{R_\star}{R_\odot}\right)^{-2} \tag{1.1}$$

adapting Eqn. 6 of Gaudi & Winn (2007) to the terminology used in this dissertation. The Rossiter-McLaughlin amplitude due to an eclipse of a rapidly-rotating star can be tens of km s^{-1}, easily detectable even a century ago (Rossiter 1924; McLaughlin 1924). As is apparent from Eqn. 1.1, however, the Rossiter-McLaughlin amplitudes of transiting hot Jupiters are typically a few tens of m s^{-1}–but, by the time that technology had advanced to the point that the detection of transiting exoplanets was possible, radial velocity methods were also good enough to detect the Rossiter-

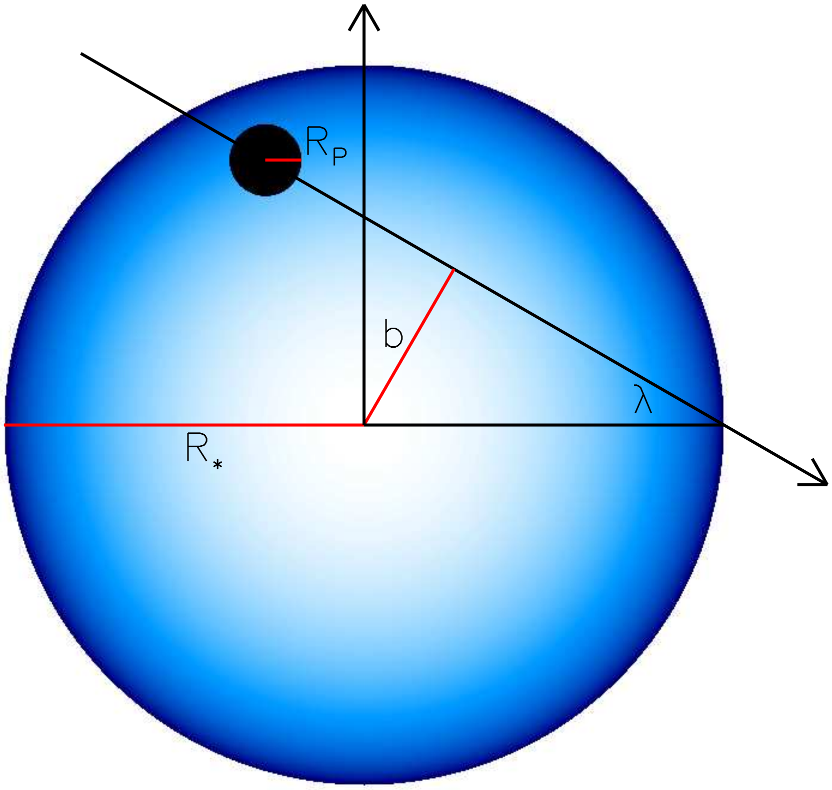

Figure 1.2 Illustration of the geometry of an exoplanetary transit and definition of terms used in this work. The stellar rotation axis is marked by the vertical black arrow, and the star rotates from left to right (i.e., the arrow can also be considered to be the projection of the stellar rotational angular momentum vector onto the plane of the sky). The planet (small black disk) moves along the long black arrow (which I will refer to as the "transit chord"). The red lines show the impact parameter b (the minimum distance between the transit chord and the center of the stellar disk), and the stellar and planetary radii $R_\star$ and R_P, respectively, as marked. The (sky-projected) spin-orbit misalignment λ is the angle between the transit chord and a line perpendicular to the projected stellar rotation axis. This figure depicts the transit of a planet with $R_P/R_\star = 0.1$, $b = 0.5$, $\lambda = 30°$. The limb darkening depicted on the stellar disk is typical for a mid-A main sequence star.

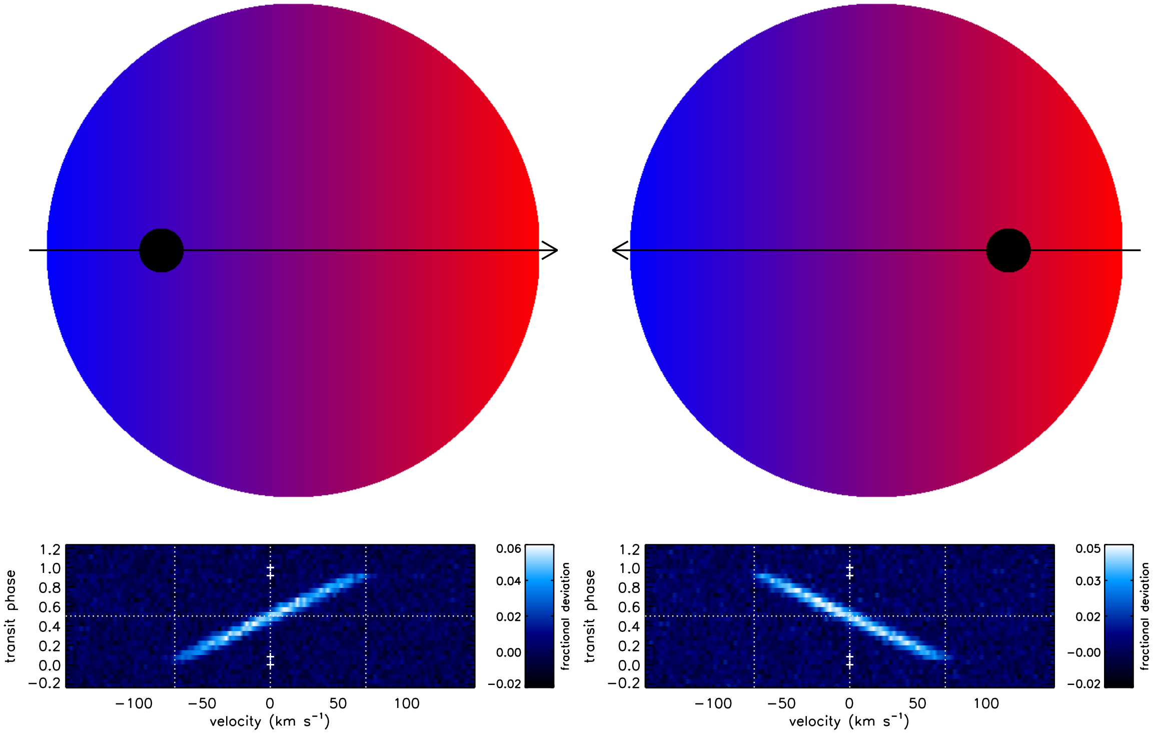

Figure 1.3 Top row: transit geometry, and bottom row: the corresponding time series line profile residuals for, left column: an aligned orbit ($\lambda = 0°$) and right column: an anti-aligned orbit ($\lambda = 180°$). The color scale on the stellar disk depicts the rotational Doppler shift across the stellar surface, assuming solid body rotation (in which case the isovelocity contours are straight and parallel to the projected rotation axis); blue and red correspond to blue and red shift, respectively. The stellar rotation axis is vertical, and the visible stellar surface rotates from left to right. The planet moves along the black line, in the direction indicated by the arrow. I have added a small amount of noise to the time series line profile residuals to better approximate actual observations. Both geometries have a central transit ($b = 0$) and $v \sin i_\star = 70$ km s^{-1}. Note the qualitatively different motion of the transit signature for the two cases.

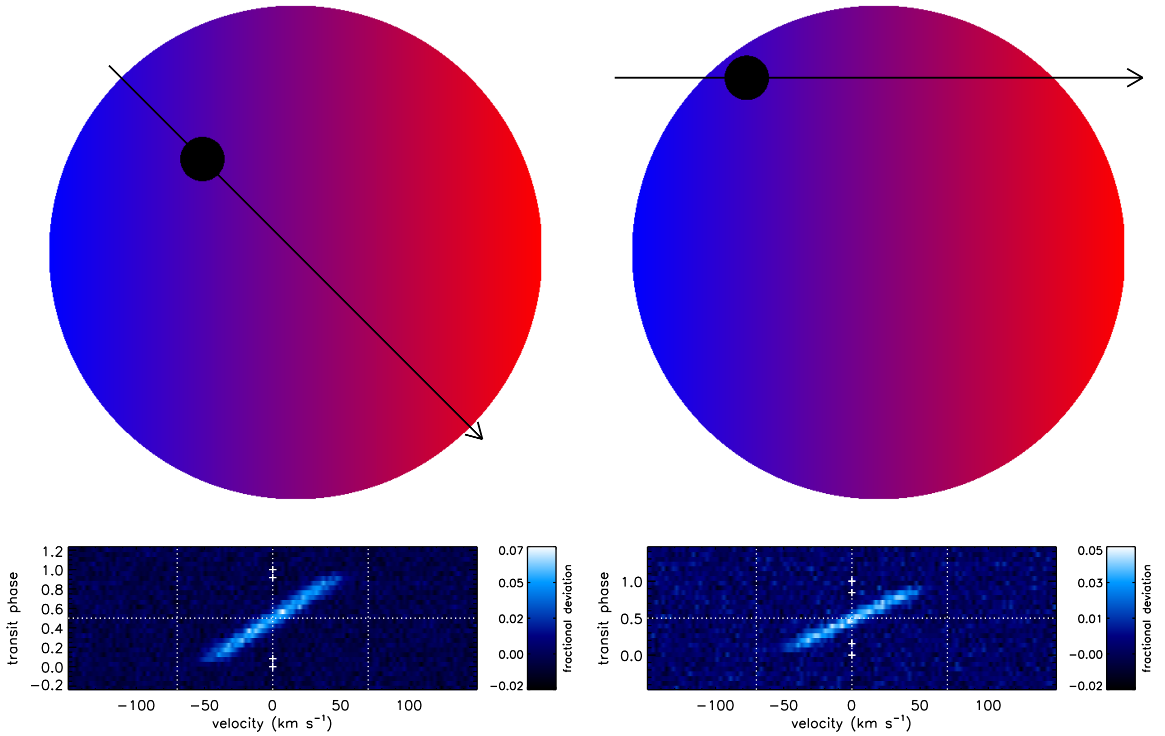

Figure 1.4 Same as Fig. 1.3, but with left column: a central transit ($b = 0$) with a misaligned orbit ($\lambda = 45°$), and right column: a non-central transit ($b = 0.71$) with an aligned orbit ($\lambda = 0°$). The velocity at which the transit signature appears at ingress, and at which it disappears at ingress, are identical for the two cases, and so there is a degeneracy between these two geometries; however, these two geometries have different transit durations–the large b case will have a shorter transit–and so knowledge of the transit duration, either directly from the Doppler tomographic data or from prior knowledge of the photometric transit lightcurve, can disambiguate these cases.

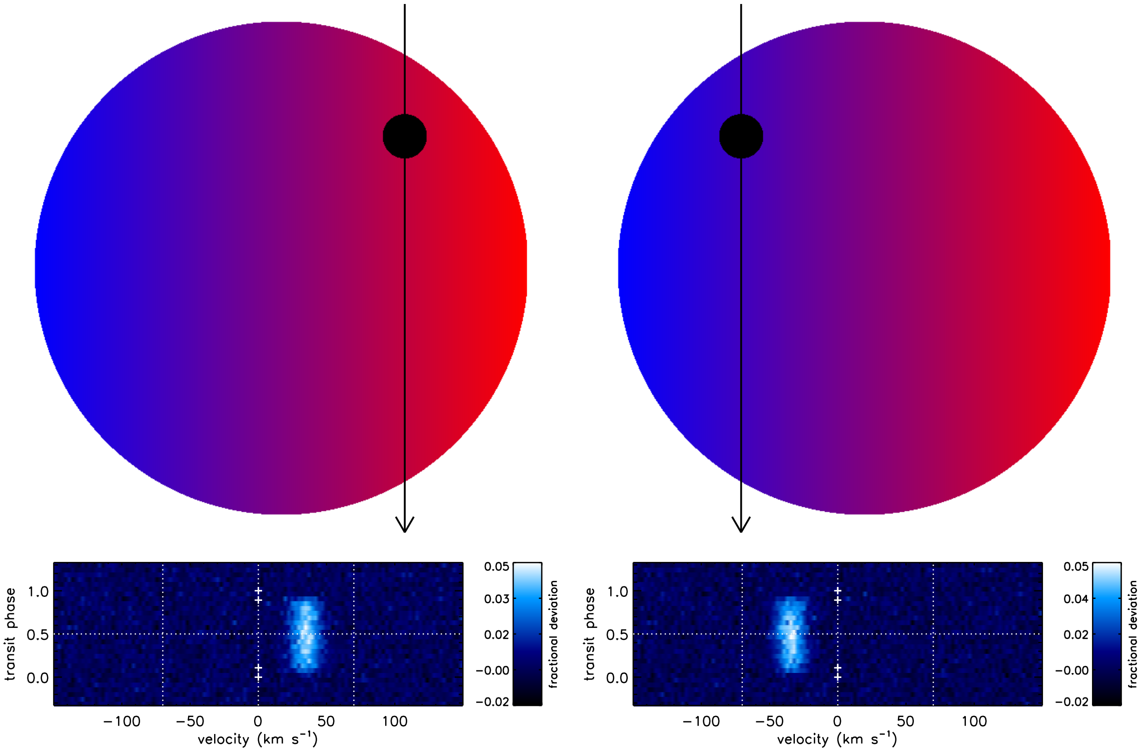

Figure 1.5 Same as Figs. 1.3 and 1.4, but with polar orbits. The left column shows a case with $\lambda = 90°$, $b = 0.5$, and the right column with $\lambda = 90°$, $b = -0.5$. In this case it is straightforward to discern the direct mapping between the path of the transit chord and the path of the transit signature; with $b = \pm 0.5$, the transit chord passes halfway between the center of the stellar disk and the limb, and consequently, for a polar orbit, the transit signature occurs at halfway between $v = 0$ and $v = \pm v \sin i_\star$.

McLaughlin effect for planets.

The first Rossiter-McLaughlin observations of a transiting exoplanet were carried out by Queloz et al. (2000), who observed HD 209458 b (the first known transiting exoplanet) only a few months after the discovery of the transits (Charbonneau et al. 2000; Henry et al. 2000). Queloz et al. (2000) were able to show that the planetary orbit is prograde and consistent with aligned. A precise determination of λ for an exoplanetary system had to wait another five years, for the work of Winn et al. (2005), who also observed HD 209458 b and obtained $\lambda = -4.4 \pm 1.4°$. Over the next few

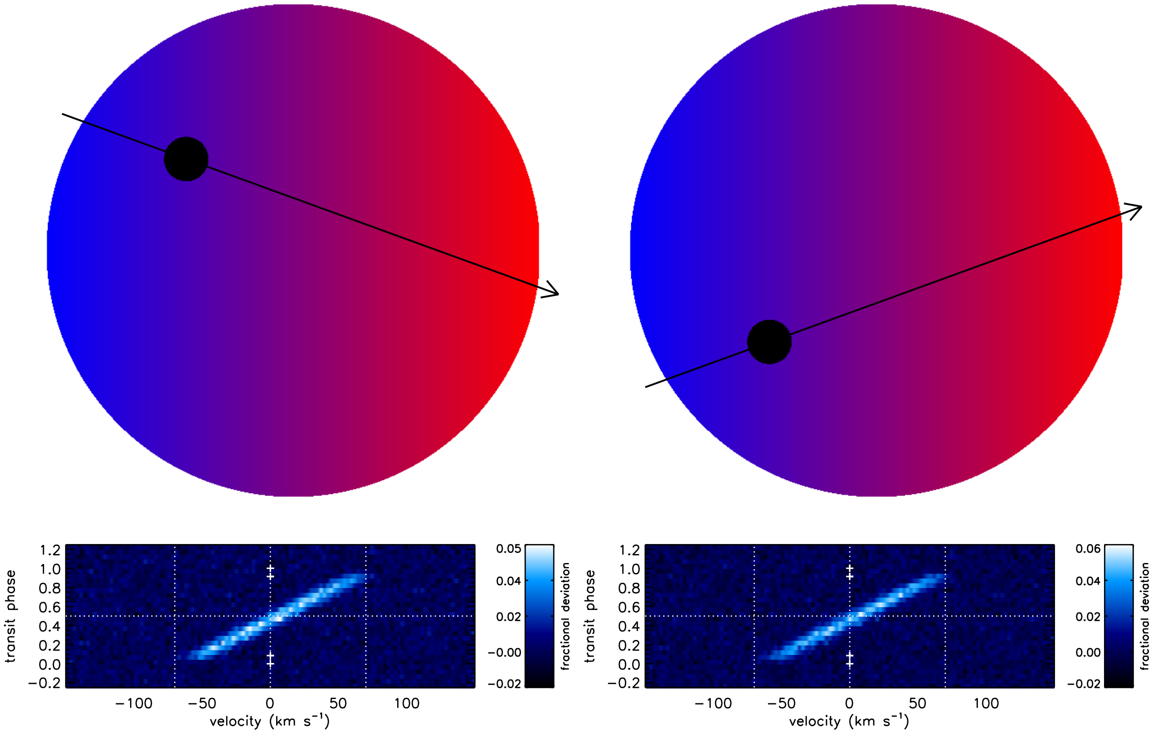

Figure 1.6 Same as Figs. 1.3, 1.4, and 1.5, but illustrating a degeneracy inherent to Doppler tomographic analysis. The left column shows a case with $\lambda = 20^\circ$, $b = 0.2$, and the right column with $\lambda = -20^\circ$, $b = -0.2$. In both geometries the transit signature will appear at ingress at the same velocity and disappear at egress at the same velocity, and the transit duration will be the same for both geometries, and so both will produce identical time series line profile residuals. It is therefore impossible to distinguish a geometry with $+\lambda$, $+b$ from one with $-\lambda$, $-b$ with Doppler tomography, at least in the limit of solid body stellar rotation depicted here.

years, the spin-orbit angles of several more hot Jupiters were measured, all of which were prograde and well-aligned with the stellar spin (Winn et al. 2006, 2007b, 2008b; Narita et al. 2007; Wolf et al. 2007; Bouchy et al. 2008). It appeared that, like our own solar system, exoplanetary systems orbited on orderly planes well-aligned with the spin axes of their host stars.

The first exoplanet unambiguously shown to have a highly misaligned orbit was HAT-P-7 b, which was shown to have a nearly retrograde orbit by Winn et al. (2009c) and Narita et al. (2009b). With the increasing pace of discovery of transiting exoplanets and Rossiter-McLaughlin follow-up, a class of misaligned planets ($|\lambda| > 30^\circ$ to good confidence) quickly emerged (Johnson et al. 2009; Anderson et al. 2010; Triaud et al. 2010; Queloz et al. 2010; Collier Cameron et al. 2010b). All of these were hot Jupiters except for HD 80606 b (Moutou et al. 2009; Winn et al. 2009b; Hébrard et al. 2010), which has an orbital period of 111 days and a highly eccentric orbit. These constituted a sufficiently large sample that Winn et al. (2010a) were able to identify a pattern: the misaligned planets orbited hot stars ($T_{\text{eff}} > 6250$ K), the only exceptions being the somewhat longer-period WASP-8 b and HD 80606 b; the remainder of planets around cooler stars were well-aligned. This pattern has only been strengthened by more recent observations (see e.g. the review of Winn & Fabrycky 2015); I discuss the current state of this work, and the implications thereof, in §1.1.2.

Almost all of the planets observed with the Rossiter-McLaughlin effect to date have been hot Jupiters; the amplitude of the effect scales as $\propto (R_P/R_\star)^2$ (Eqn. 1.1), hampering efforts to observe small planets. Furthermore, the vast majority of small transiting planets were discovered by *Kepler*, and so orbit faint stars for which it is not feasible to obtain sufficiently precise, sufficiently high time resolution RV observations with current facilities. Observations of longer-period planets are challenging due to their long transit durations. In order to accurately measure the spin-orbit misalignment from the radial velocity Rossiter-McLaughlin effect, it is necessary to observe through the entirety of a transit, which, for transits lasting more than a few hours, is challenging.

Nonetheless, Rossiter-McLaughlin observations of a few planets in each of these classes have been accomplished. Bourrier & Hébrard (2014) measured the spin-orbit misalignment of the super-Earth 55 Cnc e, finding a highly inclined orbit (which had been predicted by Kaib et al. 2011); however, López-Morales et al. (2014), using data from the same instrument, were unable to detect the radial velocity anomaly during the transit. To date only three other planets with $M_P < 0.3 M_J$ have had their spin-orbit misalignments measured with the Rossiter-McLaughlin effect (Winn et al. 2010c; Hirano et al. 2011b; Sanchis-Ojeda et al. 2013; Esposito et al. 2014); all of these are misaligned. Only three warm Jupiters ($P > 10$ days) have Rossiter-McLaughlin spin-orbit misalignment measurements, but two of these have highly eccentric orbits (e.g., Narita et al. 2009a; Hébrard et al. 2010), and the third was only a $\sim 2\sigma$ detection of the Rossiter-McLaughlin effect (Santerne et al. 2014).

Doppler tomography has to date enjoyed only much smaller applicability than radial velocity Rossiter-McLaughlin observations, due largely to the slow rotation of the FGK stars that host most known transiting hot Jupiters. Collier Cameron et al. (2010a) were the first to observe an exoplanetary transit using Doppler tomography, measuring the spin-orbit alignment of HD 189733 b, and subsequently Collier Cameron et al. (2010b) published observations of WASP-33 b, which was also the first planet to be confirmed using Doppler tomography. Since that time, only a handful of Doppler tomographic observations have been published: for WASP-3 b (Miller et al. 2010), WASP-32 b and WASP-38 b (Brown et al. 2012b), and HAT-P-2 b and Kepler-25 c (Albrecht et al. 2013), all of which orbit moderately rapidly rotating stars ($v \sin i_\star < 25$ km s^{-1}), and CoRoT-11 b (Gandolfi et al. 2012), KELT-7 b (Bieryla et al. 2015; Zhou et al. 2016a), Kepler-448 b (Bourrier et al. 2015), HAT-P-57 b (Hartman et al. 2015), HAT-P-56 b (Zhou et al. 2016a), and KELT-17 b (Zhou et al. 2016b), all of which orbit more rapidly rotating stars. Doppler tomographic analyses have also been published for HAT-P-27 b/WASP-40 b (Brown et al. 2012b), WASP-93 b, and WASP-118 b (Hay et al. 2016), but in all of these cases insufficient signal-to-noise prevented a robust detection of the transit signature and measurement of the spin-orbit misalignment. The only planets confirmed so far with Doppler tomographic observations are WASP-33 b, Kepler-448 b, and HAT-P-57 b.

1.1.1 Other Techniques for Measuring Spin-Orbit Misalignments

While most of the spin-orbit misalignment measurements to date have come via the Rossiter-McLaughlin effect, it and Doppler tomography are not the only techniques that can be used to measure the spin-orbit misalignments of transiting planets. One alternative is the gravity-darkening method. Rapidly rotating stars are dynamically oblate, and this can result in *gravity darkening*, where the poles of the star are closer to the stellar center, and thus hotter and brighter, than the equator. This breaks the rotational symmetry of the visible stellar disk, and a planet transiting across such a star will display an asymmetric transit shape, the details of which depend upon the spin-orbit misalignment (Barnes 2009). The deviations in transit shape are small and so typically require space-based data to detect, but this method has been used to measure spin-orbit misalignments for several transiting planets, mostly *Kepler* discoveries (Barnes et al. 2011, 2013, 2015a; Zhou & Huang 2013; Ahlers et al. 2014, 2015; Masuda 2015). Unlike Doppler tomography, the gravity darkening method is sensitive to both the sky-projected spin-orbit misalignment λ and the full three-dimensional misalignment ψ. Since this method also relies on rapid rotation, it is applicable over a similar stellar parameter space to Doppler tomography. Detection of an asymmetric transit shape shows that the transiting object must be orbiting the target rapidly-rotating star, and thus may also be used to validate planet candidates.

Starspots also change the intensity profile of the visible stellar disk. When a transiting planet crosses a starspot, it subtracts a smaller amount of flux, resulting in a "bump" in the light curve. If the star has a long-lived complex of spots, it may be occulted by the planet on successive transits; as the motion of the spots across the stellar disk is governed by the stellar rotation, this may be used to infer the spin-orbit misalignment. Like gravity darkening, this method also relies upon precise space-based light curves, and, in some cases, can be used to measure the full three-dimensional spin-orbit misalignment ψ (e.g., Sanchis-Ojeda & Winn 2011). First used observationally by Sanchis-Ojeda et al. (2011), this method was also the first to provide spin-orbit alignment measurements for a multiplanet system (Kepler-30; Sanchis-Ojeda et al. 2012).

Another method that has been used to measure the spin-orbit misalignments of transiting planets is asteroseismology, the study of the pulsation frequencies of stars. One observable from this is the inclination of the stellar rotation axis with respect to the line of sight, $i_\star$. Thus asteroseismology gives the opposite component of the spin-orbit misalignment from Doppler tomography–if a star has $i_\star$ much smaller than 90° and a transiting planet, then the planet's orbit must be misaligned. Most of the planet host stars observed so far with asteroseismology have $i_\star \sim 90^\circ$, and thus are likely aligned (e.g., Chaplin et al. 2013; Campante et al. 2016), but Huber et al. (2013) found that the two transiting planets around the red giant Kepler-56 must be substantially misaligned. Asteroseismology has the advantage that its feasibility does not depend upon the properties of the planets, and so it is applicable for arbitrarily small or long-period transiting planets; however, the types of pulsations necessary to measure $i_\star$ are only present in red giant and approximately solar-type stars.

Finally, $i_\star$ may also be measured or estimated if $v \sin i_\star$, the stellar radius, and the rotation period of the star are known; $i_\star$ can be calculated from these parameters in a straightforward manner. The rotation period may either be measured through periodic photometric variability due to starspots (e.g., Winn et al. 2007a), or estimated statistically using a prior distribution of rotation periods derived from the stellar parameters and literature knowledge of the dependence of stellar rotation on these properties (e.g., Schlaufman 2010, who used this method to identify a population of likely misaligned hot Jupiters, all around hotter, more massive stars).

1.1.2 Trends and Interpretations of Spin-Orbit Misalignments

As noted above, Winn et al. (2010a) first recognized the pattern that hot Jupiters with misaligned orbits preferentially orbit stars with $T_{\text{eff}} > 6250$ K, and that such planets around cooler stars are preferentially aligned. They hypothesized that this pattern could be explained if hot Jupiters are emplaced onto highly misaligned orbits by whatever process brings them close to their host stars, and then tides are subsequently able to realign those around cool stars, but not hot stars. Stars cooler than $T_{\text{eff}} \sim 6250$ K have deep, massive outer convective envelopes, which Winn et al. (2010a) suggested could efficiently tidally couple to the planet, quickly re-aligning its orbit.

Albrecht et al. (2012b) expanded the sample of planets with measured spin-orbit misalignments, and continued investigation of these trends. They further solidified the trend seen by Winn et al. (2010a), showing that the only severely misaligned planets around cool stars were those with either low masses or long orbital periods–i.e., the very planets that would be expected to have long tidal damping time scales. Albrecht et al. (2012b) then constructed a relative tidal damping timescale–the *absolute* time scales for tidal damping are very uncertain due to large uncertainties in the tidal quality factors of planets and stars and incomplete understanding of tidal theory, but the *relative* factors influencing the time scales are better understood. This allowed Albrecht et al. (2012b) to show that planets with short tidal dissipation time scales tend to be well-aligned, while those with longer time scales show a wide range of (mis)alignments. While tides are generally thought to be at least partially responsible for the spin-orbit misalignment distribution of hot Jupiters, there are still many uncertainties regarding this mechanism; I will describe these in more detail in §1.2.3.

In Fig. 1.7 I show the current sample of hot Jupiter spin-orbit misalignments as a function of stellar effective temperature, and in Fig. 1.8 I show the cumulative distribution of spin-orbit misalignments for hot Jupiters around hot and cool stars, as compiled from the literature data listed in Table A.1.

Another pattern was found by Hébrard et al. (2011a), who noted that there were no known planets with masses greater than 3 M_J on retrograde orbits ($|\lambda| > 90°$). This remains the case with the larger sample of spin-orbit misalignment measurements now available (Fig. 1.9). The statistical significance of this finding is strengthened by the fact that 7 of the 11 planets with $M > 3M_J$ and measured spin-orbit misalignments are around hot stars, and would be expected to have a wide range of measured obliquities. The tidal realignment timescale is inversely proportional to the planetary mass (Albrecht et al. 2012b), and so more massive planets are expected to realign more quickly and are less likely to remain in a retrograde configuration than less massive planets.

The picture is less clear for warm Jupiters, small planets, and multiplanet systems, due to the small number of measurements compiled to date. Albrecht et al. (2013) were the first to consider the statistical properties of the misalignments of multiplanet systems. At the time only five such measurements existed in the literature, all of which were compact multiplanet systems (i.e., with multiple closely-spaced

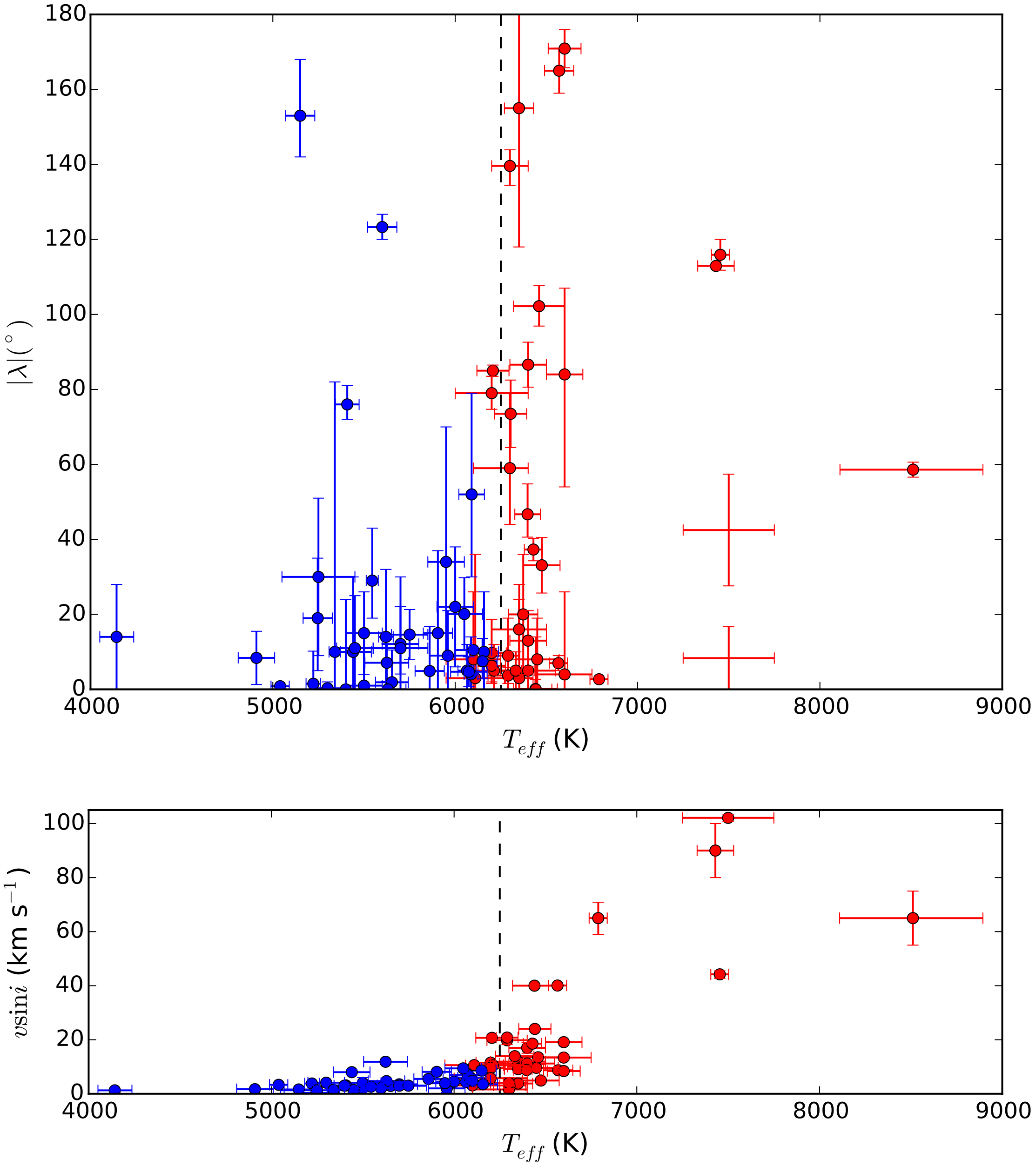

Figure 1.7 A current version of the key figure from Winn et al. (2010a)–Fig. 2 of that work–showing (top) measured spin-orbit misalignments from the literature as a function of stellar $T_{\rm eff}$, and (bottom) the $v \sin i_\star$ values for these stars. Only hot Jupiters (planets with $0.5\,M_J < M < 13\,M_J$, $P < 10$ days) are shown in this plot. Planets orbiting stars with $T_{\rm eff} < 6250$ K are shown in blue, those with $T_{\rm eff} \geq 6250$ K (to within 1σ) are shown in red, and a vertical dashed line denotes the 6250 K dividing line between the two regimes. Note the increase in $v \sin i_\star$ at $T_{\rm eff} \sim 6250$ K. The pair of red error bars without accompanying data points in the top panel denote HAT-P-57 b, for which Hartman et al. (2015) were only able to measure a 2σ range of $-16.7^\circ < \lambda < 3.3^\circ$ or $27.6^\circ < \lambda < 57.4^\circ$. The compilation of literature data used to produce this figure is listed in Table A.1.

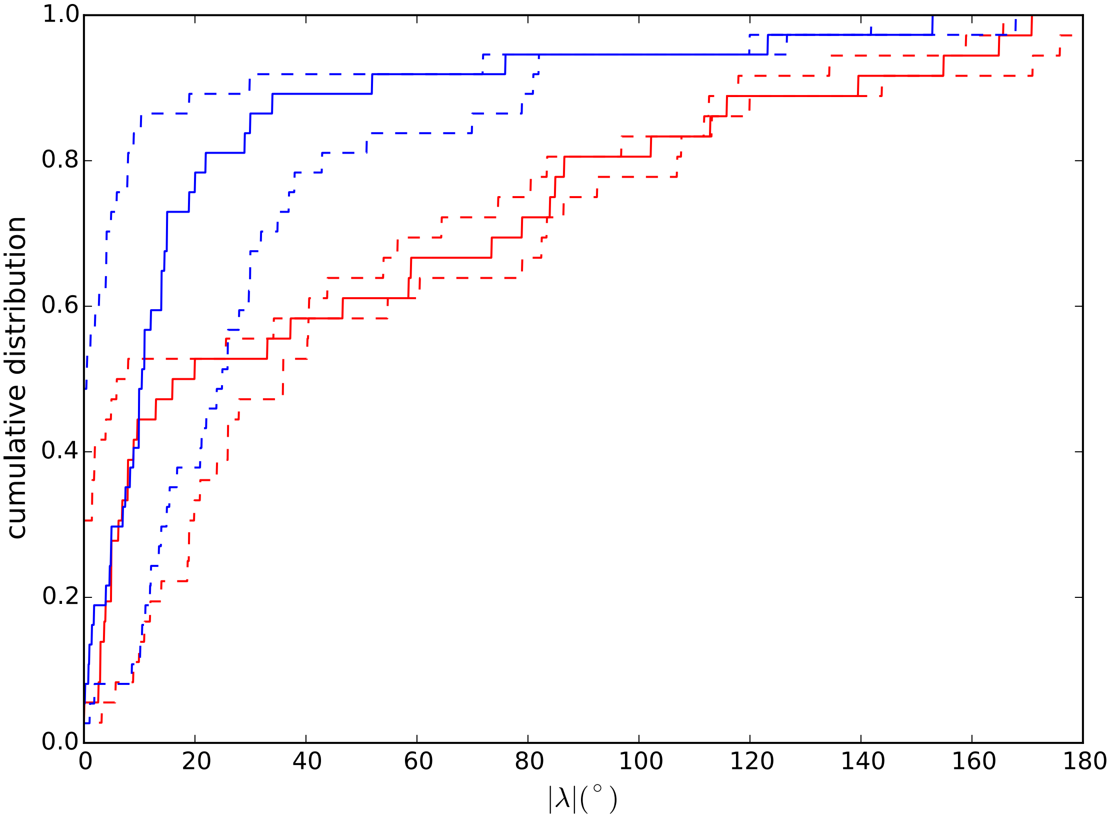

Figure 1.8 The cumulative distribution of spin-orbit misalignments for the data shown in Fig. 1.7. The blue line shows the cumulative distribution for hot Jupiters around cool stars ($T_{\rm eff} < 6250$) and the red line those around hot stars. The 1σ limits on each value of $|\lambda|$ are shown as the dotted lines, i.e., the dotted lines show the 1σ confidence interval of each distribution. The compilation of literature data used to produce this figure is listed in Table A.1; HAT-P-57 b is not included in this figure due to the two degenerate solutions for λ found by Hartman et al. (2015).

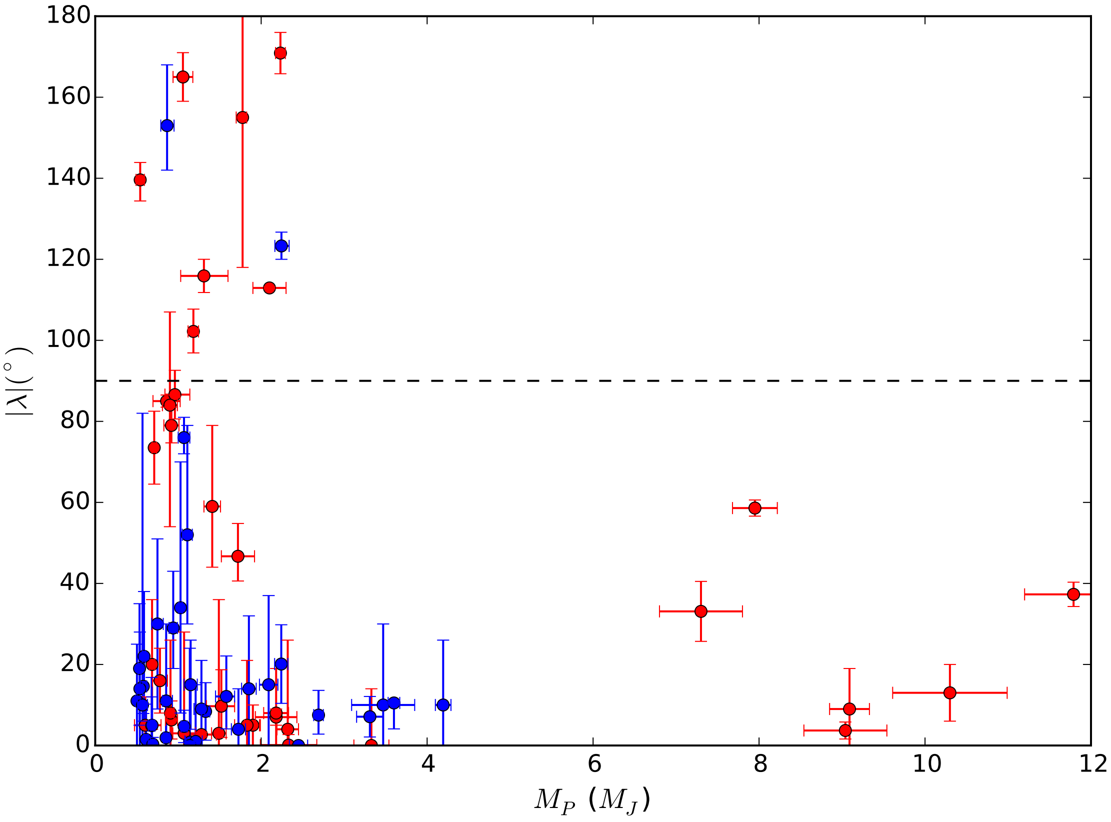

Figure 1.9 A current version of a key figure from Hébrard et al. (2011a)–Fig. 4 of that work–showing measured spin-orbit misalignments from the literature as a function of planetary mass. There are no known planets with retrograde orbits and $M > 3M_J$. Only hot Jupiters (planets with $0.5\,M_J < M < 13\,M_J$, $P < 10$ days) are shown in this plot. As in Fig. 1.7, planets orbiting stars with $T_{\rm eff} < 6250$ K are shown in blue, and those with $T_{\rm eff} \geq 6250$ K are shown in red. A horizontal dashed line marks the boundary between retrograde ($|\lambda| > 90^\circ$, top) and prograde ($|\lambda| < 90^\circ$, bottom) orbits. The compilation of literature data used to produce this figure is listed in Table A.1; again, HAT-P-57 b (Hartman et al. 2015) is not included in this figure, as there is only an upper limit available for its mass.

planets) and all of which were well-aligned with the stellar rotation. Since then, three multiplanet systems have been shown or have been claimed to be misaligned: Kepler-56 (Huber et al. 2013), via asteroseismology; 55 Cnc e (Bourrier & Hébrard 2014), using the Rossiter-McLaughlin effect; and KOI-89 (Ahlers et al. 2015), via gravity darkening. While the number of multiplanet systems with measurements of λ is small, there is a larger sample with measurements of $i_\star$; Campante et al. (2016) presented asteroseismic measurements of $i_\star$ for 15 *Kepler* multiplanet systems, all of which have $i_\star = 90^\circ$ to within 2σ confidence, suggesting that all of these systems are likely aligned. Only two of these, however, orbit stars with $T_{\rm eff} > 6250$ K.

Likewise, only a few spin-orbit misalignment measurements for warm Jupiters exist: HD 17156 b (Narita et al. 2009a), HD 80606 b (Hébrard et al. 2010), Kepler-420 b (Santerne et al. 2014), and Kepler-448 b (Bourrier et al. 2015). As noted earlier, the first two of these have highly eccentric orbits, approaching their stars to distances more typical of hot Jupiters (and thus may or may not be considered to be warm Jupiters, depending upon definition), and the third is only a $\sim 2\sigma$ detection of the Rossiter-McLaughlin effect, resulting in a highly uncertain spin-orbit misalignment. Nonetheless, in Fig. 1.10 I show the spin-orbit misalignments of the four warm Jupiters measured to date. Due to the small number of planets and problems with some measurements, the sample is again insufficient to discern any pattern with statistical significance.

Finally, there are only a handful of spin-orbit misalignment measurements for small planets with no other known planetary companions in that system. Gravity darkening appears to show that the super Earth candidate KOI-2138.01 is aligned (Barnes et al. 2015a), while eight single-transiting *Kepler* systems with small planets and asteroseismic stellar inclinations from Campante et al. (2016) all appear to be

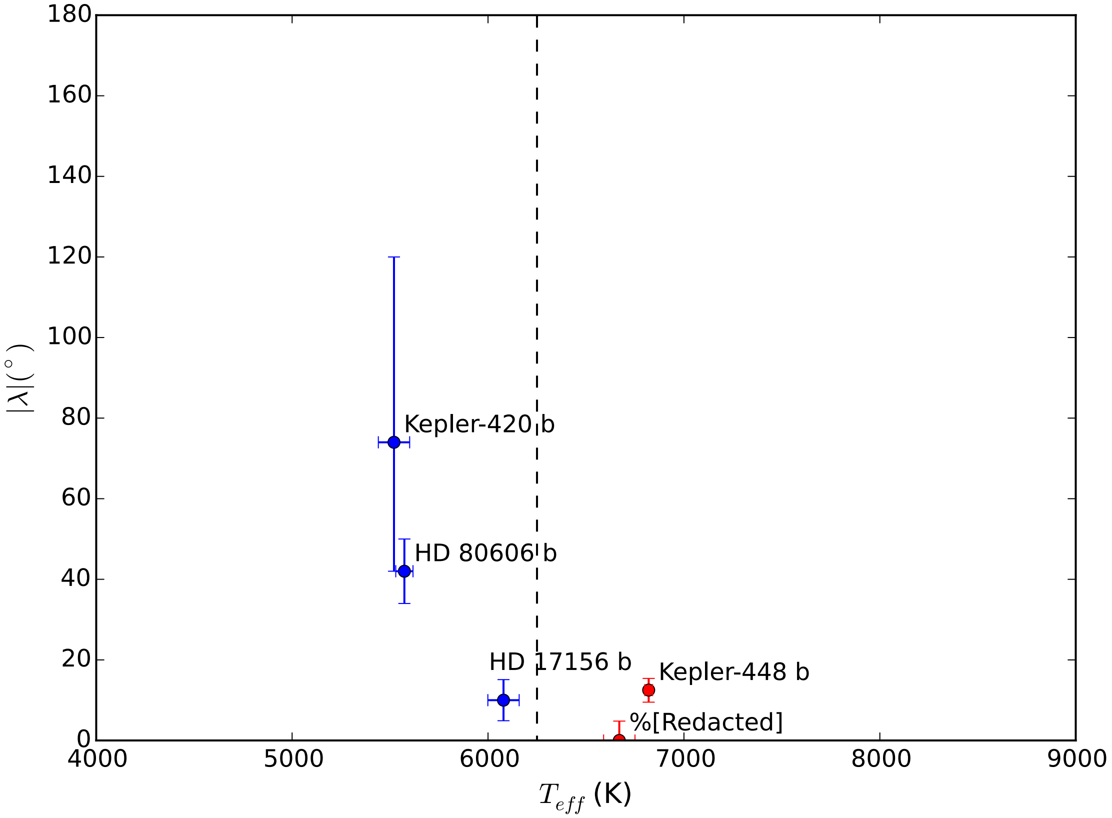

Figure 1.10 Same as Fig. 1.7, but for warm Jupiters (i.e., planets with $0.5\,M_J < M_P < 13\,M_J$ and $P > 10$ days). Only a handful of warm Jupiters have published spin-orbit misalignment measurements, and so it is difficult to discern any pattern. Contrary to hot Jupiters the more misaligned planets are around cooler stars, but with only four planets this is not statistically significant. There are also some problems for interpretation caused by individual planets in this sample. Both HD 80606 b and HD 17156 b have highly eccentric orbits which bring them within a few stellar radii of their stars at periastron, and thus are sometimes considered to be hot Jupiters or proto hot Jupiters. The Rossiter-McLaughlin effect for Kepler-420 b was only marginally detected by Santerne et al. (2014), and so its spin-orbit misalignment is very uncertain. The compilation of literature data used to produce this figure is listed in Table A.2.

aligned.

The spin-orbit misalignment distribution of a population may also be evaluated as an ensemble in a statistical manner. Mazeh et al. (2015) presented evidence that the predominantly aligned planetary population of cool stars extends out to longer orbital periods than probed previously–at least 50 days. They achieved this by studying the amplitude of photometric variations due to rotation for *Kepler* planet candidate hosts as compared to stars that *Kepler* observed but for which no planets were detected. They found that the cool planet hosts have, on average, higher photometric amplitudes, which would be expected if they are on average more equator-on, consistent with predominantly aligned orbits. Conversely, Mazeh et al. (2015) also found that hot planet host stars have *lower* amplitudes than the hot star control sample, suggesting that they are predominantly misaligned and that misaligned planetary orbits around hot stars are not limited to the population of hot Jupiters. Li & Winn (2016) performed a similar analysis on the cool *Kepler* planet candidate hosts, and concluded that systems with an innermost planet period $P < 10$ days are predominantly aligned, but misalignments grow outside of this period, and systems with $P > 30$ days are consistent with an isotropic distribution of misalignments. This is puzzling in part because tides are expected to be largely ineffective for aligning planets with $P > 10$ days, yet there is some preference for alignment out to ~ 30 days.

In short, small number statistics are currently the greatest obstacle to interpreting the spin-orbit misalignment distributions of every population except hot Jupiters, but there are tentative suggestions that multiplanet systems are typically aligned (although there is also conflicting evidence), even too far out for tides to have had a significant impact–but that even multiplanet systems around hot stars may be misaligned to long orbital periods.

1.2 Generation of Misalignments

As I have described, many hot Jupiters, and a few smaller planets and planets in multiplanet systems, have been shown to have highly misaligned orbits. A huge variety of theoretical models have been proposed to account for these orbital misalignments. In general, these models fall into two classes: either the planets were emplaced on highly-inclined orbits by whatever process brought them close to the star; or, the planet's orbit is misaligned due to other processes unrelated to planet migration. Many of these models only deal with misaligned hot Jupiters, as these are the class about which the most is known.

1.2.1 Misalignments through Planet Migration

After the discovery of the first hot Jupiter, 51 Peg b (Mayor & Queloz 1995), it was quickly realized that it would be very difficult to form such planets *in situ*; therefore, these planets likely formed much farther from their stars, beyond the snow line, and subsequently migrated in to where we see them today (e.g., Lin et al. 1996; Rasio & Ford 1996).

All of the migration mechanisms which could result in spin-orbit misalignments belong to a class of models known as "high-eccentricity migration." In all of these scenarios, the proto-hot Jupiter is put onto a highly eccentric orbit which brings it close to its host star. It can then undergo tidal damping, which reduces its semi-major axis and eventually leaves it on a circular orbit close to its host star. I note that there are also varieties of high-eccentricity migration which cannot generate spin-orbit misalignments, such as coplanar high-eccentricity migration (Petrovich 2015).

1.2.1.1 Planet-Planet Scattering

One of the first mechanisms suggested for hot Jupiter migration could also generate spin-orbit misalignments: planet-planet scattering. This mechanism was originally proposed by Rasio & Ford (1996) soon after the discovery of 51 Peg b. It was not, however, until the later work of Chatterjee et al. (2008) that it was recognized that planet-planet scattering could result in spin-orbit misalignments.

The operation of planet-planet scattering relies upon dynamical instabilities. In this scenario, a system of multiple closely-packed giant planets forms. The protoplanetary disk damps out orbital eccentricities and stabilizes the system, but once the disk dissipates the planets are free to interact and the system becomes unstable. Eccentricities increase until the planets can experience close encounters, which can "slingshot" planets into very different orbits. Planets may be ejected from the system, or crash into the star. Some planets will be put onto orbits with pericenter distances small enough to experience significant tidal damping during pericenter passages, but large enough that the planet is not tidally disrupted and does not impact the star. The tides will extract orbital energy from the planet, shrinking its semi-major axis until it is eventually left on a circular orbit close to the star–i.e., it is a hot Jupiter. The close dynamical encounters between planets that lead to highly eccentric orbits can also significantly alter the planets' orbital inclinations–that is, the spin-orbit misalignments. Planet-planet scattering is thus capable of producing misaligned hot Jupiters.

There is evidence that planet-planet scattering does indeed operate. Dawson & Murray-Clay (2013) found that warm Jupiters (in this case, Jovian planets with 10 days $< P <$ 100 days) around metal-rich stars ([Fe/H] > 0) are preferentially found on more eccentric orbits than those around metal-poor stars. This is precisely what is expected from planet-planet scattering–due to the well-known planet-metallicity correlation (Fischer & Valenti 2005), metal-rich stars are expected to more readily form the systems of multiple closely-spaced giant planets that are the initial conditions for planet-planet scattering than metal-poor stars are. Planet-planet scattering, however, cannot account for all warm Jupiters (and, by extension, all hot Jupiters)– another mechanism (likely smooth migration with the protoplanetary disk) must be invoked to account for the population of low-eccentricity warm Jupiters around low-metallicity stars in the sample of Dawson & Murray-Clay (2013).

1.2.1.2 The Kozai-Lidov Mechanism

Another well-studied dynamical mechanism for planet migration and misalignment is the Kozai-Lidov mechanism, which was discovered by Kozai (1962) and Lidov (1962) in the context of orbital perturbations in our own solar system. In the Kozai-Lidov mechanism, perturbations to the orbit of an inner companion (in this case, a planet) by a more distant perturber (either another planet or a stellar companion) on an inclined orbit cause cyclical exchange between the eccentricity and inclination of the inner orbit, while the semi-major axis remain constant. This can cause both the eccentricity and the inclination to simultaneously reach very high values–i.e., the planet can reach a highly eccentric, highly misaligned orbit. Once this occurs, just as for planet-planet scattering, tidal friction can then reduce the semi-major axis and leave the planet as a highly inclined hot Jupiter (Fabrycky & Tremaine 2007).

More recent work (Naoz et al. 2011, 2012, 2013) has overcome some shortcomings of earlier analyses, allowing them to identify new behavior and a larger parameter space over which this eccentric Kozai-Lidov mechanism may operate. Naoz et al. (2012) found that the Kozai-Lidov mechanism could account for $\sim 30\%$ of the population of hot Jupiters.

Additionally, Dawson & Chiang (2014) provided evidence that Kozai migration due to an outer eccentric *planetary* companion does produce some warm Jupiters. They showed that for known warm Jupiters with eccentric massive outer companions, the separation between the apsides of the two orbits are preferentially around 90°, which is expected for this migration scenario. These warm Jupiters, then, are currently undergoing Kozai-Lidov cycles that will eventually turn them into hot Jupiters, but the cycle periodicity is much longer than for a typical stellar companion and so the overall orbital evolution toward the final hot Jupiter state is much slower.

Most of the work to date on the Kozai-Lidov mechanism in planetary systems has been confined to the case of a single planet with an outer perturber. A different approach was taken by Kaib et al. (2011), who studied a specific system, 55 Cnc. This system consists of five planets detected via radial velocities, with orbital periods ranging from 0.74 to 4900 days (e.g., Endl et al. 2012), as well as an M dwarf at a distance of $\sim$ 1000 AU (Mugrauer et al. 2006). Kaib et al. (2011) found that, due to the gravitational interactions among the planets, Kozai cycles could not cause significant migration; rather, the entire planetary system would exhibit essentially solid-body precession of the system's orbital plane. Bourrier & Hébrard (2014) found a highly-inclined orbit for the transiting super-Earth 55 Cnc e using the Rossiter-McLaughlin effect, which, if confirmed (using the same instrument, López-Morales et al. 2014, did not detect the Rossiter-McLaughlin effect for 55 Cnc e), would be a confirmation of the validity of the Kaib et al. (2011) mechanism. By extension to other systems, this mechanism could result in large spin-orbit misalignments for multiplanet systems with a binary companion.

1.2.1.3 Chaotic Orbital Evolution

Barnes et al. (2015b) studied the orbital evolution of systems of planets in mean motion resonances with non-zero initial eccentricities and inclinations. They found that these parameters can evolve chaotically, resulting in very large values of eccentricities and inclinations that, like the previously-discussed mechanisms, could result in the formation of highly misaligned hot Jupiters. Intriguingly, systems can remain apparently stable for up to 10 Gyr before suddenly destabilizing, resulting in the emplacement of "new" hot Jupiters even around old stars. There is indeed a population of systems of giant planets in mean motion resonance with eccentric orbits (e.g., Robertson et al. 2012). Mutual inclinations between planets are difficult to measure for non-transiting systems, but systems with large mutual inclinations do exist; McArthur et al. (2010) found a mutual inclination of 30° between the non-transiting giant planets υ And c and d (although these planets are not in a mean motion resonance).

1.2.1.4 Constraints on High-Eccentricity Migration

One difficulty for high-eccentricity migration mechanisms is that there should be a population of highly eccentric proto-hot Jupiters which are in the process of migrating (Socrates et al. 2012). Dawson et al. (2015) searched for such planets in the sample of *Kepler* planet candidates, and found fewer than expected. This allowed them to show that less than 44% of hot Jupiters with periods longer than three days can have been formed by Kozai interactions with a stellar perturber; limits are less stringent for planet-planet scattering if a chain of scattering events more slowly shrinks the orbit.

1.2.2 Other Misalignment Mechanisms

1.2.2.1 Misaligned Protoplanetary Disk

One of the most-studied planetary migration mechanisms is migration due to gravitational and tidal interactions between a planet and a protoplanetary disk (e.g., Lin et al. 1996; Kley & Nelson 2012). This should typically result in well-aligned planetary orbits, and so is not in and of itself a misalignment mechanism. However, several authors have argued that if the protoplanetary disk *itself* is misaligned, migration within this disk can naturally result in misaligned planetary orbits.

The first to consider this possibility were Bate et al. (2010). They studied the possibility that, if the bulk angular momentum of material accreted by a protostar is time-variable, this could result in a misalignment between the stellar spin axis and the protoplanetary disk. That is, the early-accreted material that forms the star has some bulk angular momentum, and the later-accreted material that forms the disk during the planet-forming epoch has a different bulk angular momentum and will thus rotate in a different direction than the star. Due to the chaotic nature of star-forming environments, this mechanism could in principle operate commonly. Bate et al. (2010) found, however, that this mechanism is only efficient in producing misaligned planets if both the disk is truncated by a dynamical encounter with another object in the protostellar cluster, which locks in the disk misalignment at the value appropriate to the angular momentum of the most recently-accreted material; and, if this truncated disk still contains enough material to form planets. Further work on this mechanism was conducted by Fielding et al. (2015), who focused on the outer parts of the disk rather than the inner disk as had Bate et al. (2010). They found that this mechanism could produce spin-orbit misalignments much more readily than Bate et al. (2010) had. The simulations of Fielding et al. (2015), however, over-produced aligned hot

Jupiters and under-produced retrograde ones as compared to observations, and so either additional physics or an additional migration mechanism would be required to explain the full spin-orbit misalignment distribution.

Another mechanism to misalign a protoplanetary disk was proposed by Batygin (2012), and has been further investigated by Batygin & Adams (2013), Lai (2014), Spalding et al. (2014) and Spalding & Batygin (2015). In these models, the protoplanetary disk is torqued out of alignment with the host star either by a binary companion (which may be only temporarily bound), or the gravitational potential of the birth cluster as a whole. Like the model of Bate et al. (2010), migrating planets within this misaligned disk would naturally end up on misaligned orbits. Most interestingly, Spalding et al. (2014) found that the stronger magnetic fields of lower mass T Tauri stars are able to realign the stars with the misaligned disk, whereas the weaker fields of more massive stars are not. This would provide a natural explanation for the dichotomy in the spin-orbit misalignment distribution of hot Jupiters found by Winn et al. (2010a).

Finally, Lai et al. (2011) and Foucart & Lai (2011) studied the interaction between the protostellar magnetic field and the protoplanetary disk, and found that in some cases the magnetic field could torque the star out of alignment with the disk.

1.2.2.2 Angular Momentum Transport within Hot Stars

Another mechanism for generating misalignments–one of the few which also itself explains the dichotomy found by Winn et al. (2010a)–was proposed by Rogers et al. (2012) and expanded in Rogers et al. (2013). They performed hydrodynamic simulations of the action of gravity waves to redistribute angular momentum within hot stars. They found that such internal gravity waves can efficiently transport angular momentum on short timescales, and, as a result, the rotation of the stellar atmosphere may not be reflective of the bulk stellar angular momentum. They found that the stellar atmosphere could even develop a rotation in the sense *opposite* that of the stellar bulk angular momentum. Since in most cases when we measure the spin-orbit misalignment of a planet we are measuring it with respect to the visible stellar surface, this effect would give the appearance of a misalignment even when the planetary orbital angular momentum vector is in fact well-aligned with the stellar bulk angular momentum. Because only hot stars would exhibit this behavior, this would naturally explain the Winn et al. (2010a) finding that misaligned hot Jupiters are found around hot stars and not around cool stars. The simulations of Rogers et al. (2012) and Rogers et al. (2013), however, were carried out in 2D, and to date no 3D simulations to investigate this phenomenon have been published. Nonetheless, there is some observational evidence for this phenomenon, as Triana et al. (2015), using asteroseismology, found that the envelope of a B star observed by *Kepler* rotates in the opposite sense to its core; this star, however, is significantly more massive than the planet hosts stars considered by Rogers et al. (2012) and subsequent works.

1.2.3 The Role of Tides in Damping Misalignments

Most of the misalignment mechanisms described above should operate regardless of the stellar properties–with the exception of the mechanisms of Rogers et al. (2012) and Spalding & Batygin (2015), these mechanisms are incapable of reproducing the distribution of λ as a function of T_{eff} for hot Jupiters by themselves. One or more of these mechanisms must be invoked to emplace some fraction of hot Jupiters on misaligned orbits, and then a separate mechanism is needed to damp out the misalignments of planets around cool stars, but not hot stars.

The fact that the break in the distribution occurs at $T_{\rm eff} \sim 6250\,{\rm K}$ is likely a crucial clue. This is the point on the main sequence below which stars have deep, massive convective layers near their surfaces, whereas those above this point do not. Winn et al. (2010a) hypothesized that planets around cooler stars are able to efficiently tidally couple to the massive stellar convection zone, and thus quickly damp out spin-orbit misalignments, whereas those around more massive stars are not. Albrecht et al. (2012b) showed that misalignments do indeed correlate with the expected relative tidal damping timescale. Dawson (2014) demonstrated that tidal damping could explain both the spin-orbit misalignment dichotomy found by Winn et al. (2010a) and the lack of massive retrograde planets identified by Hébrard et al. (2011b), as well as an inverse relationship between the stellar rotation period and planetary mass for cool stars hosting hot Jupiters.

While it appears that tidal damping of misaligned orbits is consistent with the observed spin-orbit misalignment distributions, there are still significant challenges and theoretical uncertainties for these processes. Rogers & Lin (2013) showed that, if tides are to damp out misalignments while not also causing swift orbital decay that would result in the destruction of the planets, then spin-orbit misalignments must be driven to 0°, ±90°, and 180°, not only 0° as observed. Xue et al. (2014), however, showed that the latter states will eventually decay to the aligned state. Li & Winn (2016) investigated tidal realignment and decay in more detail, taking into account both the tides themselves and magnetic braking of the stellar rotation, and showed that tides can, in fact, realign initially misaligned planets without causing significant orbital decay, but that there should still be a population of planets with λ near ±90° and 180° for somewhat longer-period orbits where tidal damping is less efficient. The conclusions of Li & Winn (2016), however, required some fine-tuning of the tidal quality factors and stellar rotation rate.

An alternative model to explain the Winn et al. (2010a) dichotomy was proposed by Matsakos & Königl (2015). They suggested that most stars produce Jupiter-mass planets very early on in disks misaligned due to the mechanisms of Bate et al. (2010) or Batygin (2012); these planets then migrate close in to the star and are ingested within a Gyr. For cool stars the angular momentum of the ingested planet will be larger than that due to the stellar rotation, and so the star will realign to the orbital plane of the ingested planet (which is presumably shared by any remaining planets). For hot stars, on the other hand, the stellar rotational angular momentum will be greater than that of the ingested planet, and so the star will retain its original orientation. Their models were able to reproduce the dichotomy of Winn et al. (2010a), the lack of retrograde massive planets (Hébrard et al. 2011b), the inverse correlation between stellar rotation and planetary mass for cool hot Jupiter hosts (Dawson 2014), and the alignment of planetary systems around cool stars out to large orbital period (Mazeh et al. 2015).

1.2.4 The Current State of the Field

As I have discussed in the preceding sections, a great deal of theoretical work has been invested in determining the reasons for the existence of spin-orbit misalignments and the various trends that have been observed, but observations to determine *which* mechanisms are dominant in reality have lagged behind the theory. There is somewhat conflicting observational evidence that many warm Jupiters migrate via planet-planet scattering (Dawson & Murray-Clay 2013), but also that at least some warm Jupiters are produced by Kozai-Lidov cycles due to an outer planetary companion (Dawson & Chiang 2014). About 30% of hot Jupiters could be produced by the Kozai-Lidov mechanism (Naoz et al. 2012), which is consistent with the results of Dawson et al. (2015) that no more than 44% of hot Jupiters could be produced by Kozai-Lidov cycles due to a planetary companion. To date there are no good observational constraints on the frequency and efficacy of other misalignment mechanisms, such as the disk-tilting mechanisms of Bate et al. (2010) or Batygin (2012), or the stellar rotation changes of Rogers et al. (2012).

With the currently available data it seems most likely that some fraction of hot Jupiters are emplaced by disk migration, and some fraction by planet-planet scattering and/or Kozai-Lidov cycles. However, the relative contributions of the different migration mechanisms, and the extent to which (or even if) other mechanisms affect the spin-orbit misalignment after a hot Jupiter has been emplaced, are still under debate. In order to solve this problem, a multi-pronged approach is required. Obviously a significant component must be the measurement of a statistically significant sample of misalignments for classes of planets other than hot Jupiters. What is the misalignment distribution of warm Jupiters? Planets in multiplanet systems? Single small planets? And how do these distributions differ for hot and cool stars? Different models make different predictions for the spin-orbit misalignment distribution of these classes of planets, and so such observations may be used to differentiate among the different mechanisms. Ensemble results using asteroseismology (e.g., Campante et al. 2016) and the amplitude of stellar rotational variability (Mazeh et al. 2015; Li & Winn 2016) are suggestive, but direct measurement of λ for more longer-period planets and multiplanet systems will allow for finer-grained and more accurate investigation of the spin-orbit misalignment distributions.

Ancillary observations to detect (or exclude) the presence of additional companions in the system are also important, as several of the migration models rely upon the presence of such companions (most notably, planet-planet scattering and the Kozai-Lidov mechanism). Surveys are underway to systematically detect such companions, through the detection of radial velocity trends that could indicate the presence of an additional planet or a nearby stellar companion (e.g., Covino et al. 2013; Knutson et al. 2014), searches for secondary lines due to stellar companions at moderate separations (Piskorz et al. 2015), and direct imaging observations to detect wide separation stellar companions (e.g., Ngo et al. 2015, 2016). The work of Knutson et al. (2014), Piskorz et al. (2015), and Ngo et al. (2015) did not find any correlation between the presence of companions on any of these scales and the spin-orbit misalignments or orbital eccentricities of the hot Jupiters in such systems. In Fig. 1.11 I show the companion status of known hot Jupiters. Such ancillary observations will continue to be important for systems with warm Jupiters, multiplanet systems, and small planets with measured spin-orbit misalignments.

In this dissertation I contribute to solving these problems with Doppler tomography, by expanding the number of hot and warm Jupiters with spin-orbit misalignment measurements. I describe these efforts in Chapter 3.

1.3 Planets around Intermediate-Mass Stars

The large majority of known exoplanets orbit approximately solar-type stars, with a steep drop-off in the number of known planets around a spectral type of mid F. There is no physical reason to expect a sharp drop in the planet occurrence rate; this drop is likely due to observational biases, not an actual change in occurrence rates. As can be seen in the bottom panel of Fig. 1.7, at approximately this spectral type the rotation rates of stars begin to increase, due to lower magnetic field strengths and thus lessened braking of rotation (e.g., Kraft 1967, after whom this is called the

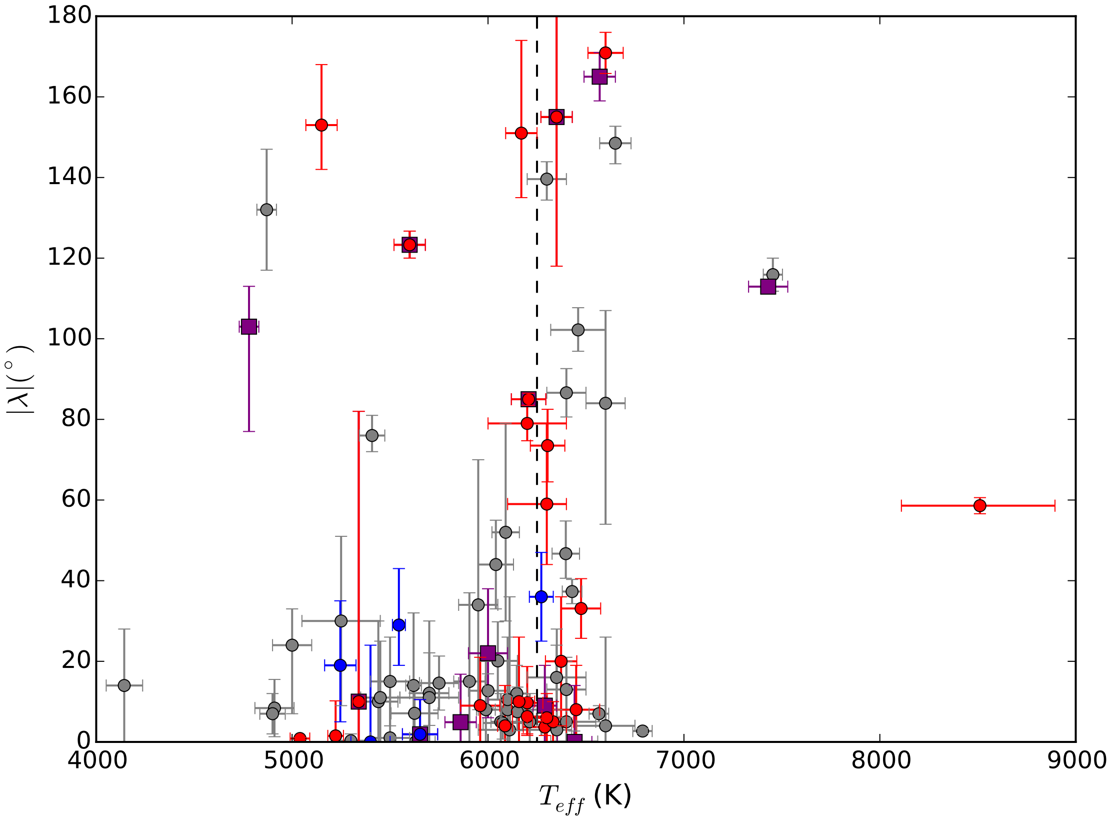

Figure 1.11 Similar to Fig. 1.7, showing the measured spin-orbit misalignments of hot Jupiters from the literature as a function of stellar $T_{\rm eff}$. Here, the symbol color and shape denotes the presence (or lack thereof) of additional object(s) in the system. Red circles show hot Jupiters in systems with a known stellar companion, blue circles those with one or more known planets in the system (in most case detected through radial velocity observations), and purple squares those with a radial velocity trend (some overlap with the previous two categories). Gray circles denote hot Jupiters with no evidence for additional objects in the system, although in many cases there has been no systematic search for such companions. The compilation of literature data used to produce this figure is listed in Table A.1.

Kraft break). The rapid rotation results in wide, rotationally broadened spectral lines, which prevent the measurement of the stellar radial velocity to the precision necessary for the detection of reflex motion due to even a massive planetary companion. For this reason, radial velocity planet searches typically exclude stars with $v \sin i_\star > 15 - 20$ km s^{-1}. Currently, the only planet discovered by radial velocities around a more rapidly rotating star is the very massive planet 30 Ari Bb, whose host star has $v \sin i_\star = 38$ km s^{-1} (Guenther et al. 2009).

Transit surveys are capable of discovering planets around intermediate-mass ($\sim 1.5 - 2.5 M_\odot$) stars, and, indeed, a number of such planets have been detected, the first and most well-studied being the hot Jupiters WASP-33 b (Collier Cameron et al. 2010b) and Kepler-13 Ab (e.g., Szabó et al. 2011). Such stars, however, have typically not been targeted by transit surveys due to the difficulty of following up and confirming transiting planet candidates without precise radial velocities. Ground-based wide-angle planet searches can find such candidates, but they are often not followed up. *Kepler* observed ~ 5000 intermediate-mass stars, and found ~ 60 planet candidates, but these numbers are dwarfed by the $\sim 150,000$ FGK stars observed and ~ 4500 planet candidates found around these stars (e.g., Coughlin et al. 2016). These discoveries give a tantalizing glimpse into the short-period planetary population of intermediate-mass stars, but most of these candidates are still unconfirmed, and the numbers of known planets are insufficient to allow the same kinds of statistical explorations of the population that *Kepler* enabled for FGKM stars (e.g., Howard et al. 2012; Petigura et al. 2013; Dressing & Charbonneau 2013; Mulders et al. 2015).

Other methods can also discover planets around intermediate-mass stars. Direct imaging has been successful in finding wide-separation giant planets around these stars; indeed, a large fraction of the known directly imaged planets orbit such stars

(Kalas et al. 2008; Lagrange et al. 2009; Macintosh et al. 2015; Wagner et al. 2016), most notably the remarkable four-planet system around HR 8799 (Marois et al. 2008, 2010). Since this method uses imaging rather than spectroscopy, the rotational properties of the host star do not affect the ability to detect planets. Indeed, intermediate-mass stars are perhaps *better* targets for direct imaging than solar-type stars, due to their typically small ages (resulting in brighter planets) and possible higher occurrence rate of wide-separation giant planets (e.g., Crepp & Johnson 2011).

While the typical fast rotation of intermediate-mass stars is an impediment to radial velocity observations, a loophole is provided by stellar evolution. These stars only rotate rapidly while they are on the main sequence–as they begin to evolve off of the main sequence, their radii expand and, due to conservation of angular momentum, their spins slow enough that they become amenable to radial velocity observations. They also cool, which increases the number of lines in their spectra, also increasing their suitability for radial velocity observations. Several teams have targeted subgiants and giants in this mass range for radial velocity observations, and have found many giant planets (e.g., Johnson et al. 2007; Reffert et al. 2015). Indeed, Reffert et al. (2015) compiled a sufficiently large sample of giant planets around giant stars to find that the planet occurrence rate (as a function of stellar mass) increases up to $\sim 1.9\,M_{\odot}$, but declines rapidly beginning at $\sim 2.5\,M_{\odot}$; they did not find any planets around the many stars in their sample with $M_{\star} > 2.7\,M_{\odot}$. There has, however, been significant controversy over the masses of these giants and subgiants, and whether they are actually intermediate-mass stars or are in fact lower mass (Lloyd 2011, 2013; Johnson et al. 2013; Schlaufman & Winn 2013). Controversies over the actual masses of these stars notwithstanding, this remains the best method to probe the giant planet population of intermediate-mass stars at intermediate separations

(a ∼a few AU).

Both of these methods have limitations, however, most notably that they are both only sensitive to giant planets. Furthermore, state-of-the-art direct imaging facilities are only now reaching the small inner working angles necessary to image companions on solar system scales–51 Eri b, the closest directly imaged planet discovered to date, is at a projected separation of 13 AU from its host star (Macintosh et al. 2015). Direct imaging can thus only probe very wide separation giant planets. Radial velocity surveys of giants and subgiants can only discover planets out to orbital periods similar to the survey timespan–currently $\sim 10-15$ years–and are additionally limited on the short-period end. As these stars evolve off the main sequence and their radii expand, they engulf and destroy any short-period planets (e.g., Schlaufman & Winn 2013). Both radial velocity and direct imaging surveys are thus incapable of probing the short-period planetary population of intermediate-mass stars.

Transit surveys plus Doppler tomographic validation provides a method to investigate the short-period planetary population of intermediate-mass stars that is inaccessible to both direct imaging and radial velocity surveys of (sub)giants. The detection of the Doppler tomographic transit signature of a planet candidate shows that it orbits the target star–it is not a background eclipsing binary blended with the light of a foreground star, or another astrophysical false positive scenario. The limitation, however, is that Doppler tomography alone gives no constraints on the mass of the companion. Objects' radii are approximately constant over masses from ~ 1 to $\sim 90\,M_J$, and so neither Doppler tomography nor transit photometry can distinguish among a transiting Jovian planet, brown dwarf, or very late M dwarf. Even if radial velocity observations of rapidly rotating stars cannot detect the stellar reflex motion, they can still set limits on this motion which are often sufficient to limit the companion mass to the planetary regime (e.g., Lillo-Box et al. 2015). Alternately, if the star is photometrically quiet, and space-based photometry is available, the planetary mass can be measured (or constrained) by the detection (or non-detection) of photometric modulations in phase with the planetary orbit due to tidal distortion of the host star and relativistic beaming effects; this has, for instance, been used to measure the mass of the hot Jupiter Kepler-13 Ab (Szabó et al. 2012; Mislis & Hodgkin 2012; Mazeh et al. 2012; Esteves et al. 2013; Placek et al. 2014). The combination of showing that the planet candidate orbits the target star, and that its mass is in the substellar regime, confirms that the planet candidate is indeed a planet.

Doppler tomography, radial velocity observations of (sub)giants, and direct imaging are actually thus very complimentary. Together, these three techniques have the potential to piece together the occurrence rate of giant planets around intermediate-mass stars as a function of semi-major axis all the way from 0.01 AU to hundreds of AU. Of course, more observations are necessary, especially to boost the number of transiting planets and directly imaged planets around intermediate-mass stars to the point where robust statistical inference is possible; nonetheless, this should be possible within the next few years to a decade.

In this dissertation I pursue Doppler tomographic observations of *Kepler* planet candidates around rapidly rotating stars in an attempt to confirm them as *bona fide* planets. I describe this work in Chapter 4. My Doppler tomographic observations of Kepler-13 Ab (§3.1) and Kepler-448 b (§3.2) also technically validate these planets, although these planets have already been validated by Szabó et al. (2012) and Bourrier et al. (2015), respectively.

Chapter Two: Methodology[1]

2.1 Observations

Doppler tomographic observations are challenging because they require high signal-to-noise spectra with both high spectral and temporal resolution. Ideally, each spectrum will have a signal-to-noise ratio SNR > 100 in the region of the spectrum where there are both many spectral lines and optical spectrographs typically have high throughput ($\sim 4000 - 6000$ Å). High spectral resolution is needed to adequately resolve the rotationally broadened stellar lines and the line profile perturbation. Typically, a spectral resolving power $R > 30,000$ is necessary, while very high resolution spectrographs ($R > 100,000$) allow the use of Doppler tomography for stars rotating as slowly as a few km s^{-1} (e.g., Collier Cameron et al. 2010a). In terms of time resolution, ideally the exposure time will be such that the planetary transit signature moves less than one resolution element across the line profile during the exposure; for a typical hot Jupiter, this requires that exposure times be approximately < 1200 s. This condition will minimize blurring of the line profile perturbation due to its motion. The combination of the requirements for high spectral and temporal resolution and high signal-to-noise ratio impose that Doppler tomographic observations require large telescopes in order to gather sufficient signal in a short amount of time.

---

[1] Much of the material in this chapter was originally published in Johnson, M. C., Cochran, W. D., Albrecht, S., Dodson-Robinson, S. E., Winn, J. N., & Gullikson, K., 2014, ApJ, 790, 30. Author contributions: M.C.J. adapted Doppler tomographic methodology described in the literature and added innovations such as fitting the line depths, performed some of the data reductions, and wrote the code to perform the Doppler tomographic analysis and the paper. S.A. assisted with the Doppler tomographic methodology and provided advice on writing the code. W.D.C. performed some of the data reductions. W.D.C., S.E.D.-R., and J.N.W. assisted with discussion of methodology. K.G. did not contribute to the Doppler tomographic methodology.

Almost all of my observations were obtained with two telescopes located at McDonald Observatory, the 9.2 m Hobby-Eberly Telescope (HET) and the 2.7 m Harlan J. Smith Telescope (HJST). The HET has a fixed-altitude design, and as a consequence it can typically observe a given target for only ~ 1 hour at a time. Therefore, in order to perform Doppler tomographic observations with the HET, it is typically necessary to observe parts of multiple transits and stitch these datasets together. The HET utilizes a fiber-fed cross-dispersed échelle spectrograph, the High Resolution Spectrograph (HRS; Tull 1998). My HRS observations were obtained with a resolving power $R = 30,000$, and cover ~ 4770 Å to ~ 6840 Å. All of these observations occurred prior to 2013 August, when the HET was taken offline for the Wide Field Upgrade.

The Robert G. Tull Spectrograph (Tull et al. 1995) on the HJST is also a cross-dispersed échelle spectrograph, but uses a more traditional slit coudé feed. I used the TS23 spectrograph configuration; these data have $R = 60,000$, and wavelength coverage from ~ 3750 Å to ~ 10200 Å, with complete coverage blueward of 5691 Å. I did not use any of the orders redward of ~ 8500 Å for the Doppler tomographic analysis, however, due to telluric contamination and lack of stellar lines. Due to the much smaller aperture of the HJST as compared to the HET, I only used it for my brightest targets ($V < 10$), although I found empirically that it is only effective for Doppler tomographic observations of Jovian planets transiting stars with $V < 9$.

Only a few of the datasets described in this work were obtained with other facilities. These other facilities are described in the same section as each relevant dataset, namely the AAT/UCLES observations of WASP-79 b (shared with me by Addison et al. 2013, and analyzed in §3.3), and my photometric observations of WASP-33 b with LCOGT (Chapter 5).

Table 2.1. Summary of Targets

Name	FOM	$v \sin i$ (km s^{-1})	Mag[a]	$T_{\rm eff}$ (K)	P (days)	R_p (R_J)	$N_{\rm obs}$	§	Ref.
WASP-33 b	2.4	90 ± 10	8.3	7430 ± 100	1.220	1.497 ± 0.045	2	5	1
Kepler-13 Ab	0.61	65 ± 10	9.9	8511^{+401}_{-383}	1.764	2.042 ± 0.080	9	3.1	2; 3
Kepler-448 b	0.27	$60.0^{+0.8}_{-0.9}$	11.353	6820 ± 20	17.855	1.43 ± 0.13	3	3.2	4
KOI-368.01	0.23	79 ± 4	11.375	9250 ± 200	110.32	2.053 ± 0.058	2	4.1	5
HAT-P-2 b	0.18	20.8 ± 0.3	8.70	6290 ± 60	5.633	$1.157^{+0.073}_{-0.062}$	2	[b]	6
KOI-959.01	0.18	25 ± 2	13.102	2661 ± 0[d]	12.714	0.22 ± 0[d]	1	[c]	7; 8
WASP-79 b	0.17	19.1 ± 0.7	10.1	6600 ± 100	3.662	1.70 ± 0.11	1	3.3	9
HAT-P-41 b	0.12	19.6 ± 0.5	11.087	6390 ± 100	2.694	$1.685^{+0.076}_{-0.051}$	5	3.4	10
KELT-2 Ab	0.083	9.0 ± 2.0	8.77	6147 ± 50	4.113	$1.307^{+0.077}_{-0.064}$	3	3.5	11
KOI-972.01	0.052	120 ± 5	9.27	7221^{+125}_{-165}	13.119	$0.788^{+0.042}_{-0.22}$	7	4.2	12; 7
KOI-366.01	0.035	35 ± 2	11.71	6201^{+124}_{-107}	75.112	$2.2^{+0.3}_{-0.5}$	1	4.3	12; 7
KOI-4.01	0.013	40	11.43	6244^{+130}_{-109}	3.849	$1.2^{+0.2}_{-0.3}$	2	[c]	7

Note. — Summary of properties for targets analyzed in or observed for this dissertation. I list the targets in order of decreasing figure of merit (FOM; defined in Eqn. 2.1); note that, strictly speaking, the FOM values for *Kepler* and non-*Kepler* targets should not be directly compared as they were calculated using target magnitudes in different bandpasses. $N_{\rm obs}$ lists the number of individual transits during which observations were obtained. The "§" column lists in which section of this dissertation each planet's datasets are analyzed.
References: 1: Collier Cameron et al. (2010b); 2: Szabó et al. (2011); 3: Esteves et al. (2013); 4: Bourrier et al. (2015); 5: Zhou & Huang (2013); 6: Pál et al. (2010); 7: Coughlin et al. (2016); 8: $v \sin i_\star$ values obtained by the *Kepler* Community Follow-Up Program (CFOP; https://exofop.ipac.caltech.edu/cfop.php); 9: Smalley et al. (2012); 10: Hartman et al. (2012); 11: Beatty et al. (2012); 12: Lillo-Box et al. (2015).

[a] *Kepler* magnitude (Kp) for *Kepler* targets (except Kepler-13), V magnitude for other targets.

[b] HAT-P-2 b was observed during the early stages of this project in order to serve as a test case to show that my methodology could reproduce published results; its spin-orbit misalignment has been measured by multiple authors (Winn et al. 2007b; Loeillet et al. 2008; Albrecht et al. 2012b). The WASP-33 dataset from the HJST/TS23 originally published by Collier Cameron et al. (2010b), however, ultimately proved to be a sufficient test, and so I did not analyze my observations of HAT-P-2 b any further.

[c] KOI-4.01 and KOI-959.01 were initially announced as planet candidates by Borucki et al. (2011), and so partial transits of both objects were observed with the HET. They were subsequently dispositioned as false positives by Burke et al. (2014), and so I did not proceed with data analysis. The most recent *Kepler* data release, however, has redispositioned both objects as planet candidates (Coughlin et al. 2016), although KOI-959 was listed in the Slawson et al. (2011) catalog of *Kepler* eclipsing binaries. I have not yet had time to restart the analysis of these data.

[d] The very low quoted $T_{\rm eff}$ and R_P for KOI-959 with zero claimed uncertainties are likely spurious.

I selected Doppler tomographic targets from two sources: the evolving catalogs of *Kepler* planet candidates (e.g., Borucki et al. 2011; Batalha et al. 2013; Coughlin et al. 2016), with $v \sin i_\star$ values taken from the *Kepler* Community Follow-Up Program's[2] reconnaissance spectroscopy observations, and transiting hot Jupiters described in the literature. In order to assess the relative suitability of the different targets I constructed a figure of merit for ranking the candidates,

$$\mathrm{FOM} = v \sin i_\star \left(\frac{R_P}{R_\star}\right)^2 10^{-0.2(M-10)} \sqrt{1-b^2} \tag{2.1}$$

where M is the stellar apparent magnitude (V for non-*Kepler* targets and *Kepler* bandpass magnitude Kp for *Kepler* targets, which I assessed separately); it enters into the figure of merit through a square root flux term to account for the attainable SNR. This figure of merit is based upon an expression for the radial velocity Rossiter-McLaughlin amplitude provided by Andrew Collier Cameron (cf. Eqn. 1.1). I list all of the targets that I observed in Table 2.1, and the details of each individual observation in Table 2.2.

Table 2.2. Log of Observations

Planet	Date (UT)	Instrument	Transit Phases	SNR	N_{spec}
WASP-33 b	2008 Nov 12	HJST/TS23	$-0.05 - 1.28$	140	13
KOI-4.01	2011 May 17	HET/HRS	$0.52 - 0.88$	104	7
Kepler-13 Ab	2011 Jun 8	HET/HRS	$0.65 - 0.98$	150	11
Kepler-13 Ab	2011 Jun 15	HJST/TS23	$-0.12 - 1.25$	53	16
Kepler-13 Ab	2011 Jul 6	HET/HRS	$0.03 - 0.48$	198	16

Continued on next page

---

[2] https://exofop.ipac.caltech.edu/cfop.php

Table 2.2, cont.

Planet	Date (UT)	Instrument	Transit Phases	SNR	$N_{\rm spec}$
Kepler-13 Ab	2011 Jul 8	HET/HRS	0.10 – 0.51	183	15
KOI-972.01	2011 Jul 21	HJST/TS23	0.61 – 1.19	124	10
KOI-972.01	2011 Aug 03	HET/HRS	0.84 – 1.19	121	16
KOI-972.01	2011 Aug 16	HET/HRS	0.02 – 0.35	145	15
KOI-366.01	2011 Aug 18	HET/HRS	0.30 – 0.51	40	7
Kepler-13 Ab	2011 Aug 21	HET/HRS	0.21 – 0.66	162	16
KOI-368.01	2011 Aug 29	HET/HRS	0.75 – 0.84	125	7
Kepler-13 Ab	2011 Sep 13	HET/HRS	0.29 – 0.71	172	15
KOI-972.01	2011 Nov 03	HET/HRS	0.40 – 0.73	33	15
Kepler-13 Ab	2011 Nov 5	HET/HRS	−0.09 – 0.32	135	15
Kepler-13 Ab	2011 Nov 5	HJST/TS23	−0.08 – 0.85	48	11
HAT-P-2 b	2012 May 13	HET/HRS	0.74 – 1.06	...	...
Kepler-448 b	2012 May 21	HET/HRS	0.66 – 0.85	58	8
Kepler-13 Ab	2012 Jun 7	HET/HRS	0.10 – 0.60	138	17
HAT-P-2 b	2012 Jun 27	HJST/TS23	0.13 – 1.06	185	15
KOI-959.01	2012 Jul 18	HET/HRS	0.11– $\sim$ 0.70	...	...
KOI-368.01	2012 Jul 25	HJST/TS23	0.79 – 1.01	42	9
KOI-972.01	2012 Oct 09	HET/HRS	0.24 – 0.59	137	19
KOI-4.01	2012 Oct 14	HET/HRS	0.52 – 1.00	...	...
KOI-368.01	2012 Oct 28	HET/HRS	template	166	6
KELT-2 Ab	2012 Dec 13	HET/HRS	0.52 – 0.74	162	13
WASP-79 b	2012 Dec 23	AAT/UCLES	−0.06 – 1.5	63	23

Continued on next page

Table 2.2, cont.

Planet	Date (UT)	Instrument	Transit Phases	SNR	$N_{\rm spec}$
KELT-2 Ab	2013 Jan 11	HET/HRS	0.04 – 0.28	114	16
KELT-2 Ab	2013 Feb 22	HET/HRS	template	194	6
KOI-972.01	2013 Mar 01	HET/HRS	template	68	6
KOI-972.01	2013 Mar 02	HET/HRS	0.67 – 0.85	146	10
KOI-972.01	2013 Mar 15	HET/HRS	−0.23 – 0.15	124	19
KELT-2 Ab	2013 Mar 22	HJST/TS23	0.20 – 0.60	163	8
KOI-366.01	2013 Mar 26	HET/HRS	template	…	…
Kepler-448 b	2013 Mar 27	HET/HRS	template	17	6
Kepler-448 b	2013 Apr 25	HET/HRS	0.08 – 0.27	43	8
Kepler-448 b	2013 May 13	HET/HRS	0.40 – 0.59	57	8
HAT-P-41 b	2013 Jun 27	HET/HRS	0.09 – 0.35	68	6
Kepler-13 Ab	2013 Jun 28	HET/HRS	template	120	12
HAT-P-41 b	2013 Jul 08	HET/HRS	0.44 – 0.67	68	6
HAT-P-41 b	2013 Jul 12	HET/HRS	template	59	6
HAT-P-41 b	2013 Jul 24	HET/HRS	0.04 – 0.25	67	7
HAT-P-41 b	2013 Aug 04	HET/HRS	0.29 – 0.59	62	7
HAT-P-41 b	2013 Aug 12	HET/HRS	0.51 – 0.77	82	6
WASP-33 b	2014 Oct 03	HJST/TS23	−0.42 – 1.76	281	21

Note. — Log of all Doppler tomographic observations obtained for or used in this dissertation. I define the "transit phase" such that it equals 0 at ingress and 1 at egress. The quoted signal-to-noise ratio (SNR) is the mean SNR per pixel near 5500 Å for all spectra taken on that night. $N_{\rm spec}$ is the number of spectra obtained during that night's observations. Horizontal lines separate each calendar year of observations.

Once the observations have been obtained, I need to extract and reduce the spectra. In this process, I follow standard methodology to reduce the spectra, using pipelines based on standard IRAF tasks. These are the same pipelines used by the McDonald Observatory Radial Velocity Planet Search Program for HET/HRS (e.g., Cochran et al. 2004) and HJST/TS23 (e.g., Wittenmyer et al. 2006). I then divide the extracted spectra by the blaze-profile function, and remove any residual curvature by fitting a second-order polynomial using a σ-clipping routine and normalizing. The spectra are now ready for Doppler tomographic analysis.

2.2 Line Profile Extraction

The first step in Doppler tomographic analysis is to extract the time series line profiles from my spectra. Essentially, I wish to compute the average line profile for each spectrum. I note that in computing an average line profile across a spectrum I make the assumption that all lines have the same shape, ignoring variations in line shape due to change of the limb darkening parameter as a function of wavelength, different fundamental line parameters which would cause different lines to be formed at different depths in the stellar atmosphere, and any other source of variations in the line profile. As I am interested in the variations in the line profile as a function of time, rather than the detailed line shape, this should not have a significant effect upon my results. Also note, however, that I exclude lines that are very strong (i.e., approaching saturation) and/or highly pressure broadened from the computation of the average line profiles, as these lines will not share the rotational broadening-dominated profile of most of the lines in the spectrum.

I extract the average line profiles from the spectra in several steps. All steps involve fitting a model spectrum to the data. In all cases I produce this model using the least squares deconvolution method of Donati et al. (1997). In this method, a model spectrum is produced by convolving a model line profile with a series of appropriately weighted delta functions at the wavelengths of the spectral lines. I fit this model spectrum to the data using the least squares methods of Markwardt (2009), as implemented in the IDL function `mpfit` and derivatives.

I first select several orders of the spectrum with many telluric lines and few or no stellar lines. I produce a model telluric spectrum with least squares deconvolution using a telluric line list (obtained from the GEISA database[3]), and assuming a Gaussian line profile. I assume that the telluric lines are unresolved, and so I set the width of the Gaussian to an appropriate value given the instrumental resolution. I fit this model spectrum to the data, leaving only the velocity offset between the extracted spectrum and the telluric rest frame as a free parameter. I assume that the telluric rest frame is identical to the spectrograph rest frame (plus or minus the wind speed, which is much smaller than the velocity scales of interest to me), and so I shift the spectra into this frame. Telluric lines have been shown to be a stable velocity standard (e.g., Gray & Brown 2006; Figueira et al. 2010). As an example, the individual spectra display an RMS scatter in the telluric velocities of ~ 250 m s^{-1} for my HET dataset on Kepler-13 Ab, again much smaller than both the velocity scales of interest and the instrumental resolution, although there is a zero-point offset of ~ 6 km s^{-1} between the spectrograph's intrinsic wavelength calibration and the telluric velocity frame. In the cases of my moderately rotating targets ($v \sin i_{\star} \sim 20$ km s^{-1}; HAT-P-41 and WASP-79), however, I found that my method for determining the telluric

---

[3] http://ether.ipsl.jussieu.fr/etherTypo/?id=950

rest frame was insufficiently precise as compared to the line width, and introduced an undesirable line-by-line velocity offset. In these cases I skipped this step. Now that I have a velocity frame fixed to the Earth, I correct for the Earth's orbital and rotational motion and shift the spectra into the solar barycentric rest frame.

Next I co-add each set of spectra taken on each night, creating several nightly master spectra. For each nightly master spectrum I create a model stellar spectrum, using a line list obtained from the Vienna Atomic Line Database (VALD; Kupka et al. 2000). The line list includes the wavelength of each line, as well as a line depth calculated by VALD using stellar model atmosphere parameters appropriate to the target. I produce an analytic rotationally broadened line profile using Eqn. 18.14 of Gray (2005), which is, using the terminology adopted in this dissertation,

$$G(v) = c_1\sqrt{1-\left(\frac{v}{v\sin i_\star}\right)^2} + c_2\left(1-\left(\frac{v}{v\sin i_\star}\right)^2\right) \tag{2.2}$$

where $G(v)$ is the rotationally broadened line profile as a function of velocity v, and

$$c_1 = \frac{2(1-\varepsilon)}{\pi v\sin i_\star(1-\varepsilon/3)} \tag{2.3}$$

$$c_2 = \frac{\varepsilon}{2v\sin i_\star(1-\varepsilon/3)} \tag{2.4}$$

and where ε is the linear limb darkening coefficient.

This profile includes only the effects of rotation; at this stage in the process, I only require an approximately correct line shape. I then fit the model spectrum to each nightly master spectrum, leaving only the velocity offset between the stellar and solar barycentric frames as a free parameter. Now that I have obtained these nightly velocity offsets, I shift all of the spectra into the stellar barycentric rest frame. I note that this assumes that there is no significant acceleration of the star over the course of one night's observations (typically one to a few hours).

Now that all of the spectra are fixed to the same velocity frame, I co-add all of the out-of-transit spectra to create a template spectrum. If there are no out of transit spectra available, I use all of the available spectra and assume that the moving transit signature will be sufficiently washed out as to have a negligible effect on the overall line shape. I create a model spectrum using the same methodology as described above. Here, however, I fix the velocity offset between model and data at zero and leave the depth of each line as a free parameter. I thus obtain best-fit line depths from my high signal-to-noise template spectrum.

The final step is to extract the time series line profiles themselves. For each spectrum I again produce a model spectrum, fixing the line depths at the best-fit values found earlier. Here the free parameters are the depth of the line profile in each pixel. An example of one of these fits is shown in Fig. 2.1. I perform these fits on an order-by-order basis (although for my more slowly rotating, cooler target stars with more lines I split some orders into two pieces), and for each spectrum I compute the average line profile by computing the weighted mean of the line profiles extracted from each order. I weight each order's line profile by the product of the signal-to-noise ratio at the center of that order and the total equivalent width of all lines in that order, after Albrecht et al. (2013). I exclude any orders with noisy line profiles (i.e., the scatter in the continuum is greater than an empirically determined value, which varies from target to target) from the computation of the weighted mean. I also regrid the line profiles from the different orders to a common velocity scale. I then perform the same process on the template spectrum to obtain an out-of-transit template line profile. I subtract this template line profile from each of the time series line profiles, resulting in the time series line profile residuals, which display the transit signature. Alternately, I can subtract a model rotationally broadened line profile (computed as

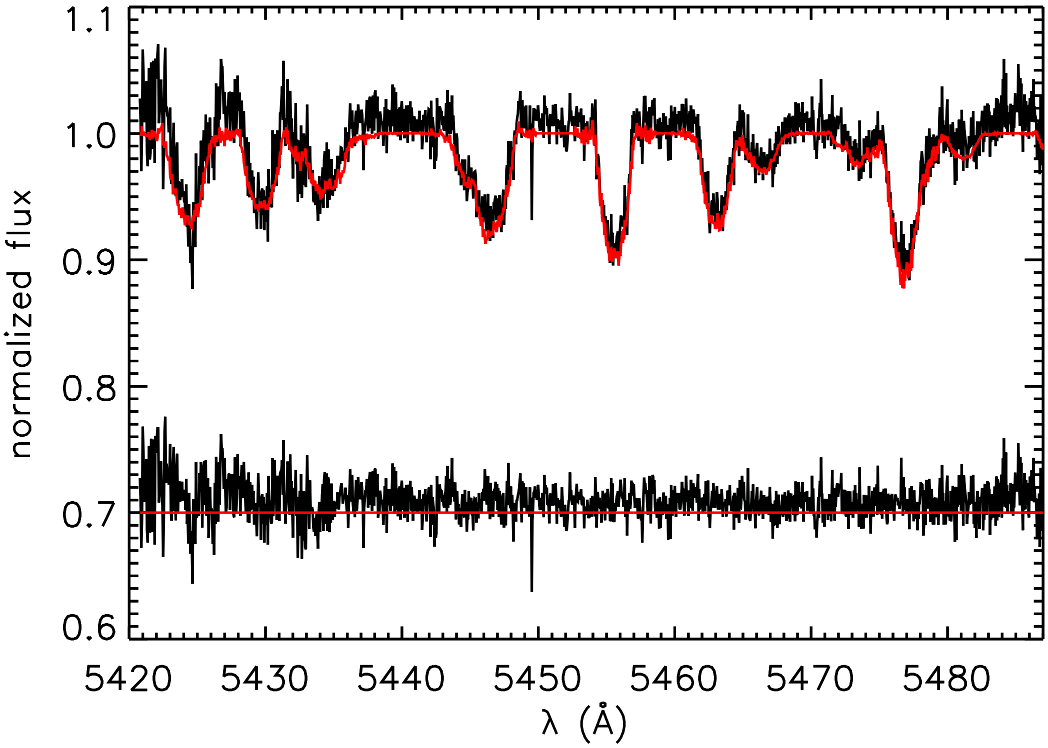

Figure 2.1 One order from one HET spectrum of Kepler-13, showing the final model fit (red) to the spectrum (black). I have shifted the residuals shifted upward by 0.7 in order to better show the spectrum.

described in §2.3) instead of the observationally-determined out-of-transit line profile. The latter method has the advantage of introducing less noise into the time series line profile residuals, but may introduce systematics if the line shape is not reproduced sufficiently well. Which method I use varies on a target-by-target basis depending upon which empirically works best.

In some cases, more specialized methods are needed to deal with the special circumstances of certain systems (e.g., binarity or stellar variability). I will describe these on a case-by-case basis in the sections dedicated to these systems.

2.2.1 Shifting and Binning

The most straightforward method to analyze Doppler tomographic data is to simply fit a model directly to the time series line profile residuals. In some cases, however, especially for small planets and/or faint stars, the line profile perturbation may be too small to be detected in each spectrum in a statistically significant manner. It is therefore desirable to have some method to bin together the time series line profile residuals to increase the signal-to-noise ratio. This is potentially difficult because the path of the line profile perturbation across the line profile is not known *a priori*; naïvely binning all of the time series line profile residuals together will wash out the transit signature, except in the case of a very nearly polar orbit.

I have therefore developed a more sophisticated binning method, which rests upon the following observation. Neglecting differential rotation of the star and assuming a circular orbit for the planet, the rate of motion of the planetary transit signature across the line profile (dv/dt) will be constant. Given the transit duration (calculated from photometric observations of the transit), each value of dv/dt corresponds to a single value of the velocity difference between the locations of the transit signature at ingress and egress, which I denote v_{14}. In geometrical terms, the path of the planetary transit signature in the time series line profile residual plots will be a straight line. For a given value of v_{14}, the transit signature will occur at some velocity v_i in the i^{th} spectrum. I shift each of the n line profile residuals by $-v_i$, such that the transit signature will occur at the same velocity for each shifted line profile residual, and then bin together all of these shifted line profile residuals. If I have the correct value of v_{14}, the transit signatures in each line profile residual will tend to add constructively, and I will obtain a single high signal-to-noise transit signature. If I have an incorrect value of v_{14}, the transit signatures will not add coherently, and the diluted transit

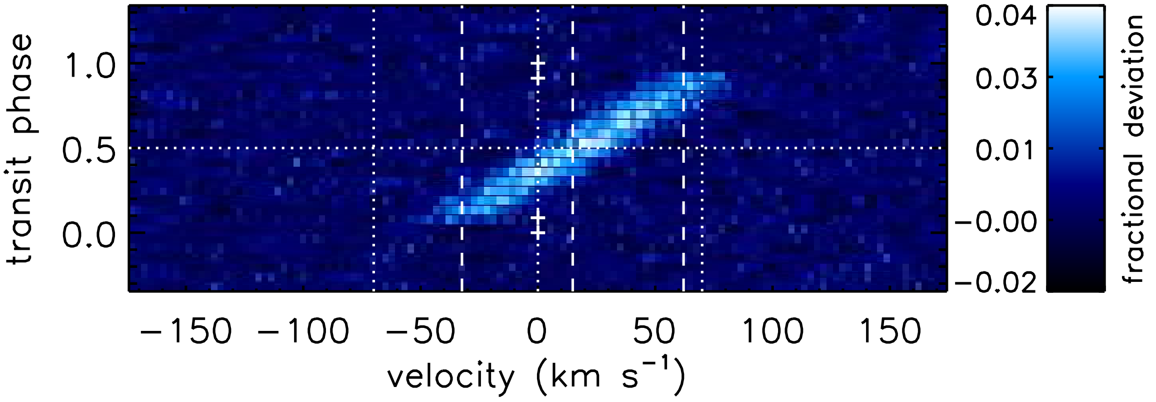

Figure 2.2 Model time series line profile residuals, illustrating v_{14} and $v_{\rm cen}$. The transit signature is the bright streak moving from lower center to upper right. The three vertical dashed lines mark, from left to right, v_1, $v_{\rm cen}$, and v_4, the velocity of the transit signature at ingress, mid-transit, and egress, respectively; $v_{14} = v_4 - v_1$. Time increases from bottom to top. The transit phase is defined such that ingress=0 and egress=1. Vertical dotted lines mark $v = 0, \pm v \sin i$, and a horizontal dotted line marks the time of mid-transit. Small crosses mark the times of first, second, third and fourth contacts. The units of the color scale are fractional deviation from the average out-of-transit line profile. Note that, in general ($b \neq 0$), $v_{\rm cen} \neq 0$ (unless $\lambda = 0$). I computed this model for a planet with $\lambda = 45°$ and $b = 0.3$ orbiting a star with $v \sin i = 70$ km s^{-1}, and added a small amount of noise to better approximate an actual observation.

signature will be below the noise floor. I define the velocity scale of the shifted line profile residuals such that it is $v_{\rm cen}$, the velocity of the transit signature at the transit midpoint. The definitions of v_{14} and $v_{\rm cen}$ with respect to the time series line profile residuals are shown graphically in Fig. 2.2.

For a grid of possible values of v_{14} ($|v_{14}| \leq 2v \sin i_\star$), I perform this shifting and binning operation, and visualize this as a two-dimensional map of the deviation from the out-of-transit line profile as a function of $v_{\rm cen}$ and v_{14}. In Fig. 2.3 I show the result of performing this operation on the model data from Fig. 2.2. This method is conceptually similar to that used by, e.g., Brogi et al. (2012, 2013), who directly detect spectral lines from hot Jupiters and, in their case, shift the time series data over the range of possible planetary radial velocity curves and bin to detect the signal.

While mathematically a complicated, usually double-valued relationship exists between (λ, b) and ($v_{\rm cen}$, v_{14}), qualitatively there exists a simple relationship between ($v_{\rm cen}$, v_{14}) and the path of the transit signature across the stellar disk. For solid-body rotation, and defining a coordinate x on the visible disk of the star perpendicular to the projected stellar rotation axis, each velocity on the line profile maps to a single value of x, i.e., $v \propto x$ (Gray 2005); equivalently, the isovelocity contours on the stellar surface are straight and parallel to the projected rotation axis. $v_{\rm cen}$ and v_{14} together fix the x coordinates of ingress and egress, x_1 and x_4, respectively. For each pair of x_1, x_4 there are two possible paths across the stellar disk: one with low λ, high b and one with high λ, low b, resulting in the double-valued function that maps (λ, b) to ($v_{\rm cen}$, v_{14}). This can be seen in Fig. 1.3, where both geometries share the same values of $v_{\rm cen}$ and v_{14}; the transit duration, information that is not taken into account by my shifting-and-binning method, can be used to distinguish these two solutions. In general I will always have some prior information on the transit duration, which can be used to determine which of the two solutions is appropriate for an individual case.

In general, positive values of v_{14} correspond to $|\lambda| < 90°$, and $v_{14} < 0$ corresponds to $|\lambda| > 90°$, while $v_{\rm cen} > 0$ corresponds to $\lambda > 0°$ and $v_{\rm cen} > 0$ corresponds to $\lambda < 0°$. The (dual-valued) relationship between the observables v_{14}, $v_{\rm cen}$ and my parameters of interest λ, b is:

$$\lambda = \sin^{-1}\left(\frac{2\sqrt{2}A}{\sqrt{4+4A^2-B^2 \pm \sqrt{(B^2-4A^2-4)^2-64A^2}}}\right) \tag{2.5}$$

and

$$b = \frac{A}{\sin\lambda} \tag{2.6}$$

defining $A = v_{\rm cen}/(v \sin i_\star)$ and $B = v_{14}/(v \sin i_\star)$ for brevity.

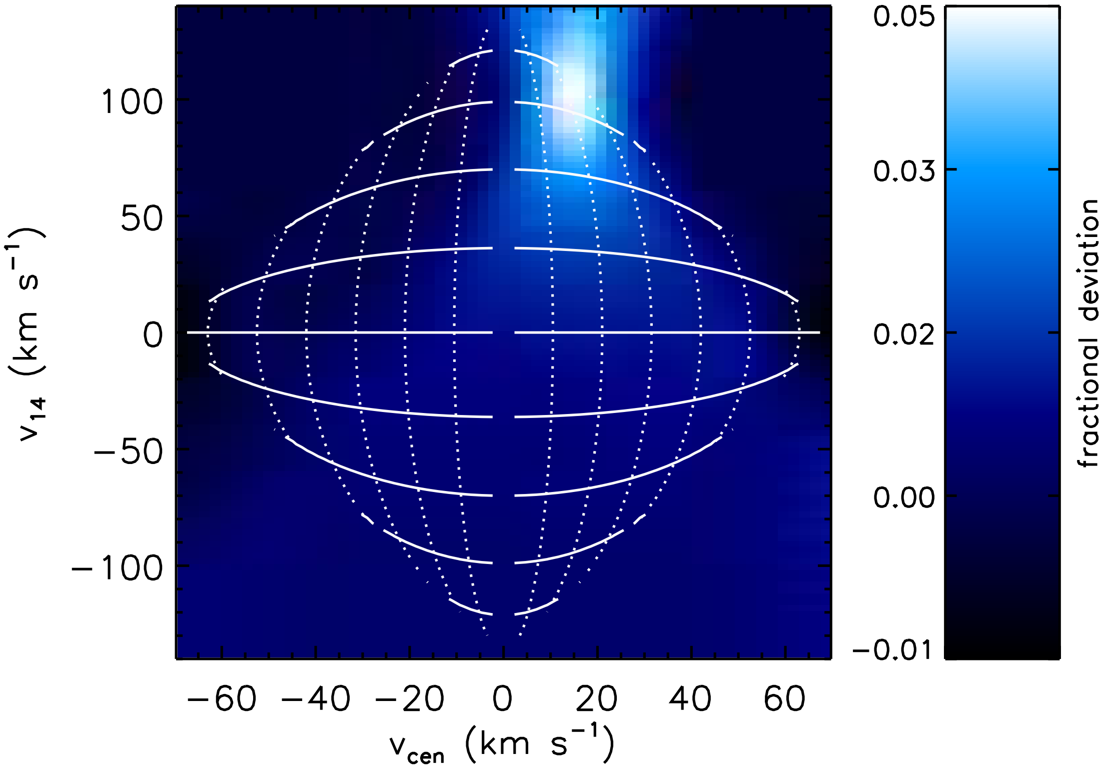

Figure 2.3 The model time series line profile residuals shown in Fig. 2.2, shifted and binned using the method described in the text. The bright spot near the top is the transit signature. The solid lines show lines of constant λ, while the dotted lines show lines of constant b. The λ contours mark, from top to bottom, $\lambda = \pm 30°, \pm 45°, \pm 60°, \pm 75°, \pm 90°, \pm 105°, \pm 120°, \pm 135°, \pm 150°$ (λ is positive on the right half of the plot, and negative on the left half). The b contours mark, from the centerline of the plot outwards, $b = 0.15, 0.30, 0.45, 0.60, 0.75, 0.9$. I note that the relationship between $(v_{\rm cen}, v_{14})$ and (λ, b) is double-valued; only one solution is shown here.

While it is possible to simply read off λ and b from the shifted and binned time series line profile residual map using Eqns. 2.5 and 2.6, in practice I can obtain more reliable values, and uncertainties thereon, by fitting a model to the shifted and binned data. I model these data by producing model time series line profile residuals in the same manner as described below in §2.3, and then shifting and binning this model in the same manner as I have treated the data.

2.3 Doppler Tomographic Modeling

Now that I have computed the time series line profiles and time series line profile residuals, I must extract the transit parameters from these data. I compute a model for the time series line profiles and/or time series line profile residuals and fit this to the data. I construct the model by numerically integrating over the stellar disk, summing the contributions from each surface element to the overall line profile. I divide the stellar disk into approximately 8,000 surface elements, utilizing Cartesian coordinates for the integration and subsequent computations. I assume a Gaussian intrinsic line profile for each surface element, which are then appropriately Doppler shifted, assuming solid body rotation, and scaled by a quadratic limb darkening law.

Rotational broadening is not the only type of line broadening present in stars; other varieties include thermal, microturbulent, and macroturbulent broadening. Thermal and microturbulent broadening both produce Gaussian line shapes, and so they are automatically included in the assumption above that the intrinsic line shape from each stellar surface element is Gaussian. Macroturbulence, however, does *not* produce a Gaussian line shape. It is typically described using a radial-tangential anisotropic macroturbulent proscription, which produces a peaked and distinctly non-Gaussian line profile (Gray 2005). Empirically, however, fitting the line profiles of two of my more slowly rotating target stars (HAT-P-41 and WASP-79, which both have $v \sin i_\star \sim 20\,\mathrm{km\,s^{-1}}$), I have found that neglecting the non-Gaussian line profile contribution of macroturbulence, and assuming that each surface element simply produces a Gaussian line profile that is the convolution of the thermal, microturbulent, and macroturbulent line profiles (insofar as it can be approximated as a Gaussian), produces a fit to the overall line profile that is within the uncertainties. I thus argue that I am justified in neglecting macroturbulence, and simply including all non-rotational contributions to line broadening in a single Gaussian "intrinsic line width" parameter. Macroturbulence could in principle also affect the measurement of λ and b by altering the stellar velocity fields on scales similar to the size of the planetary disk. I examine this possibility in more detail in the context of my observations of Kepler-13 Ab in §3.1.3.

In order to improve computational efficiency, I do not perform the full integration for each exposure. Instead, I first compute the out-of-transit line profile. Then, I compute the location of the planet at the beginning and the end of each exposure; I make the assumption that the acceleration of the planet in the plane of the sky is negligible during an exposure, i.e., that the transverse velocity of the planet is constant over the course of an exposure. In the case of an eccentric orbit, I additionally make the simplifying assumption that the angular velocity Ω of the planet in its orbit is constant, and equal to analytical value of this velocity at the midpoint of the transit; however, none of the planets analyzed in this dissertation has been shown to have an eccentric orbit, and so I do not actually make use of this assumption here. For each surface element near the planetary disk I then compute the fraction of the exposure for which that surface element is obscured by the planet. There are five cases that I define, for which I calculate t_c, the time for which the surface element is obscured during that exposure.

For the following equations, let the surface element in question have coordinates (x, y), defining a Cartesian grid on the plane of the sky, with the origin at the center of the stellar disk and with the positive y axis pointing along the projected stellar rotation axis, and let y' be the minimum distance from (x, y) to the transit chord. The units of x and y are in stellar radii $R_\star$. The angular velocity of the planet at transit center is $\Omega = 2\pi/P(1-e^2)^{-3/2}(1+e\sin\omega)^2$. I also define a cylindrical coordinate system with the z axis perpendicular to the planetary orbital plane; let θ_{mid} be the angular coordinate of the planet at the midpoint of the exposure, where $\theta_{\mathrm{mid}} = 0$ corresponds to mid-transit.

The five cases that I identify are as follows. Case 1 occurs if a surface element is obscured by the planet for the entire exposure. Trivially,

$$t_c = t_{\mathrm{exp}} \tag{2.7}$$

Case 2 occurs if a surface element is covered at either the start or the end of the exposure, by the half of the planetary disk closer to the location of the center of the planetary disk at the exposure midpoint. Let r_i be the distance from (x, y) to the center of the planetary disk at the start or the end of the exposure, depending upon when the surface element is obscured. In this case, the length of time that the surface element will be obscured is:

$$t_c = \left| \frac{\sqrt{(R_P/R_\star)^2 - y'^2} + \sqrt{r_i^2 - y'^2}}{\frac{(a/R_\star)\Omega(1-e^2)}{(1+e\cos\theta_{mid})^2}(-e\sin\omega + 2e\sin\omega\sin^2\theta_{mid} + \cos\omega\sin\theta_{mid} - \sin\omega\cos\theta_{mid})} \right| \tag{2.8}$$

Case 3 applies if a surface element is covered at either the start or the end of the exposure, by the half of the planetary disk farther from the location of the center of the planetary disk at the midpoint of the exposure. Then,

$$t_c = \left| \frac{\sqrt{(R_P/R_\star)^2 - y'^2} - \sqrt{r_i^2 - y'^2}}{\frac{(a/R_\star)\Omega(1-e^2)}{(1+e\cos\theta_{\rm mid})^2}(-e\sin\omega + 2e\sin\omega\sin^2\theta_{\rm mid} + \cos\omega\sin\theta_{\rm mid} - \sin\omega\cos\theta_{\rm mid})} \right| \tag{2.9}$$

Case 4 occurs if the surface element is covered for part of the exposure, but is covered at neither the start nor the end. Then,

$$t_c = \left| \frac{2\sqrt{(R_P/R_\star)^2 - y'^2}}{\frac{(a/R_\star)\Omega(1-e^2)}{(1+e\cos\theta_{\rm mid})^2}(-e\sin\omega - 2e\sin\omega\sin^2\theta_{\rm mid} - \cos\omega\sin\theta_{\rm mid} - \sin\omega\cos\theta_{\rm mid})} \right| \tag{2.10}$$

Finally, Case 5 is applicable if the surface element is not covered by the planet at any point during the exposure. Then, trivially,

$$t_c = 0 \tag{2.11}$$

Determining which case is applicable for each surface element is straightforward. I calculate the projected location of the center of the planetary disk at the beginning and the end of each exposure, and, for each surface element, calculate the distances d_1 and d_2 to these center locations. If $d_1 < R_P$ and $d_2 < R_P$, then the surface element is covered for the entire exposure and Case 1 applies. If $d_1 < R_P$ or $d_2 < R_P$, but not both, one of Case 2 or Case 3 will apply and I set $r_i = d_1$ or $r_i = d_2$, as appropriate. If $d_1 > R_P$ and $d_2 > R_P$ but the distance from the surface element to the transit chord is less than R_P and the closest approach of the planetary center to the surface element occurs during that exposure, then Case 4 applies. If none of these conditions apply, then the surface element will not be obscured during this exposure and Case 5 applies.

For each surface element, I diminish the out-of-transit line profile by the line profile contribution from that surface element, multiplied by the fraction of the exposure for which that surface element is covered by the planet (i.e., min($t_c/t_{\rm exp}$,1), where $t_{\rm exp}$ is the exposure time). Finally, I convolve each line profile with a model instrumental point spread function (PSF). For HET/HRS and HJST/TS23 I use a tophat profile for the PSF (W. D. Cochran, personal communication); otherwise, I assume a Gaussian with a width set by the instrumental resolution.

Now that I have computed the model time series line profiles, I need to fit them to the data in order to extract the parameters of interest. I use a Markov chain Monte Carlo (MCMC) to sample the likelihood function of the model fits to the data and produce posterior distributions for the included parameters. For the earlier work described here (the analysis of Kepler-13 described in §3.1), I used a custom-built MCMC routine. For the other systems analyzed in this dissertation I used an MCMC with affine-invariant ensemble samplers (Goodman & Weare 2010), as implemented in the Python package `emcee` (Foreman-Mackey et al. 2013).

Ideally, I would simply fit for all relevant parameters (λ, b, $v \sin i_\star$) simultaneously. As my time series line profiles are derived from the average of many lines across a wide region of the spectrum, and the limb darkening and therefore the detailed line shape change as a function of wavelength, my model line profiles do not always fit the average line profile to better than a few percent in the wings of the profile. This poses difficulties for extracting $v \sin i_\star$, as well as the transit parameters. In these cases I therefore adopted a two-stage fitting process, first extracting $v \sin i_\star$ from a single line (the Ba II line at λ6141.7 Å, which I chose because it is deep but unsaturated and unblended in my target stars), and then λ and b from the time series line profile residuals. In cases where I can adequately reproduce the observed line shape, I directly fit the time series line profiles, which gives λ, b, and $v \sin i_\star$ simultaneously.

In addition to the free parameters for each fit, I also wish to incorporate prior knowledge from the literature, e.g., the planetary orbital period and transit depth (which are typically poorly constrained by Doppler tomographic data alone), and uncertainties upon these parameters. I thus set Gaussian priors upon these parameters. For my own MCMC routine, assuming that the errors are Gaussian, I defined an "effective" χ^2 statistic

$$\chi^2_{\mathrm{eff}} = \sum_i \frac{(O_i - C_i)^2}{\sigma_i^2} + \sum_j \frac{(P_j - P_{j,0})^2}{\varsigma_j^2} \tag{2.12}$$

where O denotes the data, C the model, σ the calculated error on each data point, P_j the value of parameter j at the given iteration of the Markov chain, $P_{j,0}$ the value of parameter j from the literature, and ς_j the uncertainty on parameter j from the literature, and I am summing over i data points and j model parameters where I have prior information. For the `emcee` MCMC runs, where I sometimes simultaneously fit multiple datasets (e.g., Doppler tomographic data, transit photometry, and/or radial velocity data), I added the priors to the log probability:

$$\ln p = \sum_k \left(-\frac{1}{2} \sum_i \left(\frac{(O_{i,k} - C_{i,k})^2}{\sigma_{i,k}^2} + \ln \frac{1}{\sigma_{i,k}^2} \right) \right) - \frac{1}{2} \sum_j \frac{(P_j - P_{j,0})^2}{\varsigma_j^2} \tag{2.13}$$

where I am summing over i data points for each of k datasets (the total number of datapoints need not be the same for each dataset), and over j priors. Notation is the same as in Eqn. 2.12. The quantities χ^2 and $\ln p$ differ only by sign and constant factors; therefore, when using χ^2, I wish to minimize χ^2, and when using $\ln p$, I wish to maximize $\ln p$.

My detailed methodology for the MCMCs varies from system to system, depending upon its characteristics, the extent of prior knowledge on the system, and the availability of other datasets that I can fit simultaneously. These details are thus described in the later sections detailing my work on each system considered in this dissertation.

In all cases I use a quadratic limb darkening law to model the stellar surface brightness profile, and use the triangular sampling method of Kipping (2013) to obtain even sampling over the physically-allowed parameter space.

I note that in principle it is possible to measure $R_P/R_\star$ and $(R_P/R_\star)^2$ independently using Doppler tomography (the width of the transit signature depends on $R_P/R_\star$, while the area under the transit signature is proportional to $(R_P/R_\star)^2$). If a system is affected by dilution, the measured value of $(R_P/R_\star)^2$ will be smaller than that inferred from the measurement of $R_P/R_\star$ from the transit signature width, which is unaffected by dilution. In practice, however, given finite spectral resolution, limited time resolution, and relatively low signal-to-noise, these values are best determined from transit photometry. I therefore either incorporated these parameters in my MCMCs via priors, or through a simultaneous fit to transit photometry.

Chapter Three: Measuring Spin-Orbit Misalignments

3.1 Kepler-13 Ab[1]

The Kepler-13 (aka KOI-13, BD+46 2629) system has long been known to be a proper motion binary (Aitken 1904). Szabó et al. (2011) determined that it consists of two A-type stars with similar properties (see Table 3.1), which are separated by 1.12" (Adams et al. 2012). *Kepler* detected a planet candidate, KOI-13.01, in this system (Borucki et al. 2011); it was validated by Barnes et al. (2011), and it was subsequently given the name Kepler-13 Ab. Szabó et al. (2011) determined that it orbits the brighter of the two binary components, Kepler-13 A.

Santerne et al. (2012) detected a third stellar component in the system in an eccentric orbit about Kepler-13 B via the reflex motion of star B. They determined that this companion, Kepler-13 C (denoted Kepler-13 BB by Shporer et al. 2014), has a mass of $0.4M_\odot < M_\star < 1M_\odot$ and an orbital period of 65.8 days. Kepler-13 Ab thus orbits one member of a stellar triple system; alternatively, due to the massive nature of the planet Kepler-13 Ab (its mass is $\sim 8-10\,M_J$: Szabó et al. 2012; Mislis & Hodgkin 2012; Mazeh et al. 2012; Esteves et al. 2013; Placek et al. 2014), the system

---

[1] The work described in this section was originally published as Johnson, M. C., Cochran, W. D., Albrecht, S., Dodson-Robinson, S. E., Winn, J. N., & Gullikson, K., 2014, ApJ, 790, 30.
Author contributions: M.C.J. performed the Doppler tomographic analysis and modeling, reduced some of the HET data, and wrote the paper. W.D.C. initiated the project, and reduced the HJST and some of the HET data. S.A. assisted with the development of the Doppler tomographic analysis and modeling routines. W.D.C., S.A., S.E.D.-R., and J.N.W. assisted with discussion of methodology and results. K.G. searched for absorption lines due to the tertiary companion Kepler-13 C in the HET spectra; this portion of the original Johnson et al. (2014) paper is not included in this dissertation as this work was not principally performed by M.C.J.

could be considered to be a hierarchical quadruple.

Kepler-13 A is distinguished as one of the hottest stars to host a confirmed planet ($T_{\text{eff}} = 8500 \pm 400$ K). I list the stellar parameters for the three stars in the Kepler-13 system in Table 3.1, and summarize planetary and transit parameters from the literature in Table 3.2. As Kepler-13 Ab is a hot Jupiter, it is one of the hottest known planets; Mazeh et al. (2012) estimated $T_{\text{eff}} = 2600 \pm 150$ K using the secondary eclipse depth in the *Kepler* passband.

Kepler-13 Ab was first validated by Barnes et al. (2011) through detection of a gravity-darkening signature in the transit lightcurve from *Kepler*. This also enabled them to measure the spin-orbit misalignment, albeit with degeneracies, to be $\lambda = \pm 23^\circ \pm 4^\circ$ or $\lambda = \pm 157^\circ \pm 4^\circ$. Shporer et al. (2011), Mazeh et al. (2012), Mislis & Hodgkin (2012), Esteves et al. (2013), and Placek et al. (2014) detected Doppler beaming and ellipsoidal variations due to the planetary orbit, and used these to measure the mass of Kepler-13 Ab to be $\sim 8 - 10 M_J$, putting it firmly below the deuterium burning limit. Many of these different authors, however, found conflicting values for some of the transit and system parameters, especially the impact parameter b, ranging from 0.25 to 0.75 (Table 3.2). While the orbital plane of Kepler-13 Ab has been shown to be precessing, resulting in changes in the transit duration and impact parameter (Szabó et al. 2012, 2014; Masuda 2015), the rate of change of the impact parameter found by Szabó et al. (2012), $db/dt = -0.016 \pm 0.004$ yr^{-1}, is much too small to account for these discrepancies. While Szabó et al. (2011) found no evidence for orbital eccentricity, Shporer et al. (2014) measured a secondary eclipse time offset by ~ 30 seconds from that expected assuming a circular orbit. This could be caused by either a very small eccentricity ($e \sim 5 \times 10^{-4}$), or a bright spot on the planetary surface offset to the west of the substellar point. Due to the uncertainty in whether

Table 3.1. Parameters of Kepler-13 A, B, and C from the Literature

Parameter	Santerne et al. (2012)	Szabó et al. (2011)
	System Parameters	
d (pc)	…	500
age (Gyr)	…	$0.708^{+0.183}_{-0.146}$
A_V (mag)	…	0.34
	Kepler-13 A	
V (mag)	…	9.9
$T_{\rm eff}$ (K)	…	8511^{+401}_{-383}
$\log g$ (cgs)	…	3.9 ± 0.1
[Fe/H]	…	0.2
$v \sin i_\star$ (km s^{-1})	76.6 ± 0.2	65 ± 10
$M_\star (M_\odot)$	…	2.05
$R_\star (R_\odot)$	…	2.55
	Kepler-13 B	
V (mag)	…	10.2
$T_{\rm eff}$ (K)	…	8222^{+388}_{-370}
$\log g$ (cgs)	…	4.0 ± 0.1
[Fe/H]	…	0.2
$v \sin i_\star$ (km s^{-1})	62.7 ± 0.2	70 ± 10
$M_\star (M_\odot)$	…	1.95
$R_\star (R_\odot)$	…	2.38
	Kepler-13 C	
P (days)	65.831 ± 0.029	…
e	0.52 ± 0.02	…
K (km s^{-1})	12.42 ± 0.42	…
$M_\star (M_\odot)$	$> 0.4, < 1$	…

Note. — K is the radial velocity semi-amplitude of Kepler-13 B due to its mutual orbit about Kepler-13 C.

Table 3.2. Parameters of Kepler-13 Ab from the Literature

Parameter	Placek et al.	Müller et al.	Esteves et al.	Mazeh et al.	Mislis & Hodgkin	Szabó et al.	Shporer et al.	Barnes et al.	Szabó et al.
	(2014)	(2013)	(2013)	(2012)	(2012)	(2012)	(2011)	(2011)	(2011)
P (days)	1.76367	1.763586522	1.7635877	...	...	...	1.7637	...	...
...	±0.00007	$^{+0.000000194}_{-0.000000160}$	±0.000001	...	...	...	±0.0013	...	...
$R_P/R_\star$	...	0.08553	0.080509	0.0907	...	...	...	0.084513	0.0884
...	...	±0.000007	$^{+0.000033}_{-0.000048}$	±0.0005	...	...	...	...	±0.0027
$a/R_\star$	...	4.434	4.3396	3.17	...	...	...	...	
...	...	$^{+0.011}_{-0.010}$	$^{+0.0102}_{-0.0075}$	±0.06	...	...	...	...	
$i_P(^\circ)$	81.37	85.82	85.135	...	...	...	...	85.9	...
...	±5.23	$^{+0.10}_{-0.12}$	$^{+0.097}_{-0.063}$	...	...	...	...	±0.4	...
b	...	0.323	0.3681	0.75	...	0.253	...	0.31598	0.75
...	...	$^{+0.008}_{-0.007}$	$^{+0.0041}_{-0.0064}$	±0.01	...	±0.020	...	...	...
λ (°)	...	...	...	...	...	...	...	±23 or ±157	...
...	...	...	...	...	...	...	...	±4	...
$i_\star$ (°)	...	...	...	...	...	...	...	−48	...
...	...	...	...	...	...	...	...	±4	...
ψ (°)	...	...	...	...	...	...	...	56	...
...	...	...	...	...	...	...	...	±4	...
R_p (R_J)	> 0.748	...	2.042	...	...	...	...	1.445	2.2
...	±0.015	...	±0.080	...	...	...	...	±0.016	±0.1
M_p (M_J)	8.35	...	7.95	10	8.3	9.2	...	...	...
...	±0.43	...	±0.27	±2	±1.25	±1.1	...	...	...
$P_{\mathrm{rot},\star}$ (hr)	...	...	...	...	...	25.43	...	22.0	...
...	...	...	...	...	...	±0.05	...	...	...
$f_\star$	...	...	...	...	...	...	...	0.021	...

Note. — Values from Barnes et al. (2011) assume a value of $M_\star = 2.05 M_\odot$, from Szabó et al. (2011). $i_\star$ is the stellar obliquity (denoted as ψ by Barnes et al. 2011), ψ is the full three-dimensional spin-orbit misalignment (denoted as φ by Barnes et al. 2011), i_P is the inclination of the planetary orbit with respect to the plane of the sky (typically denoted i, but I adopt the notation i_P to distinguish it from the stellar obliquity $i_\star$, which is also typically denoted i), and $f_\star = (R_{\mathrm{eq}} - R_{\mathrm{pole}})/R_{\mathrm{eq}}$ is the stellar dynamical oblateness (Barnes 2009), where R_{eq} and R_{pole} are the stellar equatorial and polar radii, respectively.

the orbit is indeed eccentric, and the very small allowed eccentricity even if it is non-zero, I will assume that the orbit is circular.

Kepler-13 A is rapidly rotating ($v \sin i_{\star} = 76.6$ km s^{-1}; Santerne et al. 2012) and bright for a *Kepler* target ($Kp = 9.96$), making it an excellent target for Doppler tomography. While there is a previous measurement of λ via gravity darkening (Barnes et al. 2011), this method cannot distinguish between prograde and retrograde orbits, hence the four-fold degeneracy in their measurement of λ quoted above. I can break this degeneracy with Doppler tomography. With this work Kepler-13 Ab becomes the first planet with measurements of λ from both gravity darkening and Doppler tomography, an important consistency check. Additionally, Albrecht et al. (2012b) showed that, in addition to the stellar $T_{\rm eff}$, the planetary scaled semi-major axis $a/R_{\star}$ and mass ratio $M_P/M_{\star}$ are correlated with the degree of (mis)alignment. A measurement of the spin-orbit misalignment for Kepler-13 Ab helps to expand the parameter space, as it is a particularly massive planet orbiting close to a massive star.

3.1.1 Methodology for Kepler-13

The Kepler-13 A/BC mutual separation of 1.12" (Adams et al. 2012) is smaller than the 2" diameter of the HET/HRS optical fibers, and so my HET data on this system contain light from both stars and consequently the spectra contain two superposed line profiles. Furthermore, since Kepler-13 B is itself a single-lined spectroscopic binary, its line profile moves with respect to that of Kepler-13 A. In order to obtain reliable results I had to account for these complications in both the data reduction and analysis, and in this section I describe the consequent modifications to the overall methodology described in Chapter 2.

The TS23 observations used an $1.2 \times 8.2''$ slit[2] with no field rotator, and so the relative contributions to the spectrum from Kepler-13 A and B vary throughout the course of an observation. While this can, in principle, be corrected for, guiding errors will also cause similar but unpredictable variations. I therefore did not attempt such a correction.

During the line profile extraction process, as I was obtaining the nightly velocity offset for the data, fitting a single line profile resulted in a bias in the velocity offsets of the spectra that was correlated with the orbital phase of Kepler-13 B about C. In order to correct for this, I instead fit a model spectrum produced using two analytic rotationally broadened line profiles, with a time-dependent velocity separation given by the orbital elements found by Santerne et al. (2012). I determined the contrast between the two profiles by fitting two model line profiles to final extracted line profiles using the unmodified methodology.

I also had to modify my analysis process as I was extracting the transit parameters of Kepler-13 Ab, by including Kepler-13 B's moving line profile in my model. I used the orbital elements for Kepler-13 B's orbit about its barycenter with Kepler-13 C presented by Santerne et al. (2012) to calculate the velocity of Kepler-13 B at each exposure. I then computed a rotationally broadened line profile for Kepler-13 B using my line profile modeling code, Doppler shifted it and scaled it relative to the Kepler-13 A profile, and added it to the line profile for Kepler-13 A. Including this profile and the resulting dilution of the spectroscopic transit signature was necessary to accurately model the data.

I obtained the best-fit parameters for my data on the Kepler-13 system using two sequential MCMCs, both using a custom MCMC routine. In both cases I used four

---

[2] http://nexus.as.utexas.edu:8081/obs_sup/man/manuals/2dcoude/slitinfo.html

chains each of 150,000 steps, cutting off the first 20,000 steps of burn-in. My model line profiles did not fit the average line profile to better than a few percent in the wings of the profile, and so I used a two-stage fitting process, first extracting $v \sin i_\star$ from a single line and then λ and b from the time series line profile residuals.

First, I modeled a single line, the Ba II line at λ6141.7 Å, chosen because it is deep but unsaturated and isolated. I fit the nightly master spectra with models of the line profiles of Kepler-13 A and B, neglecting any contribution from the transiting planet. I left the $v \sin i_\star$ of each star, the contrast between the two stars, and eight nightly velocity offsets as free parameters. I set Gaussian priors upon two quadratic limb darkening parameters for each star, each with a width 0.1, and upon the five parameters determining the radial velocity variation of Kepler-13 B (P, epoch T_0, e, ω, K). For the limb darkening coefficients I used coefficients in the Sloan r band (as this is the closest standard photometric band to the Ba II λ6141.7 Å line), taken from the tables of Claret (2004) for an ATLAS model atmosphere and interpolated to the stellar parameters of Kepler-13 A and B as presented by Szabó et al. (2011) using the JKTLD code[3]. For the orbital parameters, I set the initial value and prior width to the best-fit value and 1σ uncertainty, respectively, presented by Santerne et al. (2012); see Table 3.1.

Second, I fit the time series line profile residuals with an appropriate model using another MCMC. Here I left λ and b as free parameters, and set priors on the $v \sin i_\star$ of Kepler-13 A and contrast between Kepler-13 A and B (with the prior value and width set to the median values and 1σ uncertainty, respectively, on these parameters from the first MCMC), and the limb darkening coefficients of Kepler-13 A, radius ratio $R_p/R_\star$, transit duration, planetary orbital period, and planetary transit epoch, with

---

[3] http://www.astro.keele.ac.uk/jkt/codes/jktld.html

all values and uncertainties/prior widths taken from Esteves et al. (2013). I fixed the $v \sin i_\star$ and orbital parameters of Kepler-13 B at values from the first MCMC and Santerne et al. (2012), respectively, in the interests of computational efficiency and as uncertainties in these parameters should have a minimal effect on the line profile residuals.

3.1.2 Results for Kepler-13

Using my first MCMC, I measured projected rotational velocities for the two stars of $v \sin i_A = 76.96 \pm 0.61$ km s^{-1} and $v \sin i_B = 63.21 \pm 1.00$ km s^{-1}, which agree to within 1σ with the $v \sin i_\star$ values presented by Santerne et al. (2012) (Table 3.1).

In the top panel of Fig. 3.1 I show the time series line profile residuals extracted from the HET data, produced by subtracting the out-of-transit template line profile from each of the time series line profiles. Significant systematics are visible, of amplitude ~ 0.1 of the depth of the line profile. Most of these systematics result from differences between the time series line profiles and the out-of-transit template line profile due to the motion of Kepler-13 B in velocity space. This is illustrated in the middle panel of Fig. 3.1, where I have subtracted the average line profile *from each night* from each of the time series line profiles. The bottom panel of Fig. 3.1 is identical to the middle panel, except using all of my HET data. Due to these systematics, for the remainder of the analysis I subtract the nightly average line profile from the time series line profiles, and I do not use the out-of-transit template data any further. The RMS scatter of the continuum is 0.022 times the line depth. The transit signature is immediately apparent visually. That the planetary orbit is prograde can be determined by inspection, as the transit signature is over the blueshifted hemisphere of the star at ingress and moves across to the redshifted hemisphere by egress. In

Fig. 3.2 I show the residuals after subtraction of the best-fit transit model. I also shift and bin the HET data (see Fig. 3.3, top). Again, the transit signature is clearly detected.

My best-fit values and 1σ uncertainties from the MCMCs are shown in Table 3.3. I present values from both directly fitting the data and fitting the shifted and binned data; these two methods give consistent results. The binned data have smaller uncertainties, but in order to be conservative and as the direct fits have a reduced chi-squared closer to 1 ($\chi^2_{\rm red} = 1.13$ for the direct fit, $\chi^2_{\rm red} = 0.66$ for the shifted and binned fit), I quote the values from the direct fit. I found a best-fit spin-orbit misalignment of $\lambda = 58.6° \pm 1.0°$, in strong disagreement with the value of $\lambda = 23° \pm 4°$ found by Barnes et al. (2011). I also found $b = 0.256 \pm 0.011$. I note that the quoted uncertainties on these parameters are the formal statistical uncertainties, given the assumptions made in my models. They do not include systematic uncertainties, which I discuss in detail in §3.1.3.

I note that my data also permit a second solution, with $\lambda = 16.04° \pm 0.72°$ and $b = 0.856 \pm 0.014$. This solution, however, has a slightly worse value of reduced chi-squared ($\chi^2_{\rm red} = 1.03$), and moreover implies a physically unrealistically low value for the stellar mean density, $\bar{\rho}_\star = 0.04$ g cm^{-3}. I calculated the stellar mean density using Eqn. 9 of Seager & Mallén-Ornelas (2003), which is, using the nomenclature used in this dissertation and assuming a circular orbit,

$$\bar{\rho}_\star = \left(\frac{4\pi^2}{P^2 G}\right)\left(\frac{(1 + R_P/R_\star)^2 - b^2[1 - \sin^2(\tau_{14}\pi/P)]}{\sin^2(\tau_{14}\pi/P)}\right)^{3/2} \tag{3.1}$$

where P is the planetary orbital period and τ_{14} is the transit duration, both measured from *Kepler* photometry. Note that the inferred stellar mean density depends only upon my measurement of b and does not directly depend upon λ. Given this stellar mean density and the stellar surface gravity measured by Szabó et al. (2011)—$\log g =$

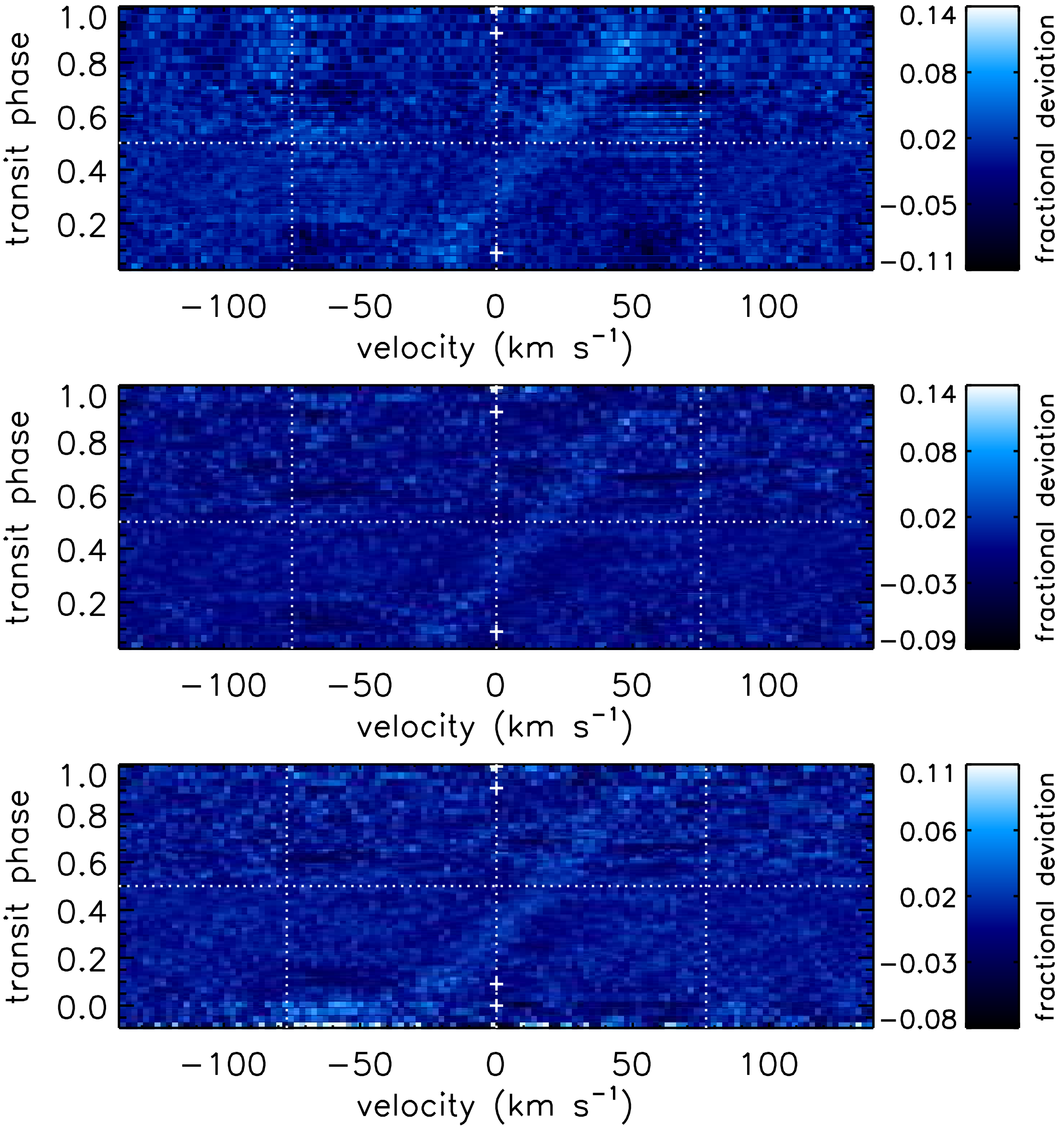

Figure 3.1 Top: transit signature of Kepler-13 Ab, using the best quality HET data (all transits except those of 2011 Nov 5 and 2012 Jun 7, which were excluded due to lower signal-to-noise; see Table 2.2). The transit signature is the bright streak moving from lower left to upper right. Note the large ($\sim$ 0.1 of the depth of the line profile) systematics. Middle: same as top, except subtracting off the average line profile from each night. Note that most of the systematics have vanished, but the amplitude of the transit signature has also been reduced. Bottom: same as middle, but using all of my data. For display purposes points with fractional deviations from the out of transit line profile greater than 0.11 or less than -0.08 have been set to these values, in order to better display the transit signature. This only affects the earliest spectrum.

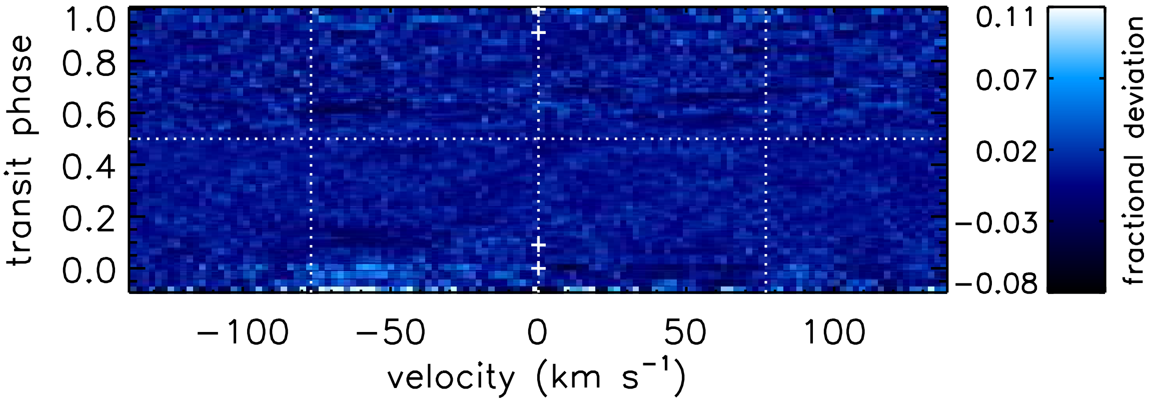

Figure 3.2 Same as the bottom panel of Fig. 3.1, but with the best-fitting transit model subtracted. The transit signature is well subtracted. For display purposes points with fractional deviations from the out of transit line profile greater than 0.11 or less than -0.08 have been set to these values, in order to better display the (lack of the) transit signature. This only affects the earliest spectrum.

3.9 ± 0.1—I have two independently-measured parameters which physically depend only upon the stellar mass and radius; thus, I can estimate the stellar mass and radius implied by $\bar{\rho}_\star$ and see whether it is compatible with the other system parameters. A value of $\bar{\rho}_\star = 0.04$ g cm^{-3} implies a stellar radius of $R_\star = 8 - 13\,R_\odot$ and mass of $M_\star = 15 - 60\,M_\odot$, values which are incompatible with the Szabó et al. (2011) value of $T_{\rm eff} = 8511^{+401}_{-383}$ K, as well as the other measured parameters of the system. Performing the same exercise for $b = 0.256$ results in a stellar mass and radius consistent with those found by Szabó et al. (2011) and Barnes et al. (2011). I thus conclude that the low-b, high-λ solution is the correct one. The full χ^2 space for my data is shown in Fig. 3.4.

My dataset also includes two transits of Kepler-13 Ab observed with the HJST. I show these data in Fig. 3.5. Like for the HET, in order to produce the time series line profile residuals, I subtract off the average line profile from each night rather than an out-of-transit line profile from both nights. These data have a much lower signal-

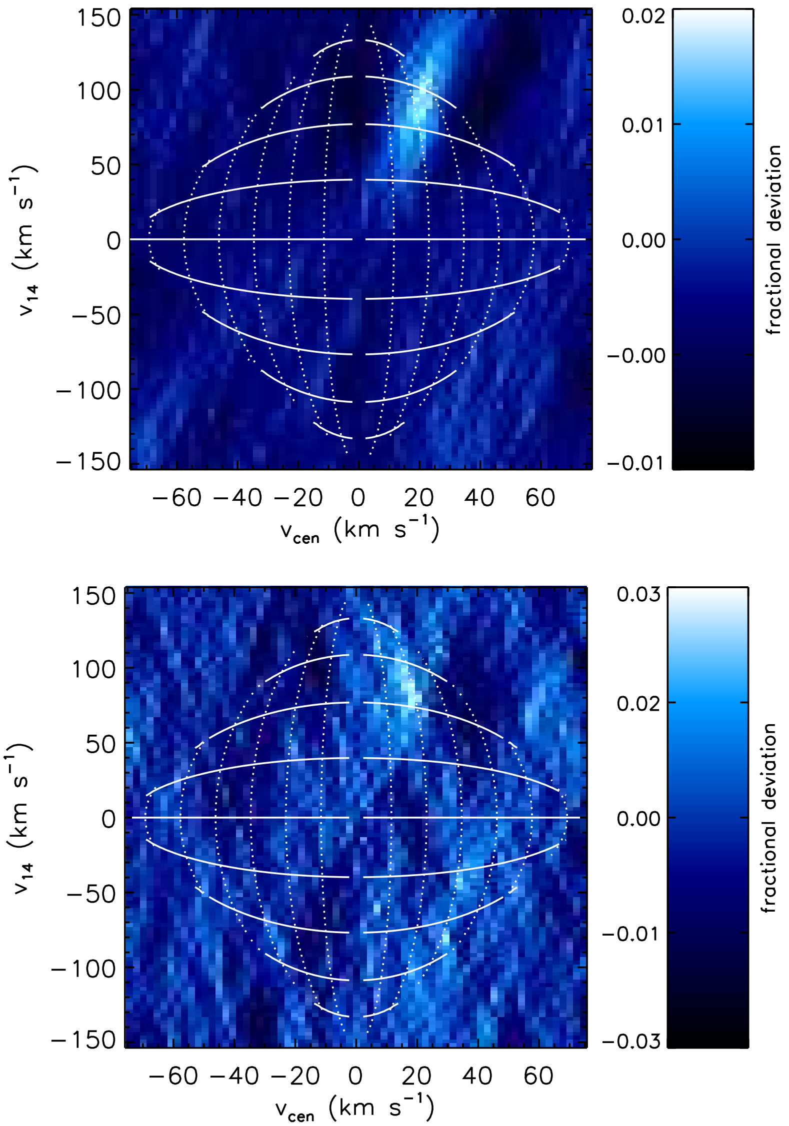

Figure 3.3 Top: shifted and binned transit data from the HET. Bottom: same as top, but for the HJST data. A bright spot is visible in the same location as in the HET data, indicating a low signal-to-noise detection of the transit. The dark side-lobes on either side of the bright transit signature (especially prominent in the HET data) are, in part, the result of subtracting off the average line profile from each night, rather than an out-of-transit line profile. The solid lines show lines of constant λ, while the dotted show lines of constant b. The λ contours mark, from top to bottom, $\lambda = \pm30°, \pm45°, \pm60°, \pm75°, \pm90°, \pm105°, \pm120°, \pm135°, \pm150°$ (λ is positive on the right half of the plot, and negative on the left half). The b contours mark, from the centerline of the plot outwards, $b = 0.15, 0.30, 0.45, 0.60, 0.75, 0.9$. I note that the relationship between $(v_{\rm cen}, v_{14})$ and (λ, b) is double-valued; only the solution appropriate to Kepler-13 Ab is shown here.

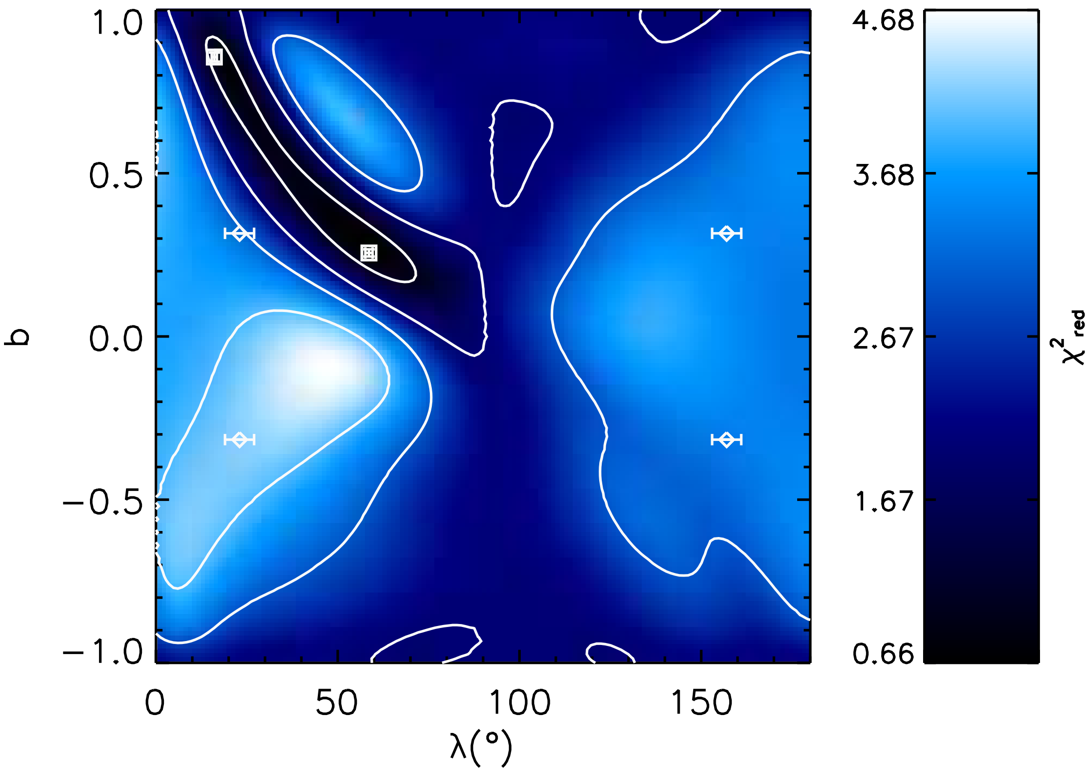

Figure 3.4 Reduced χ^2 space for my shifted and binned HET data, in λ and b. The four solutions allowed by Barnes et al. (2011) and their associated uncertainties are marked by diamonds; Barnes et al. (2011) did not quote an uncertainty on their value of b. The two best-fit solutions allowed by my data are denoted by squares. For this display I allow negative values of b; note that a transit chord with $(+\lambda, -b)$ is indistinguishable from one with $(-\lambda, +b)$. The contours denote $\chi^2_{\rm red} = 1, 2, 3, 4$.

to-noise level than the HET data (the RMS scatter of the normalized continuum is 0.037 times the line depth), and the transit is not readily apparent to the eye in the time series line profile residual map. I applied the bin-and-shift method to the HJST data (see the bottom panel of Fig. 3.3). Here, I recovered the same transit signature seen in the HET data, albeit at lower signal-to-noise. Here I measured values of $\lambda = 60.5° \pm 1.1°$ and $b = 0.168 \pm 0.010$. The spin-orbit misalignment is in mild disagreement with the value from the direct fit to the HET data, at a level of 1.3σ for

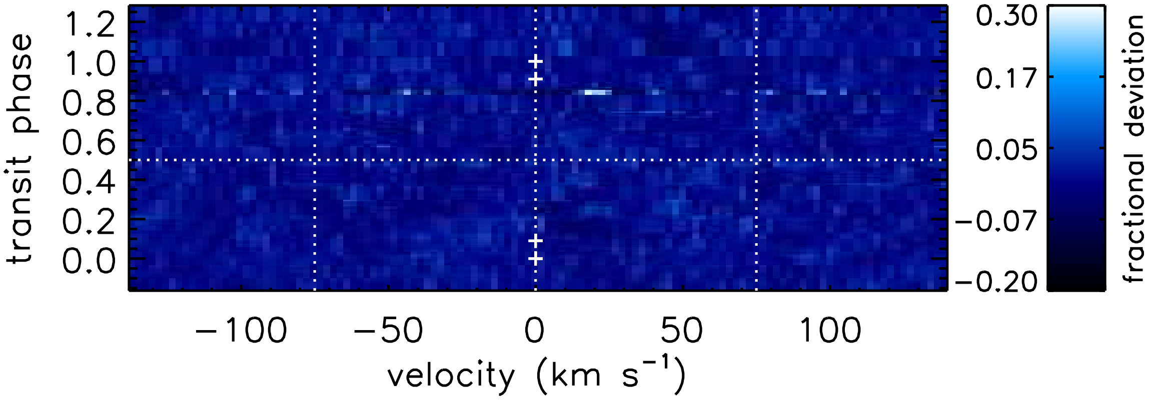

Figure 3.5 Time series line profile residuals for Kepler-13 Ab from the HJST, using data from both observed transits. The transit signature is not apparent to the eye.

λ, while there is a strong 6σ disagreement between the impact parameter found from the HET and HJST data. One possible cause is the varying degree of contamination from Kepler-13 B during the observations due to field rotation (as noted above, TS23 is a slit spectrograph). Another possible cause is the poorer time resolution of the HJST data as compared to the HET (exposure times were 900 s for the HJST and 300 s for the HET). In the spectroscopic data the impact parameter is constrained, in part, by how quickly the transit signature appears (disappears) between first and second (third and fourth) contacts. Thus, the lower time resolution of the HJST could introduce larger systematic uncertainties in these data. Additionally, the values above include only statistical uncertainties, which overstate the true degree of discrepancy between the HET and HJST values. I have, however, been unable to positively identify the source of this discrepancy.

Table 3.3. Results for Kepler-13

Parameter	Adopted	HET direct fit	HET binned fit	HJST binned fit
$v \sin i_A$ (km s^{-1})	...	76.96 ± 0.61	...	...
$v \sin i_B$ (km s^{-1})	...	63.21 ± 1.00	...	...
λ (°)	58.6 ± 2.0	58.6 ± 1.0	58.24 ± 0.68	60.5 ± 1.1
b	0.256 ± 0.030	0.256 ± 0.011	0.266 ± 0.007	0.168 ± 0.010

Note. — The quoted uncertainties for all except the "adopted" column are the formal statistical uncertainties and do not take systematic uncertainties into account.

3.1.3 Quantifying the Effects of Neglecting Differential Rotation and Macroturbulence

The formal uncertainties on my values for λ and b quoted earlier are the statistical uncertainties given the assumptions that I have made in my models (no differential rotation or macroturbulence, etc.) and do not contain information on systematic sources of uncertainty, which I will now discuss.

One possible source of systematic errors is the presence of differential rotation, which I have neglected in my models. Ammler-von Eiff & Reiners (2012) analyzed the line profiles of A and F dwarfs for evidence of differential rotation. They found no stars with $T_{\text{eff}} > 8500$ K that exhibited differential rotation. Balona (2013), however, used Fourier analysis of the *Kepler* lightcurves of A stars to infer that these stars exhibit a similar degree of differential rotation to the Sun. I constructed a modified version of my models that includes differential rotation, and conducted a version of my first MCMC, fitting to the line profile shape, in order to constrain the differential rotation. For a differential rotation law $\omega = \omega_0 - \omega_1 \sin^2 \phi$, where ϕ is the latitude on the stellar surface, the differential rotation parameter α can be defined as $\alpha = \omega_1/\omega_0$

(for the Sun, $\alpha = 0.20$; Reiners & Schmitt 2002). I note that I also needed to include the stellar inclination $i_\star$ with respect to the line of sight in this model; however, I found $i_\star$ to be totally unconstrained. The results of this exercise indicated the presence of a small amount of differential rotation. Overall, I found $\alpha = 0.050 \pm 0.028$; however, there does exist a degeneracy such that higher values of $|i_\star|$ result in larger preferred values for α: I found $\alpha = 0.034 \pm 0.017$ for $i_\star = 0^\circ$ and $\alpha = 0.046 \pm 0.023$ for $|i_\star| = 48^\circ$, the value found by Barnes et al. (2011). This is consistent with the results of Szabó et al. (2014), who found splitting of the frequency spectrum peak associated with Kepler-13 A's rotation, likely due to differential rotation.

In order to test the effects of this level of differential rotation on my measurement of the transit parameters, I modified my second MCMC to include differential rotation. I added two parameters, α and the stellar inclination $i_\star$. $i_\star$ was allowed to float, while, due to the dependence of the best-fit α on $i_\star$, I included a variable prior on α depending on the value of $i_\star$. Marginalizing over $i_\star$ in the results from the first MCMC in 5° bin sizes, I found the mean and standard deviation of α for each bin and used these as the prior center and width for the new MCMC. From this MCMC, I obtained $\lambda = 56.56^\circ \pm 0.85^\circ$ and $b = 0.2870 \pm 0.0095$. I note that the presence of even strong differential rotation cannot bring my value of λ into agreement with that found by Barnes et al. (2011).

I also neglected macroturbulence in my models, which could potentially induce systematic uncertainties in my measured values of λ and b. Measurements of macroturbulence in A dwarfs in the literature are somewhat lacking. Simón-Díaz & Herrero (2014) found varying degrees of macroturbulent broadening for B dwarfs, ranging from none to several tens of km s^{-1} (they noted that this "macroturbulence" is not necessarily physical turbulence). Fossati et al. (2011) measured macroturbulent broadening of order ~ 10 km s^{-1} for two late A dwarfs. Aerts et al. (2009) argued that "macroturbulence" in early-type stars is actually due to the collective action of many low-amplitude pulsational modes; early-type stars which do not pulsate should not show this type of macroturbulence. Even with *Kepler*'s photometric precision, there is little evidence for any pulsation of Kepler-13 A which could result in this type of "macroturbulence." Cantiello et al. (2009) conducted simulations of convection in the outer layers of massive stars due to an opacity peak produced by Fe ionization. They found that such zones can cause surface granulation and consequent small-scale velocity fields in stellar photospheres. They found, however, that this effect does not occur for stars with $L_\star < 10^{3.2}\, L_\odot$ at Galactic metallicities, and is furthermore more prominent at low surface gravities. As Kepler-13 A is below this luminosity cutoff ($L_\star = 10^{1.5}\, L_\odot$) and has high surface gravity ($\log g = 3.9 \pm 0.1$; Szabó et al. 2011), I conclude that surface granulation due to this mechanism should not occur for Kepler-13 A.

A key question for estimating the effects of macroturbulence upon my results lies with the scales of macroturbulent velocity fields in the stellar atmosphere. If these scales are much smaller than the size of the planetary disk, then this will simply increase the range of radial velocities over which the planet subtracts light from the line profile. The effect will be to "smear out" the transit signature, but this should not affect the measured value of λ. If, however, the macroturbulent velocity field changes on scales of similar or greater size as the planetary disk, then the velocity of the region of the stellar disk covered by the planet will differ from that expected if taking only rotation into account. Thus, the planetary transit signal in each spectrum will exhibit a quasi-random shift from the expected velocity.

Kallinger & Matthews (2010) presented evidence that some of the large number of frequencies seen in the frequency spectra of δ Sct (early A) stars observed by CoRoT are in fact due to surface granulation rather than pulsations, as pulsations at these frequencies would be of such high degree l that they should not be evident in disk integrated photometry. Based upon the inferred granulation frequencies, they found that the granulation properties follow scaling laws derived for solar-type stars. When scaling from such solar models, Stello et al. (2007) made the assumption that the size of granulation cells is proportional to the atmospheric pressure scale height H_P. Kjeldsen & Bedding (1995) used the scaling relation $H_P \propto T_{\rm eff}/g$. Using these relations and the stellar properties of Kepler-13 A from Szabó et al. (2011), I estimated that the size of any surface granulation cells for Kepler-13 A should be ~ 5 times that of such cells on the Sun, or $\sim 0.1 R_J$, comfortably below the size scale of the planetary disk (using an average solar granule size of 1300 km, from Gray 2005). Nonetheless, given the uncertainty in the relations used to derive this estimate, I chose to include "jitter" caused by large-scale macroturbulent cells in the stellar atmosphere in my MCMC (note that this is not the same as the jitter frequently invoked as a source of noise in radial velocity observations).

In order to simulate the effect of macroturbulence on the size scale of the planet, I used the following approach. I allowed each of the time series line profile residuals to have a small velocity offset from its nominal value. The effect of this is to shift the transit signature in that line profile residual in velocity space. Since I have already subtracted off the average line profile shape, this mimics a velocity shift of the transit signature due to large-scale macroturbulence rather than a radial velocity offset for the entire line profile. For computational reasons I applied this velocity shift to the model line profile residuals, not the data. At each MCMC step, I performed a single parameter minimization for each velocity offset using `mpfit`. Similar methodologies have been used by Albrecht et al. (2013) to deal with jitter and by Albrecht et al. (2014) to handle stellar pulsations. I limited the velocity offset amplitude to 15 km s^{-1} in order to prevent the model transit signatures from latching on to the remaining systematics in the data. I found a mean offset amplitude of 5.7 km s^{-1}. From these MCMCs, I obtained $\lambda = 60.4^\circ \pm 1.6^\circ$ and $b = 0.230 \pm 0.030$.

I thus found that including "jitter" and differential rotation have opposite systematic effects on my results: large-scale macroturbulence shifts the best-fit parameters to higher λ and lower b, while differential rotation shifts them to lower λ and higher b. Thus, I expect that these effects should largely cancel each other out, and my overall results should not be affected, while increasing the uncertainty in these results. In order to remain 1σ consistent with both the differential rotation and "jitter" MCMC results, I therefore adopt $\lambda = 58.6^\circ \pm 2.0$ and $b = 0.256 \pm 0.030$.

Additionally, for Kepler-13 A I assumed an intrinsic line width (standard deviation of a Gaussian) of 5 km s^{-1}. In order to test the impact of this assumption on my results I fit a model with an intrinsic line width of 10 km s^{-1} to my data. This did not significantly alter my measured values of λ and b or the $\chi^2_{\rm red}$ value of the model fits, and so I conclude that this has minimal impact on my measurements.

3.1.4 Conclusions on Kepler-13

My best-fit value for the spin-orbit misalignment for Kepler-13 Ab, $\lambda = 58.6^\circ \pm 2.0^\circ$, is in stark disagreement with the value of $\lambda = 23^\circ \pm 4^\circ$ found by Barnes et al. (2011). Even if I fixed b to the value found by Barnes et al. (2011), I obtained a spin-orbit misalignment of $\lambda \sim 54^\circ$, still in disagreement with the gravity darkening value. I do not have a definitive explanation for the mismatch between my result and that from Barnes et al. (2011). I note, however, that my value relies upon fewer assumptions regarding the physical nature of the star (e.g., the gravity-darkening law and gravity-darkening parameter), and thus is likely more robust. Additionally, Barnes et al. (2011) fixed the effective temperature of the pole of Kepler-13 A to 8848 K, the temperature from the Kepler Input Catalog (KIC), rather than a more accurate spectroscopic value ($T_{\rm eff} = 8511^{+401}_{-383}$, from Szabó et al. 2011, though these values for the temperature differ by less than 1σ). The fact that Kepler-13 is a near-even flux ratio binary is also not accounted for in the KIC. Barnes et al. (2011) could not account for any effects of the tertiary stellar companion Kepler-13 C upon the transit lightcurve, as this companion had not yet been discovered (Santerne et al. 2012). Kepler-13 C, however, should contribute somewhere between 0.8% and 0.03% of the total flux of the system, insufficient to significantly affect the dilution. Variability of either Kepler-13 B or C would need to occur on the orbital period of Kepler-13 Ab, or on a harmonic thereof, in order to systematically affect the light curve shape, which is unlikely. Finally, Barnes et al. (2011) found a rotation period of 22.0 hours for Kepler-13 A by fitting their model to the data, slightly shorter than the likely rotation period of 25.4 hours found by Szabó et al. (2014) in the Kepler data. While it is unclear whether the 25.4 hour period is indeed due to stellar rotation, if this is rotation then, given this and the likely too high value of $T_{\rm eff}$ assumed by Barnes et al. (2011), the actual temperature (and therefore surface brightness) contrast between the poles and equator of Kepler-13 A should be smaller than that assumed by Barnes et al. (2011). The effects of this upon the lightcurve shape and the resulting inferred spin-orbit misalignment, however, are not qualitatively obvious, and a quantitative analysis is beyond the scope of this work.

As noted above, there is a great deal of disagreement in the literature as to the value of the impact parameter b, with published values ranging from 0.253 (Szabó et al. 2012) to 0.75 (Mazeh et al. 2012; Szabó et al. 2011). As noted earlier, these discrepancies cannot be attributed to precession of the planetary orbital plane (Szabó et al. 2012). My value of $b = 0.256 \pm 0.030$ agrees to within 1σ only with the published measurement of Szabó et al. (2012), and is in disagreement with other published values by up to 16σ. I note that my value of the impact parameter is obtained directly from the spectroscopy, and is thus largely independent of the previous measurements from the *Kepler* photometry (although my model required the assumption of the transit duration from the photometry as a prior in the MCMCs). This suggests a possible reason for the discrepancy between my value of λ and that from Barnes et al. (2011). The value of λ derived from gravity darkening is dependent upon the choice of impact parameter; as the value of $b = 0.31962$ used by Barnes et al. (2011) differs from the $b = 0.256$ that I measured, it is perhaps unsurprising that the two values of λ are in disagreement.

After I published my work on Kepler-13 (Johnson et al. 2014), Masuda (2015) carried out a new analysis of the gravity-darkened *Kepler* lightcurve, using my value of λ as a prior to force the lightcurve model into agreement with my Doppler tomographic spin-orbit misalignment. In order to make this work they let both quadratic limb-darkening values float, unlike Barnes et al. (2011), who fixed one of the limb darkening parameters. Masuda (2015) was thus able to reconcile the gravity darkening and Doppler tomographic values of the spin-orbit misalignment, and found $i_\star = 81 \pm 5^\circ$ and $\psi = 60 \pm 2^\circ$.

Despite the presence of an additional star in the Kepler-13 system, Barnes et al. (2011) disfavored emplacement of Kepler-13 Ab via Kozai cycles due to the young system age (~ 700 Myr, determined using isochrones by Szabó et al. 2011), its current circular orbit (Szabó et al. 2011) or very small eccentricity (Shporer et al. 2014), and the long timescale necessary for tidal semi-major axis damping. Barnes et al. (2011) estimated that, for an initial Kozai-driven eccentric orbit similar to that currently occupied by HD 80606 b, the required tidal damping timescale to circularize the orbit at Kepler-13 Ab's current location is $\sim 2 \times 10^{14}$ years. Barnes et al. (2011) also noted that planet-planet scattering remains viable if it took place early enough that a debris disk sufficiently massive to quickly damp out the planetary eccentricity remained in place. Given the characteristics of the Kepler-13 system and the highly inclined orbit that I found for Kepler-13 Ab, it seems natural that it could have been emplaced through migration within an inclined disk produced via the mechanism of Batygin (2012). This would require an inclination between the orbital plane of Kepler-13 Ab and that of Kepler-13 BC about Kepler-13 A. Unfortunately, due to the lack of information about the position angle of Kepler-13 Ab's transit chord relative to the Kepler-13 A-BC separation, and the long orbital period of Kepler-13 BC about A (the projected separation is ~ 500 AU), this relative inclination is unlikely to be measured in the foreseeable future. The mechanism proposed by Bate et al. (2010) could also naturally result in an inclined, circular orbit for Kepler-13 Ab, but would not require the presence of a binary companion. I note, however, that these arguments rest upon the tidal circularization timescale being longer than the age of the system; as tidal theory continues to be poorly understood, the eccentricity damping timescale may be very uncertain. Additionally, I note that due to these uncertainties I cannot definitively exclude any mechanisms for the emplacement of Kepler-13 Ab upon its current inclined orbit.

A 25.4-hour periodicity is evident in the Kepler lightcurves for Kepler-13. This was suggested to be due to either stellar pulsations (Shporer et al. 2011) or rotation (Szabó et al. 2012, 2014). Additionally, Santerne et al. (2012) found a 25.5-hour periodicity in their radial velocity measurements of Kepler-13 A. They noted that this radial velocity periodicity could also be due to either pulsations or rotation, but preferred the pulsation explanation because their measured radial velocity semi-amplitude of 1.41 ± 0.38 km s^{-1} is much larger than that expected from starspots and rotation. I folded my stellar radial velocities for Kepler-13 A (i.e., the radial velocity offset between the solar and stellar barycentric rest frames discussed earlier) on the period found by Santerne et al. (2012), and my data appear to exhibit a similar periodicity and phase. In order to quantify this effect, I computed the generalized Lomb-Scargle periodograms (Lomb 1976; Scargle 1982; Zechmeister & Kürster 2009) for the Santerne et al. (2012) dataset and my dataset. For the Santerne et al. (2012) data I found a best-fitting period of 25.5 hours, and for my dataset, I found a period of 24.7 hours. The false alarm probabilities for these frequencies are 0.9998 and 0.98, respectively, and so I do not consider the detections of these periodicities in the radial velocity data to be statistically significant.

I see no evidence for stellar non-radial pulsations in my data, as are seen for the δ Sct planet host WASP-33 (Collier Cameron et al. 2010b, and Chapter 5), although given the short time span of each of my observations ($\sim$ 1 hour) such long-period pulsations would not necessarily manifest in my data. In principle I could compare the overall line shape for Kepler-13 A between different transit observations, but the moving line profile of Kepler-13 B would complicate such an effort, and thus I did not attempt such an analysis. I estimated that γ Dor-like pulsations (similar in period to the Kepler-13 A periodicity, but typically exhibited by cooler stars) would result in radial velocity shifts of order meters per second (using the results of Mathias et al. 2004), far too small to be detected in my data or to affect my conclusions.

Barnes et al. (2011) noted that, in principle, the spin-orbit misalignment for

Kepler-13 Ab can be measured using a third mechanism: the photometric Rossiter-McLaughlin effect (Shporer et al. 2012; Groot 2012). Unfortunately, given the scatter in the single-quarter Barnes et al. (2011) lightcurve of ~ 40 ppm, and that they estimated the amplitude of the photometric Rossiter-McLaughlin effect to be ~ 4 ppm, this measurement is probably out of reach of even the full 16-plus quarter Kepler lightcurve.

3.2 Kepler-448 b

Kepler-448 b (aka KOI-12.01) is a warm Jupiter discovered by *Kepler*. It was validated by Bourrier et al. (2015), using their own Doppler tomographic observations with the SOPHIE spectrograph on the 1.93m telescope at the Observatoire de Haute-Provence, France. It has an orbital period of 17.9 days and, with a host star magnitude of $Kp = 11.353$, it is the brightest star known to host a transiting warm Jupiter that is not on a highly eccentric orbit. Additionally, with $v \sin i_\star = 60$ km s^{-1} (Bourrier et al. 2015), it is a good target for Doppler tomography.

I obtained my own Doppler tomographic dataset on this system using the HET and HRS. These data span parts of three transits, on 2012 May 21, 2013 Apr 25, and 2013 May 13 UT, as well as an out-of-transit template observation on 2013 Mar 27 UT. See Table 2.2 for more details of the observations.

In order to fully constrain the system parameters, I performed a joint fit to my Doppler tomographic data, the *Kepler* photometry, and radial velocity data from Lillo-Box et al. (2015). They obtained 47 radial velocity measurements of Kepler-448 over a span of 114 days using the CAFE spectrograph on the 2.2 m telescope at the Calar Alto Observatory, Spain. They obtained an upper limit on the mass of Kepler-448 b of $25.2 \pm 3.7\,M_J$, limiting it to be a planet or brown dwarf (using a smaller

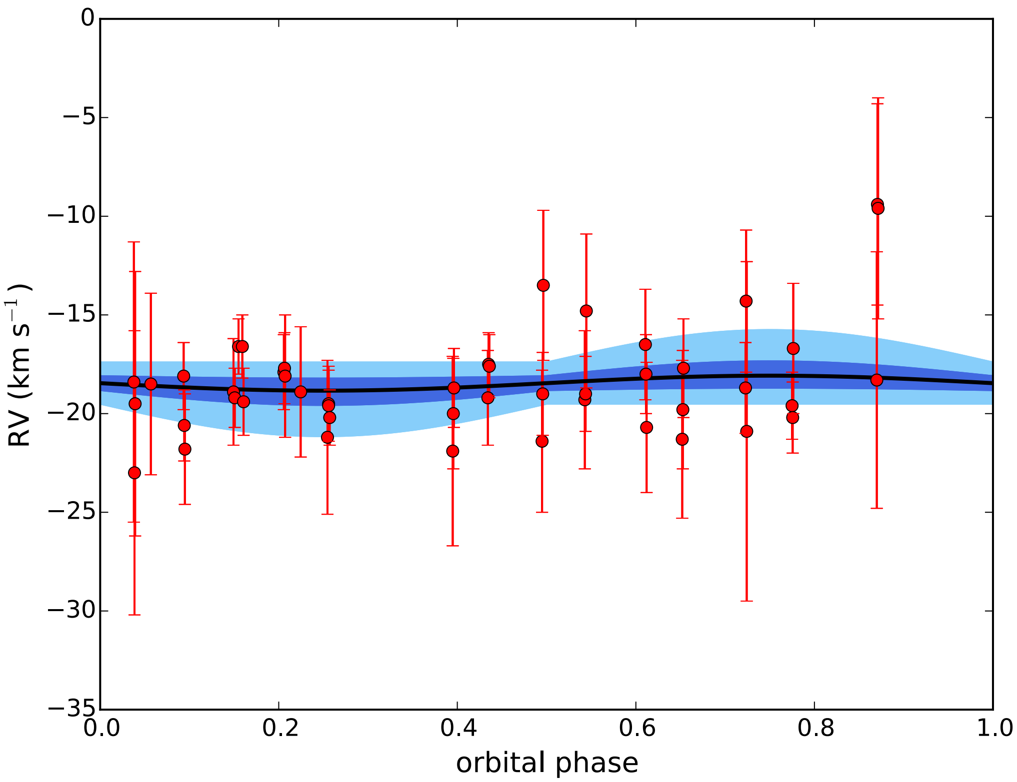

Figure 3.6 Radial velocity measurements of Kepler-448 from Lillo-Box et al. (2015), phased on the transit period and with the best-fit model from my MCMC overplotted in black. The dark and light blue regions show the 1σ and 3σ credible regions, respectively, due to uncertainty in K and γ; I neglect uncertainties in other parameters (e.g., P) because they are proportionally much smaller.

dataset, Bourrier et al. 2015, limited the mass to $< 8.7\,M_J$ at 3σ). I show the data from Lillo-Box et al. (2015) in Fig. 3.6. For simplicity I assumed a circular orbit for Kepler-448 b.

The lightcurve of Kepler-448 shows rotational modulation with an amplitude of $\sim 0.1{-}0.2\%$ and a period of ~ 1.5 days. I investigate the properties of this modulation in §3.2.1 below, but in order to model the photometric transit data it was necessary to remove this variability. For each transit I fit a quadratic function to the *Kepler* short cadence out-of-transit flux within one transit duration (7.4 hours) of the transit center, and divided out this fit to produce a flattened, normalized transit lightcurve. This produced good results for most of the transits, except for two where the shape was highly distorted due to lack of data before and/or after the transit, which I excluded from the dataset used in my fits. The remaining transits often still show some low-level distortions, but these should average out when fitting many transits. Indeed, my final best-fit transit lightcurve (Fig. 3.7) well-reproduces the data. I produced the transit lightcurve model using the `BATMAN` Python package (Kreidberg 2015).

An additional complication for the Doppler tomographic analysis was that two of the four datasets, the in-transit data from 2013 April 25 and the template data (taken on 2013 March 27), were contaminated with the solar spectrum reflecting off the Moon and scattering through the Earth's atmosphere and light clouds and into the telescope. This resulted in a narrow absorption line profile superposed upon the rotationally broadened line profile of Kepler-448 b. I dealt with this complication by including this additional line profile in my model. I assumed that the solar line profile was unresolved and thus I could model it as simply the instrumental line profile. I added it to the model line profiles of Kepler-448 b on these nights, and added two additional parameters to the MCMC to govern the behavior of this line: the line depth and line central velocity.

I simultaneously fit the Doppler tomographic, photometric, and radial velocity data using `emcee`. The MCMC used 16 parameters: the planetary orbital period P, transit epoch T_0, radius ratio $R_P/R_\star$, scaled semi-major axis $a/R_\star$, impact parameter b, spin-orbit misalignment λ, projected stellar rotational velocity $v \sin i_\star$, radial velocity semi-amplitude K and velocity offset γ, the intrinsic (Gaussian) stellar line width,

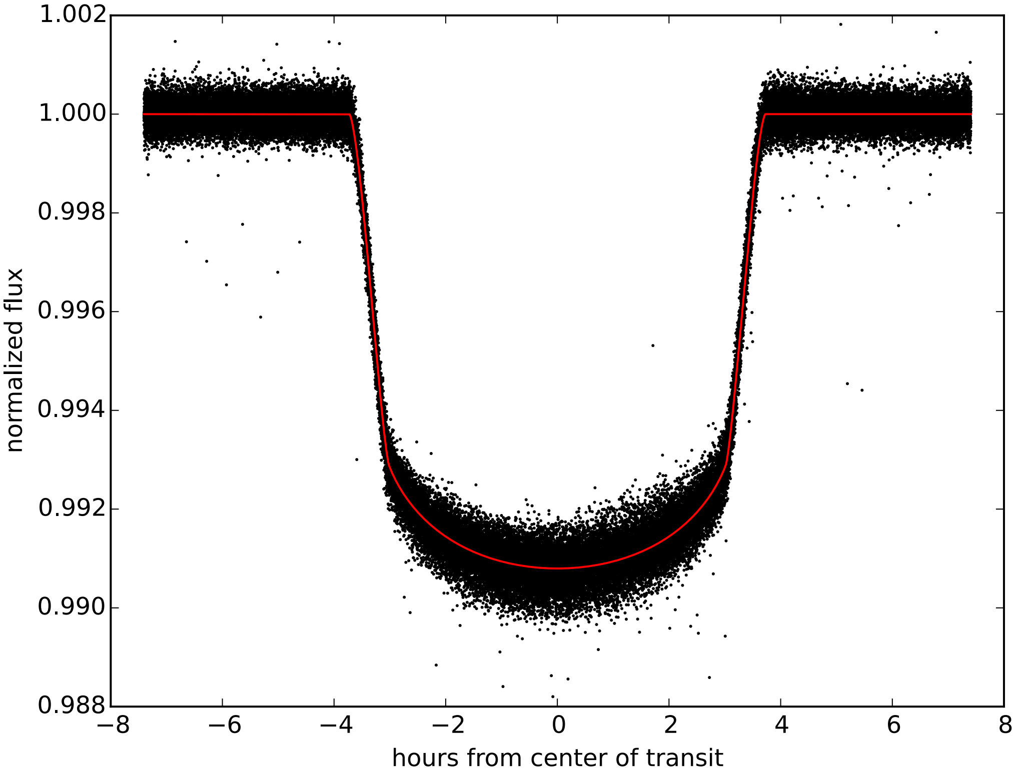

Figure 3.7 *Kepler* short-cadence data in and near the transit of Kepler-448 b, phased to the orbital period and with my best-fit photometric transit model overplotted in red. I removed the stellar variability as described in the text, and excluded two transits for which this process resulted in highly distorted transit shapes; this figure includes data from the other 77 transits observed by *Kepler* in short cadence.

the central velocity and depth of the contaminating solar line, and two limb darkening parameters each for the Doppler tomographic and photometric datasets. I used an ensemble of 100 walkers and ran these for 100,000 steps, cutting off the first 20,000 steps of burn-in, for a total of 8 million samples from the posterior distributions.

I show the time series line profiles residuals for Kepler-448 b in Fig. 3.8, and the best-fit models for the radial velocity and photometric data in Figs. 3.6 and 3.7, respectively. Using the MCMC, I measured a spin-orbit misalignment of $\lambda =$

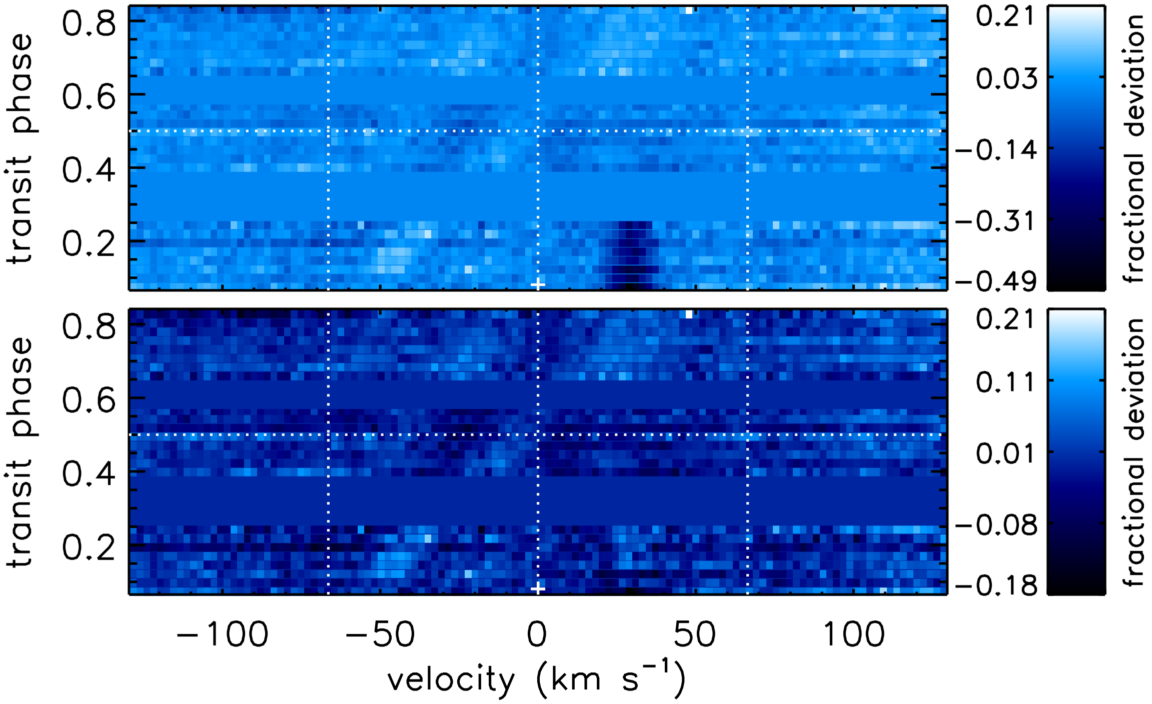

Figure 3.8 Time series line profile residuals for Kepler-448 b. Top: the raw time series line profile residuals, showing the contaminating line due to moonlight. Bottom: with the best-fit model of the moonlight removed. The transit signature is the bright streak moving from lower left to upper right. The significant systematics are likely line profile perturbations caused by the same starspots responsible for the photometric variability of Kepler-448. Flat blue regions denote parts of the transit where I do not have observations.

$-1.7^{+1.7\circ}_{-2.1}$. This is 4.2σ discrepant from the value of $12.5^{+3.0\circ}_{-2.9}$ found by Bourrier et al. (2015); likely both works underestimated the systematic uncertainties in the results. Nonetheless, given the long orbital period and small tidal damping for Kepler-448 b, this suggests that the planet likely formed in and migrated through a well-aligned protoplanetary disk. The system parameters that I measured are listed in the bottom section of Table 3.4. These are generally compatible with those found by Bourrier et al. (2015), with the sole exception of λ. I found a radial velocity semi-amplitude of $K = 0.38^{+0.38}_{-0.26}$ km s^{-1} (corresponding to a planetary mass of $M_P = 6.3^{+6.3}_{-4.3}\,M_J$, assuming the stellar mass from Bourrier et al. 2015); however, given that these values

Table 3.4. System Parameters of Kepler-448

Parameter	This Work	Bourrier et al. (2015)
Stellar Parameters		
$T_{\rm eff}$ (K)	...	6820 ± 120
$M_\star (M_\odot)$	...	1.452 ± 0.093
$R_\star (R_\odot)$	...	1.63 ± 0.15
$P_{\rm rot}$ (days)	1.27 ± 0.11	...
Measured Parameters		
P (days)	$17.85523220 \pm 5.3 \times 10^{-7}$	$17.8552332 \pm 1.0 \times 10^{-6}$
T_0 (BJD)	$2454979.596046 \pm 2.4 \times 10^{-5}$	$2454979.59601 \pm 0.5 \times 10^{-4}$
$R_P/R_\star$	$0.090545^{+0.000029}_{-0.000033}$	$0.09049 \pm 8 \times 10^{-5}$
$a/R_\star$	$18.808^{+0.021}_{-0.018}$	18.84 ± 0.04
b	$0.3676^{+0.0025}_{-0.0030}$	$0.362 \pm 7 \times 10^{-3}$
$\lambda(^\circ)$	$-1.7^{+1.7}_{-2.1}$	$12.5^{+3.0}_{-2.9}$
$v \sin i_\star$	66.43 ± 0.40	$60.0^{+0.9}_{-0.8}$
K (km s^{-1})	$0.38^{+0.38}_{-0.26}$	< 0.51 (3σ)
intrinsic line width (km s^{-1})	$11.36^{+0.44}_{-0.45}$	...
Derived Parameters		
$M_P (M_J)$[a]	$6.3^{+6.3}_{-4.3}$	< 8.7 (3σ)
$R_P (R_J)$[a]	1.44 ± 0.13	1.44 ± 0.13

Note. — Uncertainties are purely statistical and do not take into account systematic sources of error. Measured parameters are those that I measured directly with the MCMC, while Derived Parameters were calculated analytically from the Measured Parameters.

[a] To calculate the planetary mass and radius I assumed the stellar parameters found by Bourrier et al. (2015), as I did not calculate my own values of these parameters.

differ from zero at a level of only 1.46σ, I cannot claim a detection of the radial velocity reflex motion.

3.2.1 The Rotation Period of Kepler-448

The most obvious features in the *Kepler* lightcurve of Kepler-448 (Fig. 3.9) are the planetary transits (period 17.9 days) and a quasi-sinusoidal modulation of maximum amplitude $\sim 0.2\%$, which changes in amplitude and phase on timescales of tens of days. I attribute this signal to rotational modulation, as spots on the stellar surface

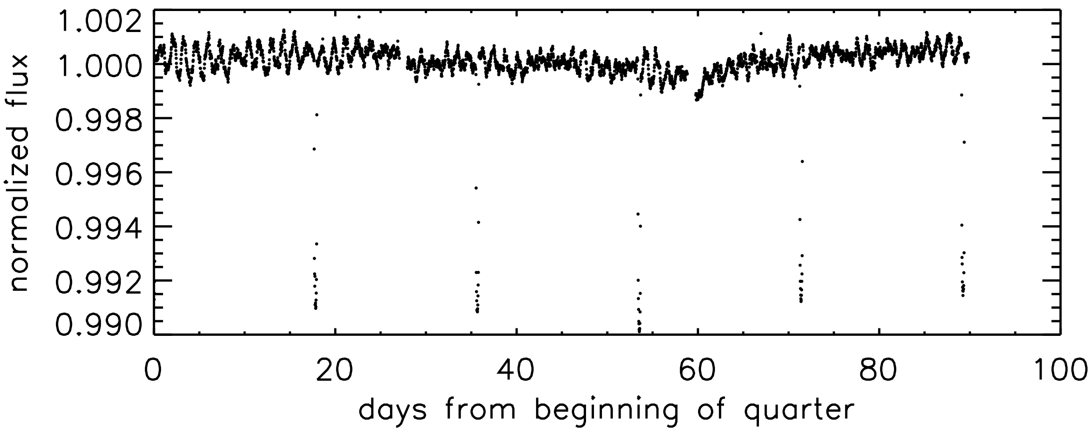

Figure 3.9 A representative *Kepler* light curve of Kepler-448, showing the rotational variability and the planetary transits. These data are from Quarter 6 of the *Kepler* mission. The data are short cadence, which are broken into three shorter intervals for each quarter, hence the discontinuities at ~ 28 and ~ 60 days after the start of the quarter.

move in and out of view; the variability is too irregular to be due to stellar pulsations.

In order to investigate this signal further, I followed the methodology of McQuillan et al. (2013), who developed tools to investigate rotational modulation in *Kepler* data. For each *Kepler* quarter, I calculated the autocorrelation function (ACF) of the long cadence lightcurve. Each ACF shows a peak at a period of ~ 1.3 days, plus a series of peaks spaced at intervals of approximately 1.3 days. In principle, any peak may be the rotation period, with peaks at shorter periods due to spots on opposite sides of the star resulting in periodicity on half the true rotation period. Nonetheless, I attribute the 1.3 day peak to the rotation period for the following reason. The rotation period, equatorial velocity, and stellar radius are related by $P_{\rm rot} = 2\pi R_\star / v_{\rm eq}$, where the equatorial velocity is $v_{\rm eq} = (v \sin i_\star)/\sin i_\star$. Given measured values of $P_{\rm rot}$ and $v \sin i_\star$, I therefore have $R_\star \sin i_\star = P_{\rm rot} v \sin i_\star / 2\pi$. The minimum possible value for $R_\star$ will occur for $i_\star = 90°$, with smaller values of $i_\star$ requiring larger values of $R_\star$.

A rotation period of 1.3 days and a $v \sin i_\star$ of 68 km s^{-1} would thus give a minimum stellar radius of 1.7 $R_\odot$, broadly consistent with the stellar parameters derived from spectroscopy. If the second peak, at ~ 2.6 days, instead corresponds to the rotation period, this would imply a minimum stellar radius of 3.5 $R_\odot$, inconsistent with the known stellar parameters. This also implies that $\sin i_\star \sim 90^\circ$, and thus that the full three-dimensional spin-orbit misalignment is also small, $\psi \sim 0^\circ$.

For each of the eight quarters with a well-behaved ACF (i.e., with distinct, approximately equally spaced peaks in the 1-5 day range and without an excess of power at short periods), I measured the rotation period from the location of the peak near 1.3 days, and the uncertainty in the period from the half width half max of the peak, following McQuillan et al. (2013). I then took the final rotation period to be the mean of the periods measured for each of these quarters. This resulted in a period of $P_{\rm rot} = 1.27 \pm 0.11$ days.

McQuillan et al. (2013), however, noted that the ACF method is not necessarily reliable for rotation periods below 7 days. In order to double-check my results, I also calculated the Lomb-Scargle periodogram (Lomb 1976; Scargle 1982; Zechmeister & Kürster 2009) of the *Kepler* lightcurve for each quarter. For the same quarters that I used to measure the period from the ACF, the mean period measured from the Lomb-Scargle periodogram was 1.26 days, in good agreement with the value found by the ACF method. I thus adopt $P_{\rm rot} = 1.27 \pm 0.11$ days as the rotation period of Kepler-448.

3.3 WASP-79 b

WASP-79 b is a hot Jupiter that was originally discovered by Smalley et al. (2012). It orbits a relatively bright ($V = 10.1$) F5 star with a period of 3.662 days. The star is mildly rapidly rotating, with $v \sin i_\star = 19.1 \pm 0.7$ km s^{-1}. Smalley et al. (2012) produced two sets of system parameters, one assuming a main sequence primary (i.e., enforcing the main sequence $M_\star - R_\star$ relation in their global fit) and one assuming a non-main sequence host (no $M_\star - R_\star$ relation assumed). I quote the literature parameters of the WASP-79 in Table 3.5.

WASP-79 is too far south ($\delta = -30°$) to observe effectively from McDonald. The star was observed using radial velocity Rossiter-McLaughlin methodology by Addison et al. (2013), who measured a spin-orbit misalignment of $\lambda = -106^{+19}_{-13}{}^\circ$ (and a second solution of $\lambda = -84^{+23}_{-30}{}^\circ$ by assuming the parameters of the non main sequence solution from Smalley et al. 2012). Due to the relatively rapid stellar rotation and the fact that the high wavelength stability necessary for precise radial velocity observations was obtained using simultaneous ThXe calibration (rather than through the use of an iodine cell), these data are also amenable to Doppler tomographic analysis. Addison et al. (2013) generously shared their data with me, and in this section I analyze these data.

The Addison et al. (2013) dataset was obtained using the 3.9 m Anglo-Australian Telescope (AAT) at Siding Spring Observatory, Australia. Addison et al. (2013) used the CYCLOPS2 optical fiber bundle and the University College London Échelle Spectrograph (UCLES) to observe WASP-79 during the transit of 2012 Dec 23 UT. They obtained a total of 23 spectra, beginning just before ingress and continuing for about three hours after egress (see Table 2.2 for more details of the observations). These data have $R = 70,000$ and wavelength coverage from 4550 Å to 7350 Å (Addison

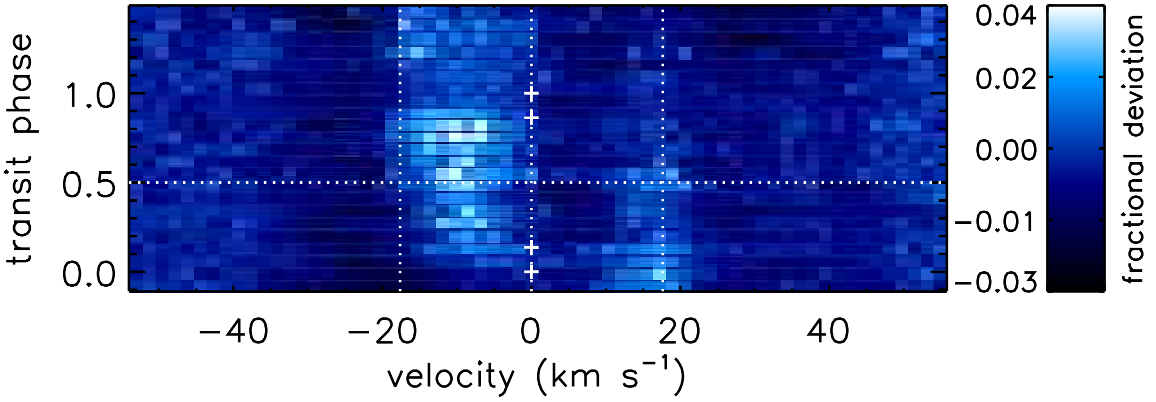

Figure 3.10 Time series line profile residuals showing a transit of WASP-79 b. In order to make this figure I subtracted the best-fit model line profile found by the MCMC from the time series line profiles. The transit signature is the bright vertical streak to the left of center. Systematics in the first few spectra are due to small velocity registration errors of the line profiles.

et al. 2013). I analyzed these data using my Doppler tomographic methodology, and show the time series line profile residuals in Fig. 3.10. I easily detect the transit.

The two solutions for the system parameters from Smalley et al. (2012) have different values of several of my MCMC parameters, most notably b (0.570 ± 0.052 for the main sequence case and 0.706 ± 0.031 for non main sequence solution), but also $R_P/R_\star$ and $a/R_\star$. I consequently ran two separate MCMCs, one assuming the main sequence values from Smalley et al. (2012) as the starting values and priors on P, T_0, $R_P/R_\star$, and $a/R_\star$, and the other using the non main sequence values. Due to the highly-inclined orbit of WASP-79 b, the path of the transit signature is highly sensitive to the impact parameter b, and so I let this parameter float. For this system I fit directly to the time series line profiles, treating limb darkening as described earlier. I ran 100 MCMC walkers for 100,000 steps and cut off the first 20,000 steps of burn-in, producing 8 million samples from the posterior distributions for each of the main sequence and non main sequence solutions.

Table 3.5. System Parameters of WASP-79

Parameter	Value (MS; preferred)	Value (non-MS)	Source
Stellar Parameters			
$T_{\rm eff}$ (K)	6600 ± 100	6600 ± 100	Smalley et al. (2012)
$M_\star\,(M_\odot)$	1.56 ± 0.09	1.52 ± 0.07	Smalley et al. (2012)
$R_\star\,(R_\odot)$	1.64 ± 0.08	1.91 ± 0.09	Smalley et al. (2012)
Planetary Parameters			
$M_P\,(M_J)$	0.90 ± 0.09	0.90 ± 0.08	Smalley et al. (2012)
$R_P\,(R_J)$	1.70 ± 0.11	2.09 ± 0.14	Smalley et al. (2012)
MCMC Inputs			
P (days)	3.6623817 ± 0.0000051	3.6623866 ± 0.0000085	Smalley et al. (2012)
T_0 (BJD_TDB)[a]	$2455545.23555 \pm 0.00125$	$2455545.0.23606 \pm 0.00150$	Smalley et al. (2012)
$R_P/R_\star$[a]	0.1071 ± 0.0024	0.1126 ± 0.0028	Smalley et al. (2012)
$a/R_\star$[a]	7.1 ± 1.1	6.05 ± 0.52	Smalley et al. (2012)
b	0.570 ± 0.052	0.706 ± 0.031	Smalley et al. (2012)
Rossiter-McLaughlin Parameters			
λ (°)	-106^{+19}_{-13}	-84^{+23}_{-30}	Addison et al. (2013)
$v \sin i_\star$ (km s^{-1})	$17.5^{+3.1}_{-3.0}$	16.0 ± 3.7	Addison et al. (2013)
Measured Parameters			
b	0.541 ± 0.016	0.553 ± 0.016	this work
λ (°)	-98.3 ± 1.9	-97.7 ± 1.9	this work
$v \sin i_\star$ (km s^{-1})	$17.347^{+0.073}_{-0.043}$	$17.356^{+0.075}_{-0.044}$	this work
intrinsic line width (km s^{-1})	$5.460^{+0.055}_{-0.062}$	$5.452^{+0.055}_{-0.062}$	this work

Note. — Uncertainties are purely statistical and do not take into account systematic sources of error. The parameters in the MCMC Inputs section were MCMC parameters on which I put Gaussian priors using the best-fit parameter and uncertainty from Smalley et al. (2012). Rossiter-McLaughlin Parameters are those measured by Addison et al. (2013) in their analysis. Measured parameters are those that I measure directly with the MCMC.

[a] Calculated from the parameters given in the literature source.

I list the parameters that I find for WASP-79 b in the bottom section of Table 3.5. The values of λ that I find are consistent with those found by Addison et al. (2013), but about an order of magnitude more precise (although, again, my uncertainties are purely statistical and likely underestimated as I do not fully take into account systematic sources of uncertainty). My results are insensitive to the choice of priors (i.e., the main sequence vs. non main sequence solutions of Smalley et al. 2012); my best-fit values of λ, b, $v \sin i_\star$, and the intrinsic Gaussian line width all vary by $< 0.6\sigma$ between the two solutions. Interestingly, the value of b that I find for the main sequence priors is consistent (0.5σ difference) with that found by Smalley et al. (2012), but that for the non main sequence priors is significantly discrepant with that from Smalley et al. (2012)–4.4σ–but in agreement with my value of b from the main sequence priors. Since my measurement of b is largely independent from the choice of priors, and both cases agree with the main sequence solution of Smalley et al. (2012), I conclude that this is likely to be the correct solution for the system and adopt the solution with main sequence priors as the preferred solution.

3.4 HAT-P-41 b

HAT-P-41 b is a hot Jupiter discovered by Hartman et al. (2012). It orbits a mildly rapidly rotating ($v \sin i_\star = 19.6$ km s^{-1}) star every 2.69 days; the star has $T_{\rm eff} =$ 6390 K, and is thus above the 6250 K boundary where many planets are misaligned. The planet has a mass of $0.8\,M_J$ and, with a radius of $1.7\,R_J$, it is highly inflated. I list the parameters of the system in Table 3.6. The $v \sin i_\star$ value is high enough for the system to be amenable to Doppler tomographic observations.

Consequently, parts of five transits were observed with the HET and HRS between 2013 June and August. I summarize the observations in Table 2.2, and show the time series line profile residuals in the top panel of Fig. 3.11. It is apparent by inspection that the orbit of HAT-P-41 b is prograde, but I do not robustly detect the transit signature in all of the datasets; indeed, it is only significantly detected in the datasets from 2013 June 27 and July 24, which together cover approximately the first one-third of the transit. My efforts to modify my line profile extraction code to detect the transits in the other datasets are ongoing, and so for the time being I will restrict myself to analysis of the two datasets mentioned above. Due to the limited coverage of the transit my measurement of λ will perforce be less precise than one measured from the full five datasets would be. I show the time series line profile residuals from these two datasets alone in the bottom panel of Fig. 3.11.

As was the case for Kepler-448 b, there is an additional line profile component due to scattered moonlight in the data obtained on 2013 July 24. Here, however, the scattered solar line profile does not significantly overlap with the stellar line profile–it is centered at ~ -35 km s^{-1}, while the star has $v \sin i_\star = 19.6 \pm 0.5$ km s^{-1} (Hartman et al. 2012), and so I can safely neglect this contaminating line profile.

In the MCMC that I used to extract the transit parameters for HAT-P-41 b, I set a prior upon b, using the value and uncertainty found by Hartman et al. (2012). The reason for this is that, while fitting to only a small part of the transit and with a relatively low-inclination orbit, b is poorly constrained by the Doppler tomographic data alone. As b is already well-determined from the photometry of Hartman et al. (2012), I can obtain a more precise measurement of λ by setting this prior upon b. All in all, I set priors upon the two limb darkening parameters, T_0, P, $R_P/R_\star$, $a/R_\star$, and b, and let λ, $v \sin i_\star$, and the intrinsic line width float.

I summarize my results in the bottom section of Table 2.2. The posterior distribution for λ is bimodal, allowing two solutions: either $\lambda = 18.4^{+10.0\circ}_{-8.5}$, or $\lambda = -57.2^{+8.4\circ}_{-7.5}$.

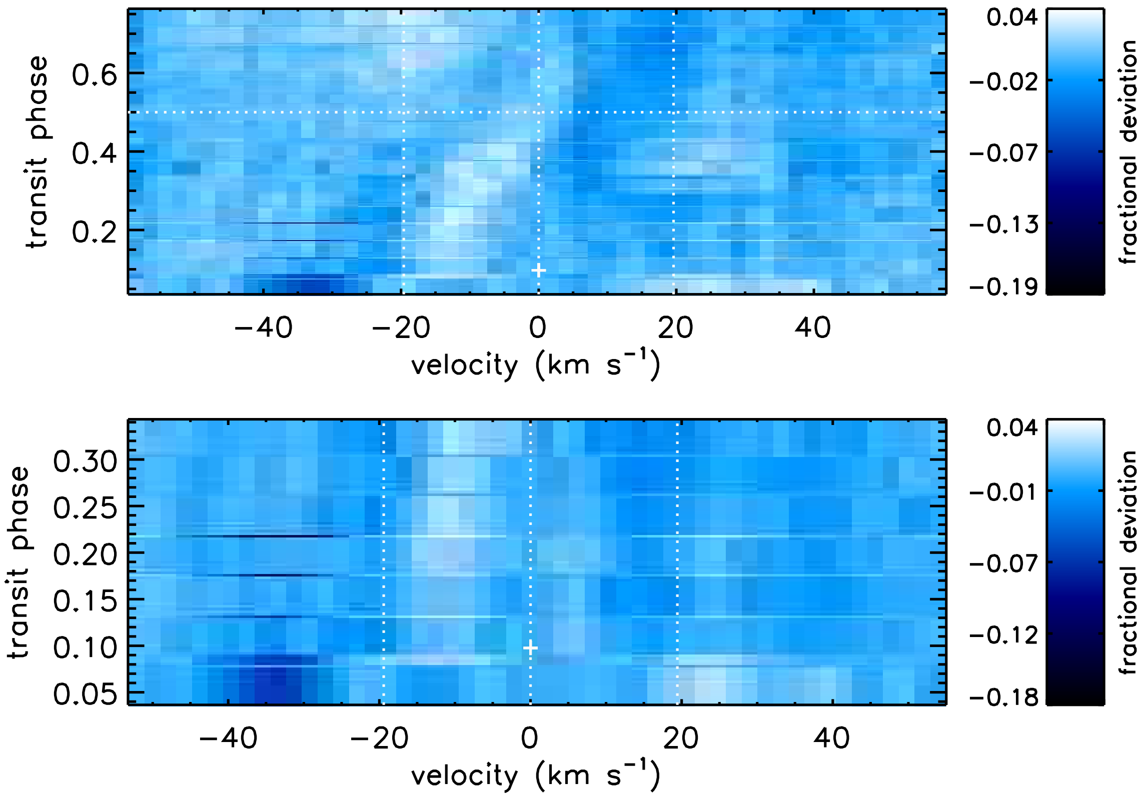

Figure 3.11 Top: time series line profile residuals showing the transit of HAT-P-41 b, using all five of my in-transit datasets. The transit signature is the light blob moving from lower left towards the upper right, but it is not robustly detected in the datasets from later in the transit. The dark area at lower left is the contaminating solar line in the dataset from 2013 July 24, but it is only partially visible as it is partially overlain by the dataset from 2013 June 27, which covers much of the same portion of the transit. Bottom: time series line profile residuals of only the transits of 2013 June 27 and July 24, which I used to obtain the best-fit parameters listed in Table 3.6.

Table 3.6. System Parameters of HAT-P-41

Parameter	Value	Source
Stellar Parameters		
$T_{\rm eff}$ (K)	6390 ± 100	Hartman et al. (2012)
$M_\star\,(M_\odot)$	1.418 ± 0.047	Hartman et al. (2012)
$R_\star\,(R_\odot)$	$1.683^{+0.058}_{-0.036}$	Hartman et al. (2012)
Planetary Parameters		
$M_P\,(M_J)$	0.800 ± 0.102	Hartman et al. (2012)
$R_P\,(R_J)$	$1.685^{+0.076}_{-0.051}$	Hartman et al. (2012)
MCMC Inputs		
P (days)	2.694047 ± 0.000004	Hartman et al. (2012)
T_0 (BJD)	$2454983.86167 \pm 0.00107$	Hartman et al. (2012)
$R_P/R_\star$	0.1028 ± 0.0016	Hartman et al. (2012)
$a/R_\star$	$5.44^{+0.09}_{-0.15}$	Hartman et al. (2012)
b	$0.222^{+0.088}_{-0.093}$	Hartman et al. (2012)
Measured Parameters		
$\lambda\,(^\circ)$	$-57.2^{+8.4}_{-7.5}$ or $18.4^{+10.0}_{-8.5}$	this work
$v \sin i_\star$ (km s^{-1})	$19.9^{+2.3}_{-1.1}$	this work
intrinsic line width (km s^{-1})	$11.18^{+0.40}_{-0.84}$	this work

Note. — Uncertainties are purely statistical and do not take into account systematic sources of error. The parameters in the MCMC Inputs section were MCMC parameters on which I put Gaussian priors using the best-fit values and uncertainties from Hartman et al. (2012). Measured parameters are those that I measured directly with the MCMC.

The mean values of the other parameters corresponding to the two different solutions in λ differ from each other by no more than 0.36σ. Such bimodal solutions for λ can often occur if only part of a transit is observed (cf. Hartman et al. 2015, who obtained a bimodal solution for the spin-orbit misalignment of HAT-P-57 b with observations of a partial transit). Once I am able to detect the transit signature in all of my in-transit datasets, this will likely allow me to eliminate one of the possible solutions for λ. Since HAT-P-41 has $T_{\rm eff} > 6250$ K, I cannot use the λ versus $T_{\rm eff}$ distribution of Winn et al. (2010a) to say that the solution with the smaller misalignment ($\lambda = 16.9^{+9.5\circ}_{-9.9}$) is more likely *a priori*. Indeed, the higher-inclination solution

($\lambda = -57.2^{+8.4\circ}_{-7.5}$) is a slightly better fit to the data, but the two solutions only have $\Delta\chi^2_{\rm red} = 0.04$, so I cannot exclude the low-inclination solution on this basis alone.

3.5 KELT-2 Ab

KELT-2 Ab (aka HD 42176 b) is a hot Jupiter discovered by Beatty et al. (2012). It has an orbital period of 4.11 days. Its host star has $T_{\rm eff} = 6147$ K, and, with $v \sin i_\star = 9.0 \pm 2.0$ km s^{-1}, it is only slightly rapidly rotating. It is, however, one of the brightest stars known to host a transiting hot Jupiter, with $V = 8.77$. Despite the relatively slow rotation, with a $v \sin i_\star$ similar to the width of the HET/HRS instrumental profile, I nonetheless obtained observations of parts of two transits with HET/HRS, and part of a third with the HJST and TS23. I show these data in the top and bottom panels of Fig. 3.12, respectively. Unfortunately, due to the barely resolved stellar lines I was unable to detect the Doppler tomographic transit signature. Measurement of the spin-orbit misalignment of KELT-2 Ab will require either Doppler tomographic observations with higher spectral resolution, or radial velocity Rossiter-McLaughlin observations. Indeed, Beatty et al. (2012) calculated that the Rossiter-McLaughlin amplitude should be ~ 44 m s^{-1}, easily measurable for such a bright star. The relatively close nature of the stellar binary, however (KELT-2 B is 2.3" from the primary and about 3 magnitudes fainter in the V band) may complicate any such observations.

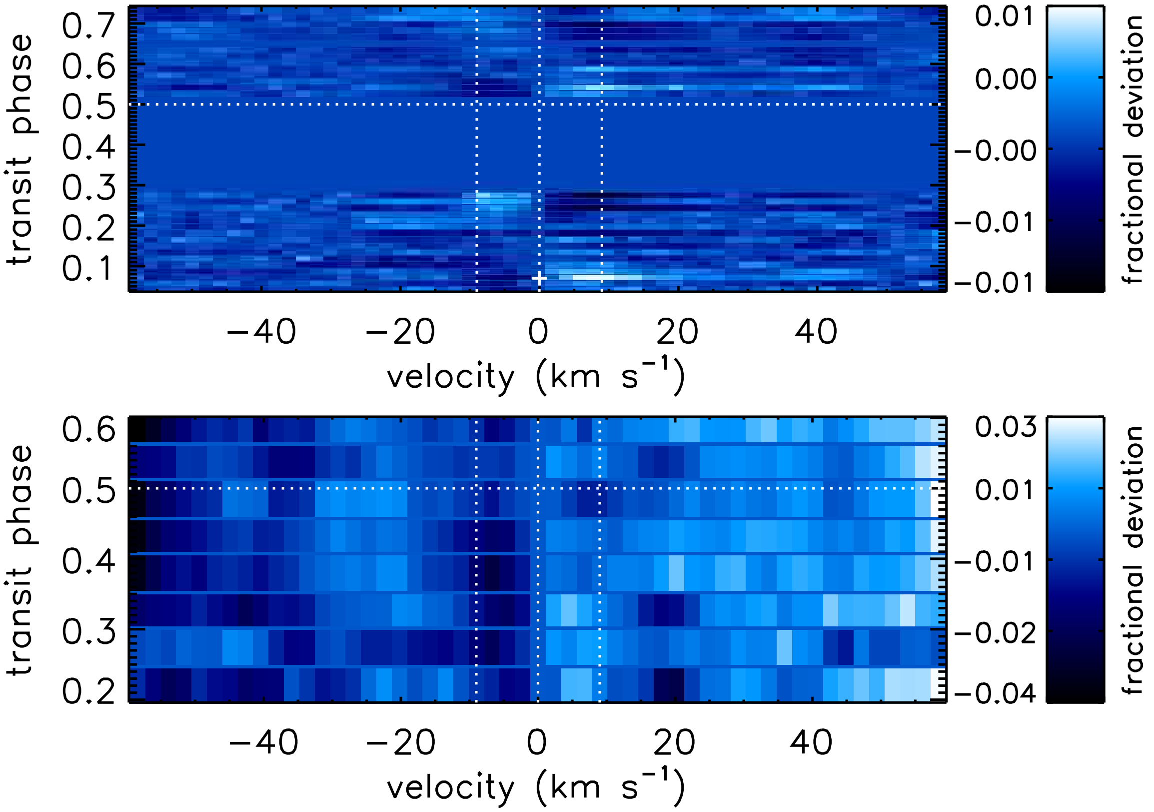

Figure 3.12 Time series line profile residuals showing two partial transits of KELT-2 Ab from the HET (top) and one partial transit from the HJST (bottom). The transit signature is not evident. The systematics within the line profile in the HET data are likely due to uncorrected radial velocity drifts of the spectrograph over the course of the observations, and only superficially mimic a Doppler tomographic transit signature.

Chapter Four: Planet Candidate Validation

4.1 KOI-368.01

The *Kepler* candidate KOI-368.01 is the longest-period object considered in this dissertation, with an orbital period of 110 days. Unlike the other objects that I have observed, it is unlikely to be a planet–Zhou & Huang (2013) detected a secondary eclipse in the *Kepler* lightcurve, which suggests an equilibrium temperature too high to be caused by stellar irradiation at the relatively large separation of KOI-368.01. KOI-368.01 is therefore likely significantly self-luminous, i.e., it is a star; Zhou & Huang (2013) found a secondary $T_{\rm eff} = 3060 \pm 50$ K, corresponding to an M dwarf.

Like Kepler-13 A, the star KOI-368 is sufficiently rapidly rotating that it is dynamically oblate enough to display an asymmetric transit shape (e.g., Barnes 2009). The asymmetric transit shape was used to measure the spin-orbit misalignment by both Zhou & Huang (2013) and Ahlers et al. (2014). These two works, however, found very different values of the spin-orbit misalignment, and of the system's dynamical state as a whole. Zhou & Huang (2013) found a sky-projected spin-orbit misalignment of $\lambda = 36^{+23\circ}_{-17}$ and a three-dimensional misalignment of $\psi = 69^{+9}_{-10}{}^\circ$–i.e., a highly misaligned transiting object. Ahlers et al. (2014), on the other hand, found values of $\lambda = 10 \pm 2^\circ$ and $\psi = 11 \pm 3^\circ$ (note that they denoted $i_\star$ as ψ and ψ as φ), i.e., a well-aligned orbit of the transiting object. As was the case for Kepler-13 Ab (Barnes et al. 2011, discussed in §3.1), there are also corresponding retrograde solutions degenerate with those found by Zhou & Huang (2013) and Ahlers et al. (2014), with $\lambda = 144^{+17\circ}_{-23}$ and $\lambda = 170 \pm 2^\circ$, respectively; however, both works quoted only the prograde solution as this is more likely *a priori*. I list the full system parameters found by Zhou & Huang (2013) and Ahlers et al. (2014) in Table 4.1. The differences between the two works are likely related to different treatment of the stellar limb darkening or the gravity darkening parameter β (e.g., Masuda 2015). A measurement of the sky-projected spin-orbit misalignment using Doppler tomography could resolve the impasse between these two solutions, and allow one to back out the true values of the limb darkening or gravity darkening coefficients.

Doppler tomographic observations, however, are challenging due to the long orbital period (110 days) and long transit duration (13 hours). There are therefore only one or two observable transits during a given observing season, significantly limiting opportunities for observations. On the other hand, the long transit duration allows me to integrate for longer, as the transiting object is moving more slowly across the stellar disk than a hot Jupiter would.

I obtained observations during the transit of KOI-368.01 on 2011 August 29 UT using HET/HRS. These observations consisted of seven spectra, beginning 75% of the way through the transit and ending 83% through the transit duration. I show the time series line profile residuals in Fig. 4.1. I note that KOI-368.01 was also observed using the HJST and TS23 (Table 2.2), but as this dataset has very low signal-to-noise (average SNR$\sim$ 40), I did not analyze these data.

The individual time series line profiles from the HET are too noisy to allow me to detect the transit signature. Using the shifting and binning method (§2.2.1), however, I obtain a possible detection of the transit signature at a significance level of $\sim 2\sigma$ (i.e., comparing the peak of the possible transit signature to the overall noise level in the map). These data are shown in Fig. 4.2.

The transit parameters implied by this tentative detection are very unconstrained,

Table 4.1. System Parameters of KOI-368

Parameter	Zhou & Huang (2013)	Ahlers et al. (2014)	This Work
Stellar Parameters			
T_{eff} (K)	9250 ± 200	...	...
$\log g$ (cgs)	4.02 ± 0.01	...	...
$M_\star\,(M_\odot)$	2.3 ± 0.1	...	...
$R_\star\,(R_\odot)$	2.4 ± 0.1	2.28 ± 0.02	...
Transit Parameters			
P (days)	110.32164 ± 0.00001	...	...
T_0 (BJD)	2455030.3645 ± 0.0002	...	...
$R_P/R_\star$	0.0863 ± 0.0004	0.0823	...
$a/R_\star$	$52.73 \pm 0.26^{\mathrm{a}}$	...	...
b	$0.7041^{+0.0073\mathrm{a}}_{-0.0090}$	0.697	...
$R_P\,(R_J)$	$2.053 \pm 0.058^{\mathrm{a}}$	1.83 ± 0.02	...
Measured or Estimated Parameters			
λ (°)	36^{+23}_{-17}	10 ± 2	$\sim 55 - 80$?
$v \sin i_\star$	79 ± 4	...	$81.20^{+0.43}_{-0.30}$
intrinsic line width	...	...	$17.59^{+0.35}_{-0.39}$
ψ (°)[b]	69^{+9}_{-10}	11 ± 3	...
$i_\star$ (°)[c]	55^{+3}_{-10}	3 ± 7	...

Note. — Uncertainties are purely statistical and do not take into account systematic sources of error. In the Measured or Estimated Parameters section, I measured $v \sin i_\star$ and the intrinsic line width directly with the MCMC, and estimated λ qualitatively from the map shown in Fig. 4.2 plus the values of b found by Zhou & Huang (2013) and Ahlers et al. (2014).

[a] Calculated from values given in the source.

[b] Denoted φ by Ahlers et al. (2014).

[c] Denoted i_{rot} by Zhou & Huang (2013) and ψ by Ahlers et al. (2014).

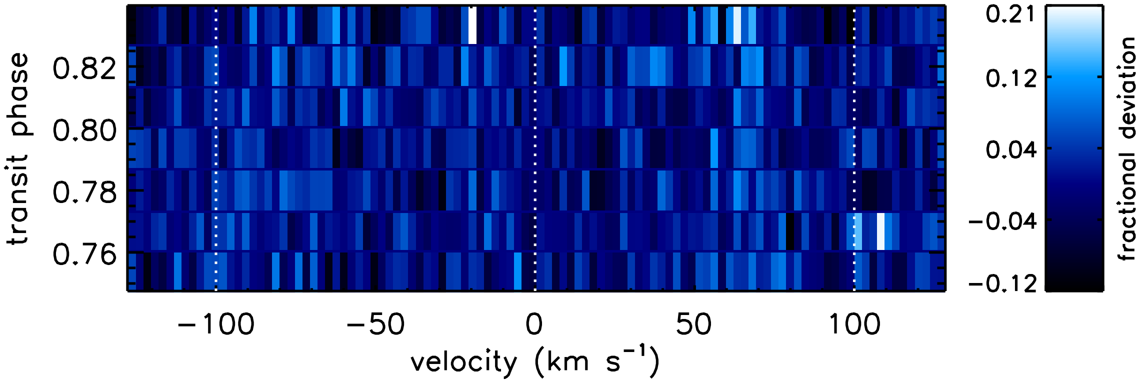

Figure 4.1 Time series line profile residuals for KOI-368.01. The transit signature is not visible.

as the data only cover a short portion of the transit; however, they are most consistent with a prograde but misaligned orbit. Ahlers et al. (2014) found a value of the impact parameter $b = 0.697$, while the parameters found by Zhou & Huang (2013) imply a value of $b = 0.7041^{+0.0073}_{-0.0090}$. Assuming these values, my tentative detection would correspond to $\lambda \sim 55 - 80°$. This is very different from the value found by Ahlers et al. (2014), but only discrepant by $1-2\sigma$ from the λ found by Zhou & Huang (2013) (Table 4.1). This tends to favor the solution found by Zhou & Huang (2013), but I cannot discard the possibility that this detection is spurious, or that the sky-projected spin-orbit misalignments measured by both Zhou & Huang (2013) and Ahlers et al. (2014) suffered from systematics that caused their values of λ to deviate from the true value, much as was the case for Kepler-13 Ab (Barnes et al. 2011; Johnson et al. 2014, and §3.1).

Given the relatively high probability that this is a spurious detection, more observations are needed to confidently detect the Doppler tomographic transit signature of KOI-368.01. Thanks to the very long transit duration and consequent slow motion of the transit signature this is achievable even with 2-4 m class telescopes such as the

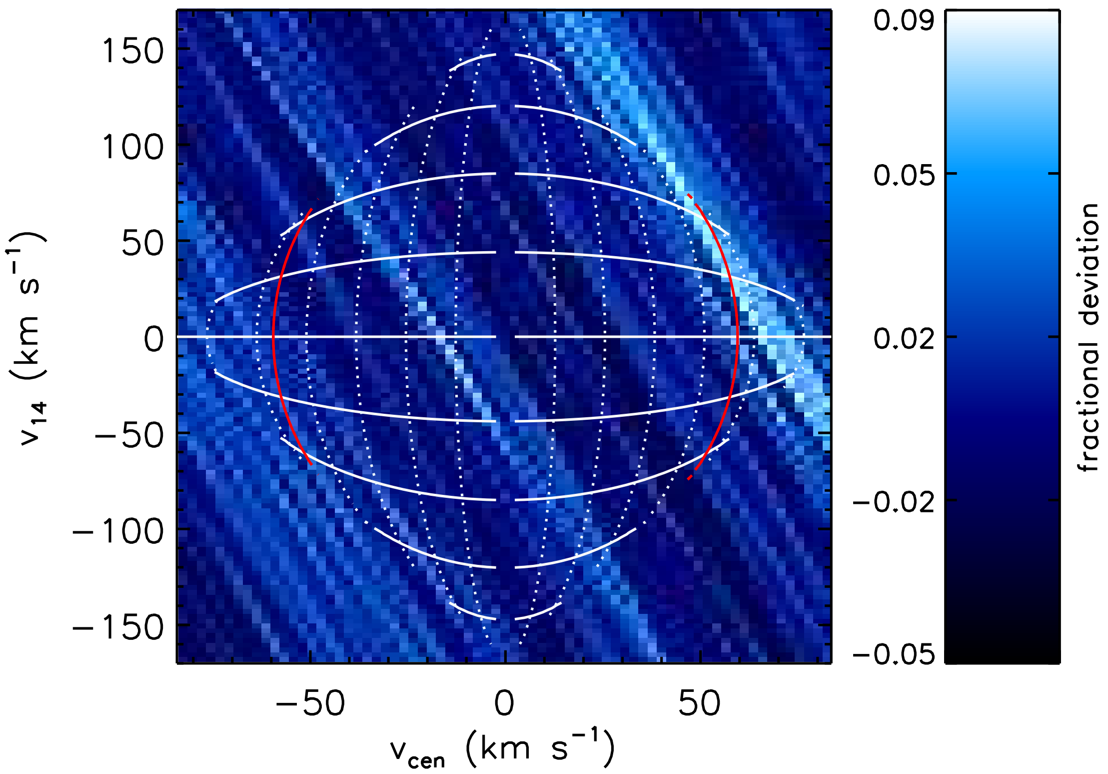

Figure 4.2 Time series line profile residuals during a partial transit of KOI-368.01, shifted and binned using the method described in §2.2.1. The bright streak at upper right is the possible detection of the transit. The solid lines show lines of constant λ, while the dotted show lines of constant b. The red contours show $b = \pm 0.7$, approximately the value found by both Zhou & Huang (2013) and Ahlers et al. (2014); the intersection of this curve and the bright streak gives the approximate range of allowed values of λ from this tentative detection. The λ contours mark, from top to bottom, $\lambda = \pm 30°, \pm 45°, \pm 60°, \pm 75°, \pm 90°, \pm 105°, \pm 120°, \pm 135°, \pm 150°$ (λ is positive on the right half of the plot, and negative on the left half). The b contours mark, from the centerline of the plot outwards, $b = 0.15, 0.30, 0.45, 0.60, 0.75, 0.9$. I note that the relationship between $(v_{\rm cen}, v_{14})$ and (λ, b) is double-valued; only one solution is shown here. The long streaks in this figure are due to the fact that my observations only covered a small portion of the transit.

HJST.

I additionally performed an MCMC fit to the average line profile for KOI-368. Using this fit, I found $v \sin i_{\star} = 81.20^{+0.43}_{-0.30}$ km s^{-1} and an intrinsic line width of $17.59^{+0.35}_{-0.39}$ km s^{-1}.

4.2 KOI-972.01

KOI-972.01 is a *Kepler* planet candidate on a 13.1-day orbit around a δ Sct variable (J. L. Christiansen, private communication; Borucki et al. 2011). Like for Kepler-448 b (§3.2), Lillo-Box et al. (2015) obtained radial velocity observations of KOI-972 using the CAFE spectrograph on the 2.2 m telescope at the Calar Alto Observatory, Spain. They obtained 51 radial velocity observations over a span of 335 days, and set an upper limit of $106.8 \pm 2.8\, M_J$ ($0.1020 \pm 0.0027\, M_{\odot}$) on the mass of KOI-972.01.

While the transit depth is rather small for a Doppler tomography target ($R_P/R_{\star} = 0.01788^{+0.00031}_{-0.00010}$; Coughlin et al. 2016), the star is very bright for a *Kepler* candidate host ($Kp = 9.275$) and is additionally the most rapidly rotating target observed for this dissertation ($v \sin i_{\star} \sim 120$ km s^{-1}). Despite the challenge, I therefore pursued Doppler tomographic observations of this target. I obtained observations during six transits of KOI-972.01 using HET/HRS, as well as one transit with HJST/TS23 (although I did not actually analyze the latter dataset); I list the complete details of the observations in Table 2.2, and the system parameters in Table 4.2.

Batalha et al. (2013) also identified a second planet candidate, KOI-972.02, around this star, with a radius of $\sim 2.5 R_{\oplus}$ and a period of 7.8 days. It has since, however, been dispositioned (*dispositioning* is the process by which a potential transiting object in the *Kepler* data is classified as a planet candidate, false positive, confirmed planet, etc.) as a false positive (Coughlin et al. 2016).

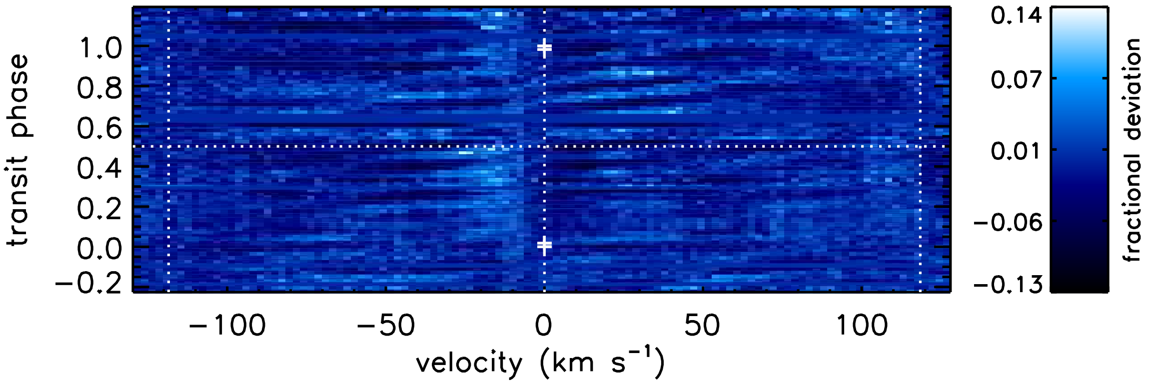

Figure 4.3 Time series line profile residuals for KOI-972.01, using only my HET data with SNR>100. The transit signature is not visible. There are still significant systematics in the time series line profile residuals–most notable the vertical feature at $-30 < v < -5$ km s^{-1}. The light and dark striations are likely non-radial pulsations of the host star, a δ Sct variable; cf. WASP-33 (Fig. 5.2).

I show the time series line profile residuals in Fig. 4.3, and the shifted and binned time series line profile residuals in Fig. 4.4. Several of my datasets had very low signal-to-noise (Table 2.2), and I excluded these in the construction of this figure. Despite the large quantity of data–more than 60 in-transit spectra with a per-pixel SNR of > 100–I was ultimately unable to detect the transit signature of KOI-972.01. There are, however, still significant systematics visible in the time series line profile residuals which complicate the detection of the transit signature. Nonetheless, this is not necessarily surprising, given that this planet candidate is much smaller and has a much smaller transit depth than any other target that I observed. I note that one transit of KOI-972.01 was also observed with the HJST and TS23 (Table 2.2), but considering that I was unable to detect the transit in the much higher signal-to-noise HET data, I do not analyze this dataset.

Despite the lack of a transit detection, I performed an MCMC fit to the average out-of-transit line profile to extract $v \sin i_\star$. Using this MCMC, I find $v \sin i_\star =$

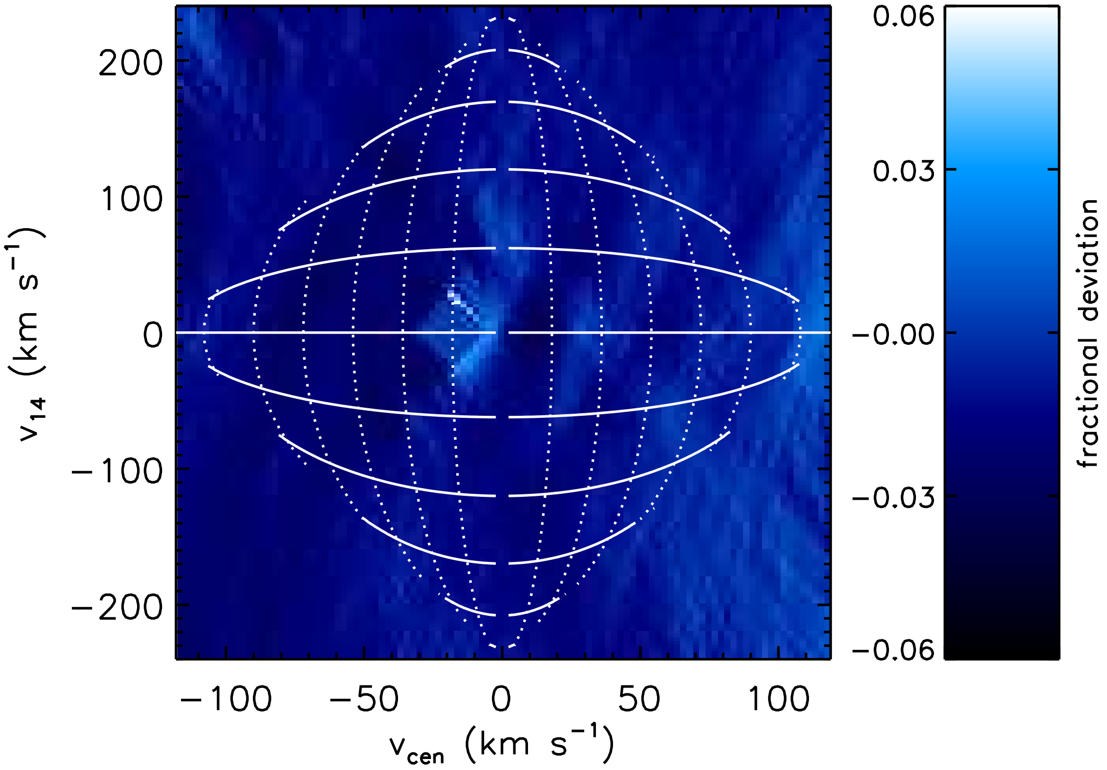

Figure 4.4 Time series line profile residuals of KOI-972.01, shifted and binned using the method described in §2.2.1. In order to create this figure I masked out the systematics at $-30 < v < -5$ km s^{-1} visible in Fig. 4.3, in order to avoid having these systematics bias the results; this results in the "hole" in this figure around $v_{\rm cen} = -20$ km s^{-1}, $v_{14} = 0$ km s^{-1}. $v_{\rm cen}$ is the velocity of the transit signature at the transit midpoint, while v_{14} is the difference between the velocity of the transit signature at egress and ingress. The solid lines show lines of constant λ, while the dotted show lines of constant b. The λ contours mark, from top to bottom, $\lambda = \pm30°, \pm45°, \pm60°, \pm75°, \pm90°, \pm105°, \pm120°, \pm135°, \pm150°$ (λ is positive on the right half of the plot, and negative on the left half). The b contours mark, from the centerline of the plot outwards, $b = 0.15, 0.30, 0.45, 0.60, 0.75, 0.9$. I note that the relationship between $(v_{\rm cen}, v_{14})$ and (λ, b) is double-valued; only one solution is shown here.

Table 4.2. System Parameters of KOI-972

Parameter	Value	Source
Stellar Parameters		
$T_{\rm eff}$ (K)	7221^{+125}_{-165}	Coughlin et al. (2016)
$\log g$ (cgs)	$3.488^{+0.231}_{-0.048}$	Coughlin et al. (2016)
$M_\star\,(M_\odot)$	$2.09^{+0.07}_{-0.31}$	Coughlin et al. (2016)
$R_\star\,(R_\odot)$	$4.24^{+0.23}_{-1.20}$	Coughlin et al. (2016)
Transit Parameters		
P (days)	$13.118966756 \pm 4.674 \times 10^{-6}$	Coughlin et al. (2016)
T_0 (BJD)	$2455094.539326 \pm 0.00025$	Coughlin et al. (2016)
$R_P/R_\star$	$0.01788^{+0.00031}_{-0.00010}$	Coughlin et al. (2016)
$a/R_\star$	23.571 ± 0.762	Coughlin et al. (2016)
b	$0.10^{+0.32}_{-0.10}$	Coughlin et al. (2016)
$M_P\,(M_J)$	$< 106.8 \pm 2.8$	Lillo-Box et al. (2015)
$R_P\,(R_J)$	$8.28^{+0.45}_{-2.35}$	Coughlin et al. (2016)
Measured Parameters		
$v \sin i_\star$ (km s^{-1})	$117.1^{+2.1}_{-1.9}$	this work
intrinsic line width (km s^{-1})	18.8 ± 1.2	this work

Note. — Uncertainties are purely statistical and do not take into account systematic sources of error. Measured parameters are those that I measured directly with the MCMC.

$117.1^{+2.1}_{-1.9}$ km s^{-1}; I quote the full results in Table 4.2.

In order to more quantitatively assess whether I detected the transit signature or not, I constructed model time series line profile residuals with parameters fixed to those of KOI-972 and KOI-972.01 from Coughlin et al. (2016), and with $v \sin i_\star$ fixed to the value that I found from fitting the average line profile. I ran a grid search over all possible values of λ and values of b, computing the reduced χ^2 value at each step. For b, Coughlin et al. (2016) found $b = 0.10^{+0.32}_{-0.10}$, and so I searched over the 1σ range of $-0.42 < b < 0.42$. In order to minimize the effects of the systematics seen in Fig. 4.3 in the range $-30 < v < -5$ km s^{-1}, I masked out this region of the time series line profile residuals. I found that the best-fit value had a goodness-of-fit measure of $\chi^2_{\rm red} = 1.47$. The corresponding goodness-of-fit parameter for fitting flat time series line profile residuals to the data (i.e., no transit signature present) is $\chi^2_{\rm red} = 1.48$. With $\Delta\chi^2_{\rm red} = 0.01$, I conclude that the transit signature model is not a significantly better fit than a null hypothesis model and thus I have not detected the transit. Due to the masking of the systematics-affected area described above, however, I would not be sensitive to the transit if $\lambda \sim -90^\circ$, $b \sim 0.15$, and thus cannot formally exclude the detection of the transit if the planet has these parameters. However, given the results of the grid search, I do not expect to have been able to detect a transit with these parameters even if the masked-out systematics did not exist.

4.3 KOI-366.01

KOI-366.01 is a *Kepler* giant planet candidate on a 75.1-day orbit around a rapidly rotating mid-F star, first announced by Batalha et al. (2013). Like Kepler-448 and KOI-972, KOI-366 was also observed by Lillo-Box et al. (2015) in their radial velocity campaign. For this target they obtained 44 observations over 73 days, and set an upper limit of $8.70 \pm 0.59 M_J$ on the mass of KOI-366.01. This suggest that, if it is not some other variety of false positive, it is indeed a planet.

Part of one transit of this object was observed with HET/HRS on 2011 August 18 UT; I list the details of the observation in Table 2.2. I show the time series line profile residuals in Fig. 4.5, and the shifted and binned data in Fig. 4.6. No hint of the transit signature is evident to the eye. In order to more quantitatively assess whether the transit signature was detected, I used the same grid search methodology as for KOI-972 in §4.2 above, fixing the parameters to those of KOI-366 and KOI-366.01 from Coughlin et al. (2016); unlike for KOI-972, b is sufficiently well determined from *Kepler* photometry that I fixed it and ran the grid search only over λ. I found that the best-fit model had $\chi^2_{\rm red} = 1.00$. The corresponding goodness-of-fit parameter for

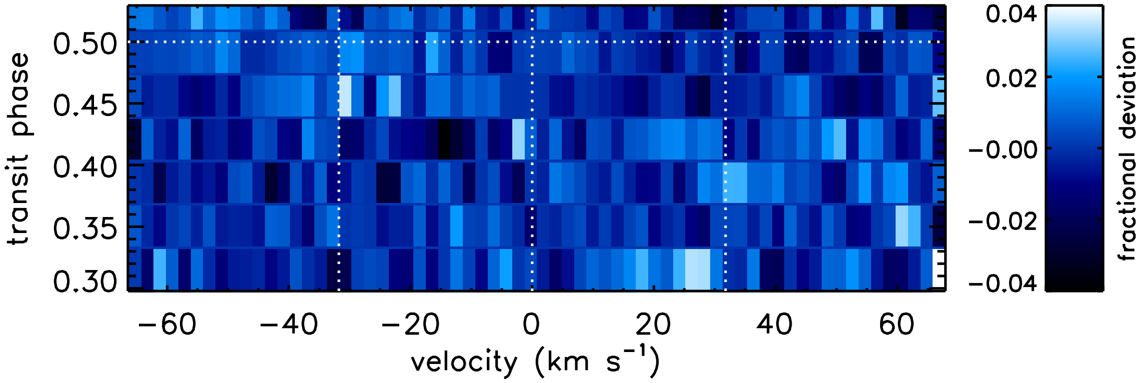

Figure 4.5 Time series line profile residuals for KOI-366.01. The transit signature is not visible, despite the high quality of the dataset (standard deviation of the continuum of 1% of the line depth).

the null hypothesis (no transit detected) is $\chi^2_{\mathrm{red}} = 1.26$, or $\Delta\chi^2_{\mathrm{red}} = 0.26$. This value of $\Delta\chi^2_{\mathrm{red}}$ is small enough that I conclude that the transit signature model is not a significantly better fit than a null hypothesis model and thus I have not detected the transit.

I also measured the $v \sin i_\star$ of KOI-366 using an MCMC fit to the average line profile. Here, I found $v \sin i_\star = 34.15^{+0.89}_{-0.83}$ km s^{-1}, as listed in Table 4.3.

Further observations, with higher signal-to-noise, are required to validate KOI-366.01 and to measure its spin-orbit misalignment; my dataset consists of only seven in-transit spectra with a mean signal-to-noise ratio of 40, preventing me from detecting the transit. Additionally, with $R_P/R_\star = 0.06361^{+0.00017}_{-0.00035}$, KOI-366.01 has a transit depth of $(R_P/R_\star)^2 \sim 0.4$ %, which is smaller than that of any of the planets where I successfully detected the transit signature.

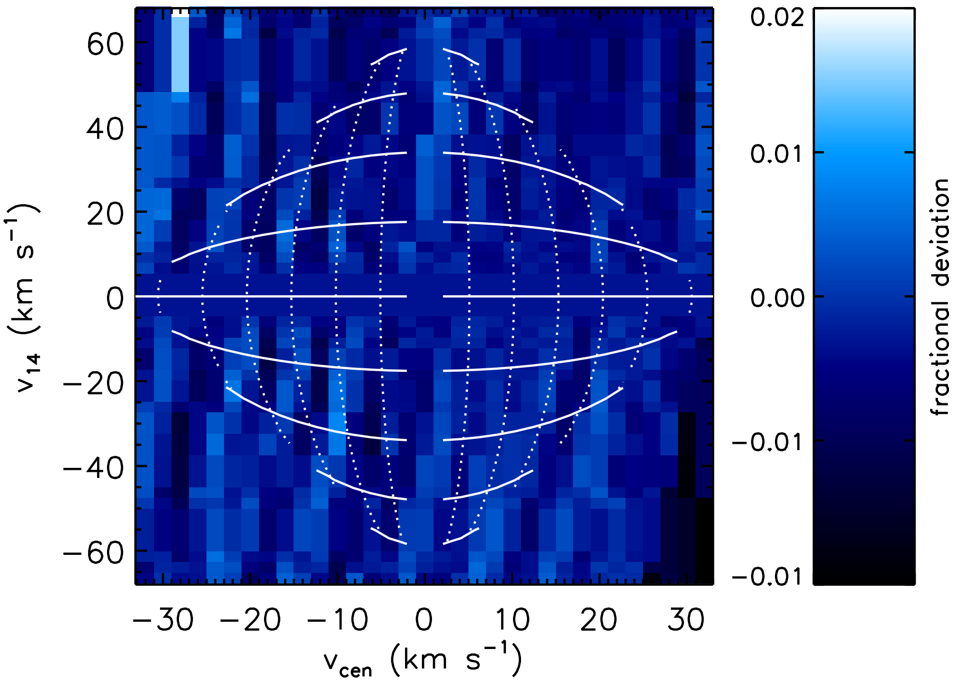

Figure 4.6 Time series line profile residuals during a partial transit of KOI-366.01 (shown in Fig. 4.5), shifted and binned using the method described in §2.2.1. No transit signature is visible. The solid lines show lines of constant λ, while the dotted show lines of constant b. The λ contours mark, from top to bottom, $\lambda = \pm 30°, \pm 45°, \pm 60°, \pm 75°, \pm 90°, \pm 105°, \pm 120°, \pm 135°, \pm 150°$ (λ is positive on the right half of the plot, and negative on the left half). The b contours mark, from the centerline of the plot outwards, $b = 0.15, 0.30, 0.45, 0.60, 0.75, 0.9$. I note that the relationship between $(v_{\rm cen}, v_{14})$ and (λ, b) is double-valued; only one solution is shown here.

Table 4.3. System Parameters of KOI-366

Parameter	Value	Source
Stellar Parameters		
$T_{\rm eff}$ (K)	6201^{+124}_{-107}	Coughlin et al. (2016)
$\log g$ (cgs)	$3.616^{+0.188}_{-0.07}$	Coughlin et al. (2016)
$M_\star\,(M_\odot)$	$1.69^{+0.17}_{-0.20}$	Coughlin et al. (2016)
$R_\star\,(R_\odot)$	$3.35^{+0.46}_{-0.79}$	Coughlin et al. (2016)
Transit Parameters		
P (days)	$75.11221874 \pm 2.468 \times 10^{-5}$	Coughlin et al. (2016)
T_0 (BJD)	$2455040.713996 \pm 0.000244$	Coughlin et al. (2016)
$R_P/R_\star$	$0.06361^{+0.00017}_{-0.00035}$	Coughlin et al. (2016)
$a/R_\star$	76.69 ± 4.1	Coughlin et al. (2016)
b	$0.8345^{+0.0038}_{-0.0074}$	Coughlin et al. (2016)
$M_P\,(M_J)$	$< 8.70 \pm 0.59$	Lillo-Box et al. (2015)
$R_P\,(R_J)$	$23.3^{+3.2}_{-5.5}$	Coughlin et al. (2016)
Measured Parameters		
$v \sin i_\star$ (km s^{-1})	$34.15^{+0.89}_{-0.83}$	this work
intrinsic line width (km s^{-1})	$8.64^{+0.65}_{-0.71}$	this work

Note. — Uncertainties are purely statistical and do not take into account systematic sources of error. Measured parameters are those that I measured directly with the MCMC.

Chapter Five: The Nodal Precession of WASP-33 b[1]

In the absence of external forces, a test particle orbiting a spherical star will keep orbiting on the same plane forever. In the real world, however, stars are not perfectly spherical, planets are not test masses, and external forces are not always negligible. One of the consequences of this is that orbits are not fixed relative to the star's inertial rest frame–they precess. In general, there are two types of orbital precession: apsidal precession, where the longitude of periastron of an eccentric orbit precesses; and nodal precession, where the longitude of the ascending node of an inclined orbit precesses.

Nodal precession is generally caused by non-sphericity of the host star (although there are also smaller contributions from general relativity and other sources; e.g., Iorio 2011). One consequence of the fact that stars rotate is that they are dynamically oblate–the equatorial radius is slightly larger than the polar radius (which, in extreme cases, causes the stellar gravity darkening discussed in §1.1.1). Our own Sun is dynamically oblate, but the rapidly rotating stars discussed in this dissertation display a much higher degree of oblateness. As a planet orbits an oblate star on an inclined orbit (i.e., it has a large spin-orbit misalignment), the additional mass

---

[1] The work described in this chapter was originally published as Johnson, M. C., Cochran, W. D., Collier Cameron, A., & Bayliss, D. 2015, ApJL, 810, 23. An erratum was subsequently published as Johnson, M. C., Cochran, W. D., Collier Cameron, A., & Bayliss, D. 2015, ApJL, 812, 17. Author contributions: M.C.J. performed all of the analysis and wrote the paper. W.D.C. observed the 2014 transit, reduced the spectroscopic data, and discussed methodology and results. A.C.C. suggested that the project should be undertaken and consulted on results. D.B. assisted with scheduling the LCOGT observations and analysis of these data. M.C.J. also acknowledges L. Iorio and K. Rice for pointing out errors in the original versions of Eqn. 5.3 and the calculation of J_2, respectively.

around the bulging stellar equator exerts a gravitational force on the planet. Due to conservation of angular momentum (of the full planet plus star system), this results in a torque on the orbit, and the orbit precesses while maintaining the same inclination. Equivalently, an oblate star possesses a significant gravitational quadrupole moment, resulting in non-Keplerian motion of the orbiting planet.

Measurement of the nodal precession of an exoplanet can thus be used to back out the stellar gravitational quadrupole moment (denoted J_2). This quantity is generally affected by the internal structure of the star, and so may be used as a direct probe of models of stellar structure.

WASP-33 b is a hot Jupiter orbiting a relatively massive ($1.5\,M_\odot$), rapidly rotating ($v \sin i_\star = 85.6$ km s^{-1}) star (Collier Cameron et al. 2010b). It is notable for being one of the hottest planet host stars known ($T_{\rm eff} = 7430$ K), and the first transiting planet to be confirmed with Doppler tomography. Using their Doppler tomographic observations of WASP-33 b, Collier Cameron et al. (2010b) measured a sky-projected spin-orbit misalignment of $\lambda = -105.8^\circ \pm 1.2^\circ$ (using their dataset from McDonald Observatory). They also found an orbital period of $P = 1.2198669 \pm 0.0000012$ days. I summarize the parameters of the WASP-33 system from the literature in Table 5.1.

Since WASP-33 b is on a highly inclined, short-period orbit about a rapidly rotating (and therefore likely dynamically oblate) star, Iorio (2011) estimated that the orbital nodes should precess at a rate of $d\Omega/dt \leq 8.2 \times 10^{-10}$ s^{-1} ($\leq 1.5^\circ$ yr^{-1}). They predicted that this would result in a changing transit duration that would be detectable in ~ 10 years. Such a measurement will be challenging, however, as WASP-33 is a δ Sct variable (Herrero et al. 2011). The stellar non-radial pulsations cause distortions in the transit light curve, which could induce systematic errors in the measurement of the transit duration. This change in the transit duration, how-

Table 5.1. Parameters of WASP-33 from the Literature

Parameter	Value	Source
Stellar Parameters		
$T_{\rm eff}$ (K)	7430 ± 100	Collier Cameron et al. (2010b)
$M_\star\,(M_\odot)$	1.495 ± 0.031	Collier Cameron et al. (2010b)
$R_\star\,(R_\odot)$	1.444 ± 0.034	Collier Cameron et al. (2010b)
Planetary Parameters		
$M_P\,(M_J)$	2.1 ± 0.2	Lehmann et al. (2015)
$R_P\,(R_J)$	1.497 ± 0.045	Collier Cameron et al. (2010b)
b	0.176 ± 0.010	Collier Cameron et al. (2010b)
MCMC Inputs		
P (days)	1.2198709 ± 0.0000007	Kovács et al. (2013)
T_0 (BJD)[a]	2452950.6731 ± 0.0015	Kovács et al. (2013)
$R_P/R_\star$	0.1143 ± 0.0002	Kovács et al. (2013)
$a/R_\star$	3.69 ± 0.01	Kovács et al. (2013)

Note. — The parameters in the MCMC Inputs section were MCMC parameters on which I put Gaussian priors using the best-fit parameter and uncertainty from Kovács et al. (2013).

[a] Quoted in HJD by Kovács et al. (2013), and converted to BJD using the `hjd2bjd` IDL code (Eastman et al. 2010, or http://astroutils.astronomy.ohio-state.edu/time/hjd2bjd.html).

ever, is caused by the changing impact parameter b, which can be more accurately measured using Doppler tomography than from the transit lightcurve. For instance, Collier Cameron et al. (2010b) measured the impact parameter of WASP-33 b to be $b = 0.176 \pm 0.010$ using their spectroscopic data and $b = 0.155^{+0.100}_{-0.120}$ using their photometric data.

The movement of the line profile perturbation across the stellar line profile during the transit maps directly to the path of the planet across the stellar disk, allowing me to measure the location and orientation of the transit chord relative to the projected stellar rotation axis. Precession changes this path, allowing nodal precession to be measured using Doppler tomography.

It has now been several years since the Doppler tomographic observations presented by Collier Cameron et al. (2010b) were obtained. This offers a sufficient time baseline to allow the detection of the movement of the transit chord due to nodal precession. Thus, a second epoch of Doppler tomographic observations were collected, and I have detected the changing transit chord.

Orbital precession has previously been detected for Kepler-13 Ab by Szabó et al. (2012), who measured a rate of change of the impact parameter of $db/dt = -0.016 \pm 0.004$ yr^{-1} using the changing transit duration in *Kepler* photometry. Like WASP-33 b, Kepler-13 Ab is a hot Jupiter orbiting a rapidly rotating star on an inclined orbit (see §3.1). WASP-33 b, however, has a more highly inclined, shorter period orbit than Kepler-13 Ab, and so it might be qualitatively expected to show a larger precession rate than Kepler-13 Ab. Barnes et al. (2013) proposed a large rate of nodal precession for the young hot Jupiter candidate PTFO 8-8695 b (van Eyken et al. 2012) to explain the time-variable transit shape of this object, but the planetary nature of this object is controversial (Ciardi et al. 2015; Yu et al. 2015; Kamiaka et al. 2015; Howarth 2016; Raetz et al. 2016; Johns-Krull et al. 2016). Orbital precession has also previously been measured for several circumbinary planets (e.g., Kostov et al. 2014); in this case the precession is caused by large gravitational perturbations due to the inclination of the planetary orbit with respect to the binary orbital plane. My measurement of the orbital precession of WASP-33 b is thus the second such measurement for a confirmed exoplanet orbiting a single star.

Collier Cameron et al. (2010b) observed one transit of WASP-33 b with the HJST and TS23 on 2008 November 12 UT, and I reanalyzed these data. They also observed two other transits with other facilities, but I did not reanalyze these data. A second transit was observed with the HJST on 2014 October 4 UT, 2,152 days (1,764 planetary orbits) after the first dataset. The exposure length was 900 seconds for both datasets. 13 spectra were obtained in 2008 and 21 in 2014; 10 spectra in each dataset were taken during the transit. Thanks to WASP-33's brightness ($V = 8.3$) I was able to obtain very high quality line profiles; the standard deviation of the continuum was 0.010 of the depth of the line profile for the 2008 observations and 0.0078 for the 2014 dataset.

Deviation of the observed transit midpoint from that expected based on the published ephemeris could masquerade as a change of the transit chord in the Doppler tomographic data. Due to its relatively poor time resolution (900 second exposure lengths), the time of transit was not well constrained by the spectroscopic data alone. In order to better constrain the transit epoch in my 2014 spectroscopic data I simultaneously obtained photometry of WASP-33 using the Las Cumbres Observatory Global Telescope Network (LCOGT; Brown et al. 2013) 1 m telescope and SBIG camera at McDonald Observatory.

I observed in the Sloan i' band, and defocused the telescope in order to reduce the effects of inter-pixel variations and avoid saturating on this bright star. This dataset consists of 700 images, each with an exposure length of 15 seconds. The initial data reductions (e.g., flat and bias correction) were performed automatically by the LCOGT pipeline. I used the `astrometry.net` code (Lang et al. 2010) to register all images, and then performed aperture photometry on WASP-33 and three reference stars using the IDL task `APER`. I calculated the formal uncertainty on each data point incorporating the uncertainty from `APER` (based upon photon-counting noise and uncertainty in the sky background), as well as an estimated contribution from the calibration frames and from scintillation noise (Young 1967).

In order to analyze my photometric and tomographic data on WASP-33 b, I needed to have some method to minimize the impact of the δ Sct non-radial pulsations on the analysis, as these cause both photometric variability and features in the time series line profile residuals. Either could, if not handled properly, bias the results and perhaps even result in a false detection of precession. I mitigated the impact of the pulsations by treating the photometric and tomographic data with Gaussian process regression and a two-dimensional Fourier filter, respectively. I will describe these methodologies in the next section.

5.1 Methodology for WASP-33

5.1.1 Gaussian Process Regression

A methodology that has been gaining widespread acceptance in the literature for dealing with stellar photometric variability is *Gaussian process regression.* Essentially, this method fits a non-parametric model of the noise along with the model of the expected signal (in my case, the transit light curve model). In addition to the usual MCMC jump parameters (P, λ, etc.), a number of *hyperparameters* are included and specify the properties of the non-parametric model.

Gaussian process regression rests upon the assumption of some form for the covariance matrix K, detailing the relationship between each pair of measurements in the dataset. This form, or kernel, governs the response of the Gaussian process to the input data. Various forms of the kernel are used, depending upon the expected nature of the noise or variability that is being fit. For the analysis of the transit light curve of WASP-33 b, I used a Matern 3/2 kernel. With this kernel, each element of the covariance matrix is

$$k_{ij} = \alpha^2\left(1 + \frac{\sqrt{3}|t_i - t_j|}{l}\right)\exp\left(-\frac{\sqrt{3}|t_i - t_j|}{l}\right) + \delta_{ij}\sigma_i^2 \tag{5.1}$$

where i, j denote two of the photometric observations, t_i, t_j are the times at which observations i, j were obtained, σ_i is the formal uncertainty on datapoint i, and α and l are hyperparameters describing the amplitude and timescale of the stellar variability, respectively.

The Gaussian process model of the stellar variability may then be obtained as

$$\mathbf{m}_* = \boldsymbol{\mu}(t_*) + \mathbf{K}(t, t_*)\mathbf{K}(t, t)^{-1}(\mathbf{y}(t) - \boldsymbol{\mu}(t)) \tag{5.2}$$

(this is Eqn. 3.8 of Roberts et al. 2013, with the terminology modified slightly to match the nomenclature used in this dissertation), where t denotes the times of each observation; t_* the times at which I wish to compute the model; $\mathbf{m}_*$ is a vector containing the Gaussian process model; $\boldsymbol{\mu}(t)$, $\boldsymbol{\mu}(t_*)$ are vectors containing the transit lightcurve model at t and t_*, respectively; $\mathbf{K}$ is the covariance matrix computed according to Eqn. 5.1; and $\mathbf{y}(t)$ is a vector containing the photometric data.

I produced a model of the transit lightcurve using the JKTEBOP package[2] (e.g., Southworth 2011), and explored the likelihood space of model fits to the data using an MCMC derived from that used for my work on Kepler-13 (§3.1). The MCMC used eight parameters: b, $R_P/R_\star$, $a/R_\star$, α, l, the epoch of transit center T_0, and two quadratic limb darkening parameters. I set Gaussian priors upon $R_P/R_\star$ and $a/R_\star$, using the best-fit values and uncertainties found by Kovács et al. (2013) as the center and width of the priors, respectively. I also set priors upon the limb-darkening parameters, using JKTLD[3] to find the expected limb darkening values from ATLAS

---

[2] http://www.astro.keele.ac.uk/jkt/codes/jktebop.html

[3] http://www.astro.keele.ac.uk/jkt/codes/jktld.html

model atmospheres from Claret (2004) at the stellar parameters of WASP-33 from Collier Cameron et al. (2010b), and transformed these into the triangular sampling space of Kipping (2013).

5.1.2 Fourier Filtering

Doppler tomography is most effective for stars with $20\ \mathrm{km\ s^{-1}} < v \sin i_\star < 120\ \mathrm{km\ s^{-1}}$, and most stars showing these characteristics are main sequence A and early F stars. This range of spectral types, however, is also where the main sequence intersects the instability strip, and many of these stars are therefore photometric variables (δ Sct and/or γ Dor variables). Both of these classes of variables owe their variability to non-radial pulsations of the stellar surface. These non-radial pulsations also make an imprint upon the stellar line profiles, and can obscure the Doppler tomographic signature of a planet transiting the star. It is therefore desirable to develop a methodology to filter out the stellar pulsations, leaving only the planetary transit signature.

In the case of WASP-33 b, I can mitigate the effects of the pulsations by exploiting the fact that the pulsations propagate in the prograde direction, whereas the planetary orbit is retrograde ($|\lambda| > 90^\circ$). The frequency components due to the pulsations and the planetary transit thus tend to be separated in the two-dimensional Fourier transform of the time series line profile residuals.

I can construct a Fourier filter by multiplying each complex element of the Fourier transform by unity if that element was in a region where there is power only from the transit signature, and zero if the element is in a region with significant power from the pulsations, with a Hann function transition between the two regimes in order to avoid ringing due to a sharp edge. I then perform an inverse Fourier transform on this filtered Fourier spectrum. In the case of WASP-33 b this successfully removed most of the effects of the pulsations. For best results I had to filter out low-frequency modes where there was power from both the pulsations and the transit; however, the high-frequency components were sufficient to reconstruct most of the transit signature.

I obtained best-fit values of the transit parameters using an MCMC as implemented by `emcee` (Foreman-Mackey et al. 2013). I performed a joint fit to the Fourier-filtered time series line profile residuals from both 2008 and 2014, as well as a single spectral line, the latter in order to measure the $v \sin i_\star$ of WASP-33. For the single line I fit a rotationally broadened line profile to the Ba II line at 6141.7 Å (the same line as I used for Kepler-13 in §3.1), chosen because it is deep but unblended and unsaturated. In order to minimize the impact of the line profile variations I stacked all of the 2008 spectra. I did not utilize the 2014 dataset because I could not obtain a good fit to the Ba II line. For the time series line profile residuals I fit a transit model computed with my modeling code and passed through the same Fourier filter as the data. The MCMC had sixteen parameters: λ, b, and the transit epoch T_0 at the two epochs, $v \sin i_\star$, $R_P/R_\star$, $a/R_\star$, P, four quadratic limb darkening parameters (two each for the single-line and the time series line profile residual data), the intrinsic Gaussian line width, and a velocity offset between the single line data and the rest frame. I assumed that all parameters except T_0, λ and b remained constant between 2008 and 2014. I calculated T_0 for 2008 from the epoch and period given by Kovács et al. (2013), while the 2014 transit epoch was taken from the simultaneous photometric observations of that transit described above. I set Gaussian priors upon $R_P/R_\star$, $a/R_\star$, P, and the 2008 T_0, and set the prior value and width to the parameter value and uncertainty, respectively, found by Kovács et al. (2013), while the prior value and width for the 2014 T_0 were taken from my photometric observations. I used a set of 100 walkers, ran each one for 1000 steps, and cut off the first 500 steps of convergence and burn-in, resulting in 50,000 samples from the posterior distribution.

5.2 Results on WASP-33

I show the LCOGT lightcurve in Fig. 5.1. I found a best-fit time of transit center of $T_0 = 2456934.77146 \pm 0.00059$ BJD. This is 12.3 minutes later than predicted by the ephemeris of Collier Cameron et al. (2010b), but is in agreement with that predicted by that of Kovács et al. (2013).

I show the time series line profile residuals, both filtered and unfiltered, along with the Fourier spectra and filters, in Fig. 5.2. For illustrative purposes I also shifted and binned these data (after Fourier filtering), which I show in Fig. 5.3; I did not use the shifted and binned data for my analysis.

I give the best-fit values of the model parameters in Table 5.2. I found that both the impact parameter and the spin-orbit misalignment have changed between the two epochs: I measured $b = 0.218^{+0.011}_{-0.029}$ and $\lambda = -110.06^{+0.40}_{-0.47}$ ° in 2008, and $b = 0.0840^{+0.0020}_{-0.0019}$ and $\lambda = -112.93^{+0.23}_{-0.21}$ ° in 2014. My uncertainties on these values are rather small (cf. Collier Cameron et al. 2010b, whose uncertainties on λ and b are $\sim 2-5$ times the size of mine). They did not remove the stellar pulsations from their data, and so it is perhaps not unexpected that I can obtain a more precise result. There may, however, be sources of systematic errors which were not taken into account in my calculation of the uncertainties. The values of λ and b that I obtained from the 2008 data disagree with those found by Collier Cameron et al. (2010b) by 3.4σ and 1.3σ, respectively, but agree with another of their Doppler tomographic datasets to within 1.2σ. Most likely this results from differing treatments of the stellar pulsations. Additionally, my posterior distribution for b in 2008 is double-peaked, resulting in asymmetric uncertainties on this parameter.

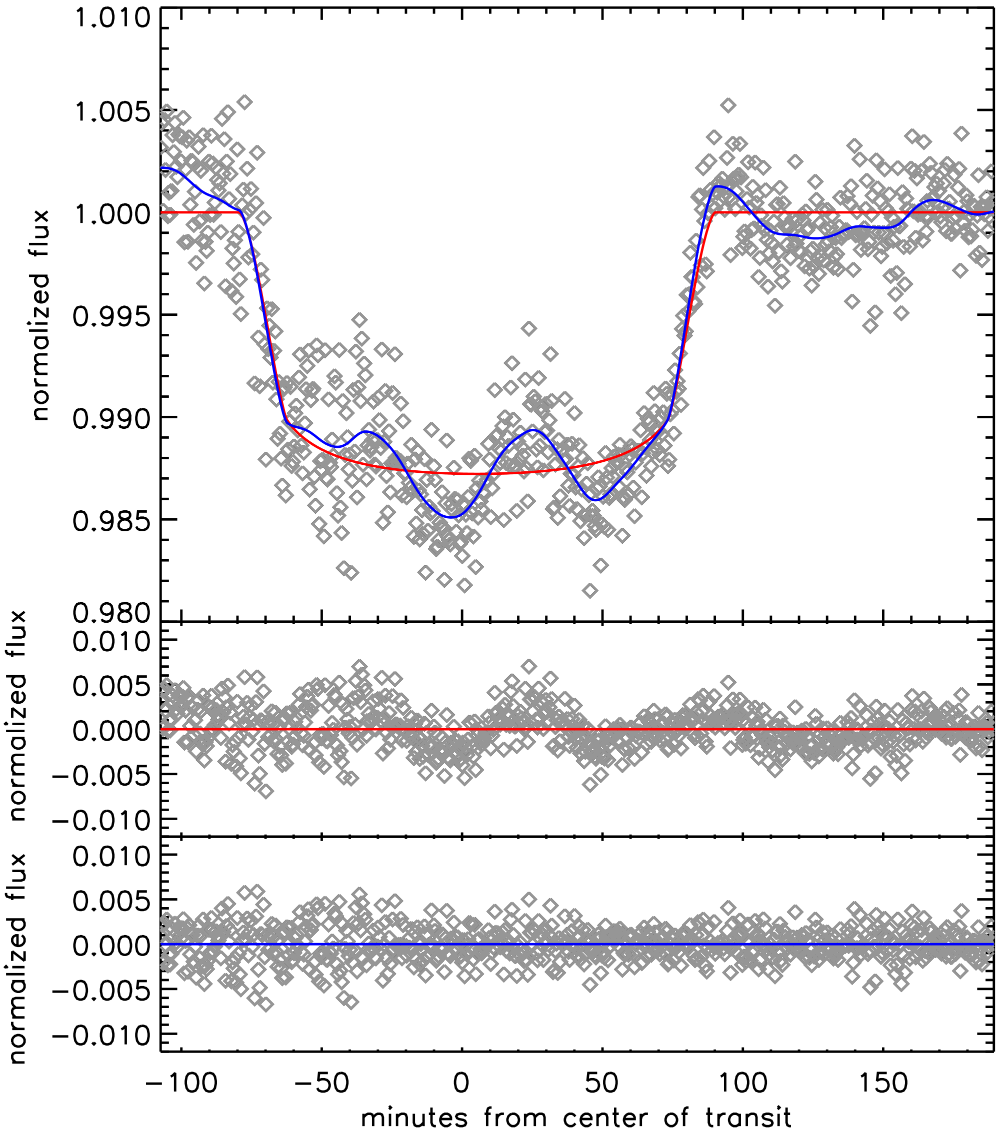

Figure 5.1 Top: LCOGT lightcurve of the transit of WASP-33 b on 2014 October 4 UT. I show the data in gray, with the best-fit transit model in red and the best-fit transit plus Gaussian process model in blue. Middle: residuals with the best-fit transit model subtracted, showing the stellar variability. Bottom: residuals with the best-fit transit plus Gaussian process model subtracted, showing the power of the Gaussian process to model and remove the stellar variability. The varying scatter about the best-fit model over the course of the observations is due to changing airmass.

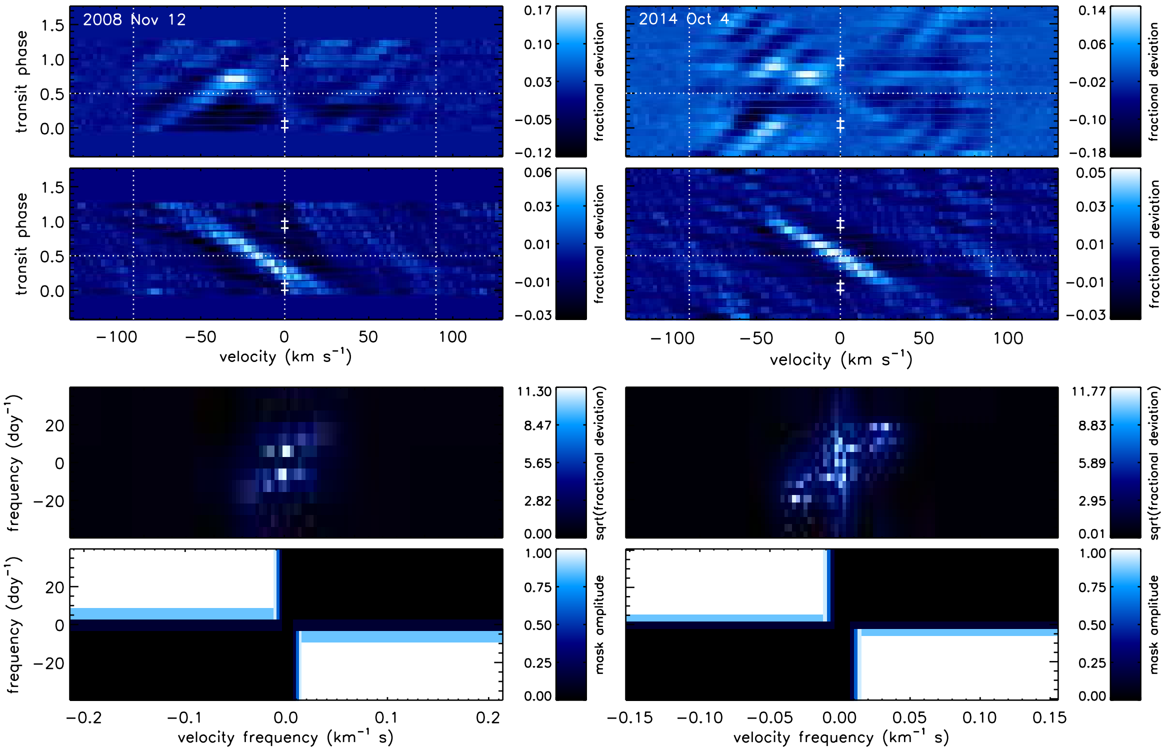

Figure 5.2 Times series line profile residuals and Fourier filters for WASP-33 b. The left and right columns show the 2008 and 2014 datasets, respectively. Top row: raw time series line profile residuals. Second row: these data after application of the Fourier filter. The transit signature is the bright streak running from bottom center towards the upper left. The time range depicted is the same for all plots; flat blue areas indicate regions where I do not have any observations. Most of the remaining anomalous structure in the filtered datasets is ringing due to the filter. The transit signature has shifted noticeably to the right between the 2008 and 2014 epochs. Third row: two-dimensional Fourier transforms of the time series line profile residuals, shown with a square-root color scale to best display the frequency structure. The transit signature is the narrow structure running from upper left to lower right. Bottom row: masks used to Fourier filter the time series line profile residuals.

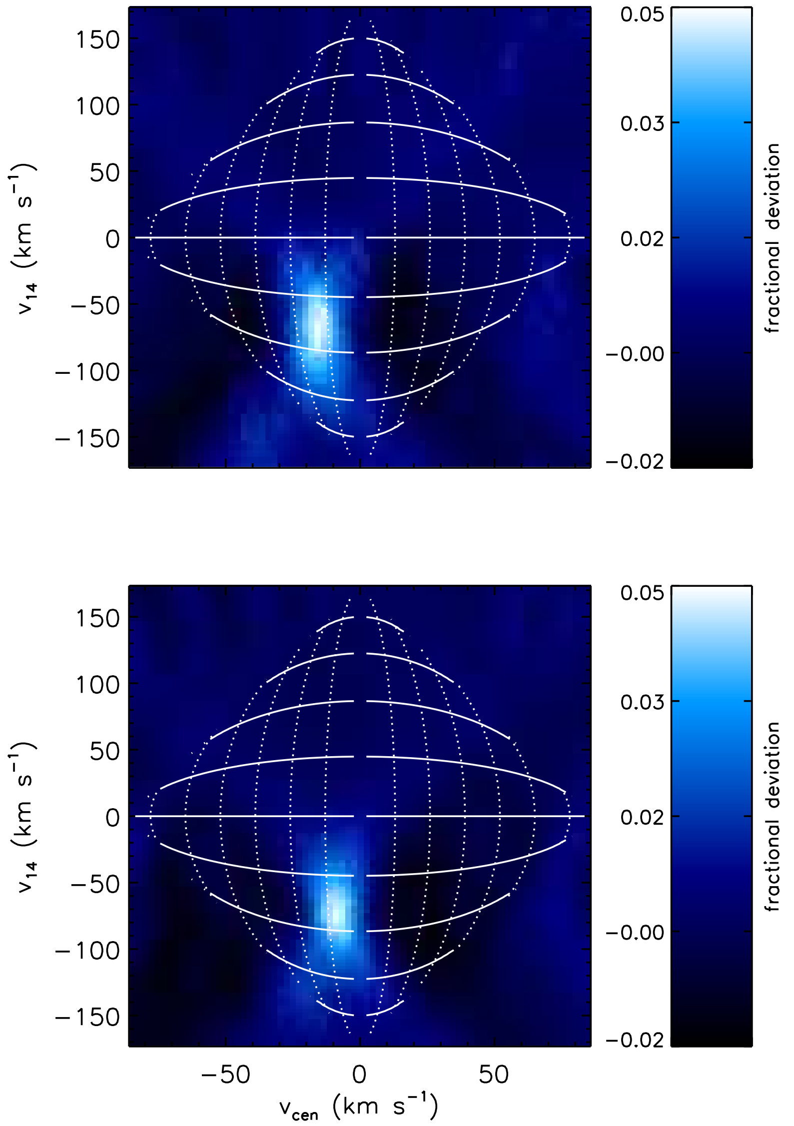

Figure 5.3 Shifted and binned time series line profile residuals for WASP-33 b, after the Fourier filter has been applied. The 2008 transit is shown in the top panel, and the 2014 transit in the bottom panel. Note the movement of the bright spot denoting the best-fit transit parameters, showing the precession of WASP-33 b. The solid lines show lines of constant λ, while the dotted lines show lines of constant b. The λ contours mark, from top to bottom, $\lambda = \pm30°, \pm45°, \pm60°, \pm75°, \pm90°, \pm105°, \pm120°, \pm135°, \pm150°$ (λ is positive on the right half of the plot, and negative on the left half). The b contours mark, from the centerline of the plot outwards, $b = 0.15, 0.30, 0.45, 0.60, 0.75, 0.9$. I note that the relationship between $(v_{\rm cen}, v_{14})$ and (λ, b) is double-valued; only the solution appropriate to WASP-33 b is shown here.

Table 5.2. Results for WASP-33

Parameter	2008	2014
Measured Parameters		
T_0 (BJD)	...	$2456934.77146 \pm 0.00059$
b	$0.218^{+0.011}_{-0.029}$	$0.0840^{+0.0020}_{-0.0019}$
λ (°)	$-110.06^{+0.40}_{-0.47}$	$-112.93^{+0.23}_{-0.21}$
$v \sin i_\star$ (km s^{-1})	$86.63^{+0.37}_{-0.32}$	...
α	...	0.00173 ± 0.00082
l (minutes)	...	20.7 ± 9.2
Calculated Parameters		
i_P (°)	$86.61^{+0.46}_{-0.17}$	$88.695^{+0.031}_{-0.029}$
Ω (°)	$86.39^{+0.49}_{-0.18}$	$88.584^{+0.034}_{-0.032}$
τ_{14} (days)	$0.11694^{+0.00073}_{-0.00041}$	0.11880 ± 0.00033

Note. — Uncertainties are purely statistical and do not take into account systematic sources of error. The values in the Measured Parameters section are measured directly from the MCMC, while those in the Calculated Parameters section are calculated analytically based upon the results of the MCMC and the parameters from the literature listed in Table 5.1. τ_{14} is the transit duration.

Although I did not measure the transit duration directly from my data, I calculated the expected duration using Eqn. 3 of Seager & Mallén-Ornelas (2003); this is shown in Table 5.2. The transit duration implied by my Doppler tomographic measurements has changed by 2.7 minutes between the two epochs, a challenging measurement for typical ground-based data, even without the complication of stellar variability.

Using my values of b and λ at the two epochs, I calculated the rate of precession. I used the definition of the argument of the ascending node Ω as given by Queloz et al. (2000), i.e., the angle between the plane of the sky and the intersection between the planetary orbital plane and a plane parallel to the line of sight which is also perpendicular to the projection of the stellar rotation axis onto the plane of the sky, as measured in this latter plane. See Fig. 2 of Queloz et al. (2000) for a graphical definition; note that the quantity they denoted as Δ is my b, their i is my $i_\star$, and that their α is *not* the same as λ–α is the angle between the planetary orbital angular momentum vector and the sky projection of the stellar rotational angular momentum vector (λ is the angle between the sky projections of both vectors). Using this definition of Ω and the definition of the impact parameter, $b = a/R_\star \cos i_P$, I related Ω to my known quantities with

$$\tan\Omega = -\sin\lambda \tan i_P \tag{5.3}$$

which I used to calculate Ω at the two epochs. I assumed that $a/R_\star$ remains constant. I found $db/dt = -0.0228^{+0.0050}_{-0.0018}$ yr^{-1} and $d\lambda/dt = -0.487^{+0.089}_{-0.076}$ ° yr^{-1}, and calculated a rate of nodal precession of WASP-33 b of $d\Omega/dt = 0.373^{+0.031}_{-0.083}$ ° yr^{-1}. The direction of precession is prograde, as required by the retrograde orbit of WASP-33 b. My result is in agreement with the prediction of Iorio (2011), $d\Omega/dt \leq 1.5^\circ$ yr^{-1}. I show a schematic view of the changing transit chord in Fig. 5.4.

The observation that both b and λ are changing implies that the total angular momentum vector of the system $\mathbf{L}_{\rm tot}$ (the sum of the stellar spin and planetary orbital momentum vectors), about which the planetary orbital angular momentum is precessing, is neither close to perpendicular nor close to parallel to the line of sight. Consider two limiting cases: if $\mathbf{L}_{\rm tot}$ were perpendicular to the line of sight, then the precession would manifest as purely a change in b, whereas if $\mathbf{L}_{\rm tot}$ were parallel to the line of sight, the precession would manifest as purely a change in λ. Intermediate motion implies an intermediate angle.

Using the rate of precession I set limits on the stellar gravitational quadrupole

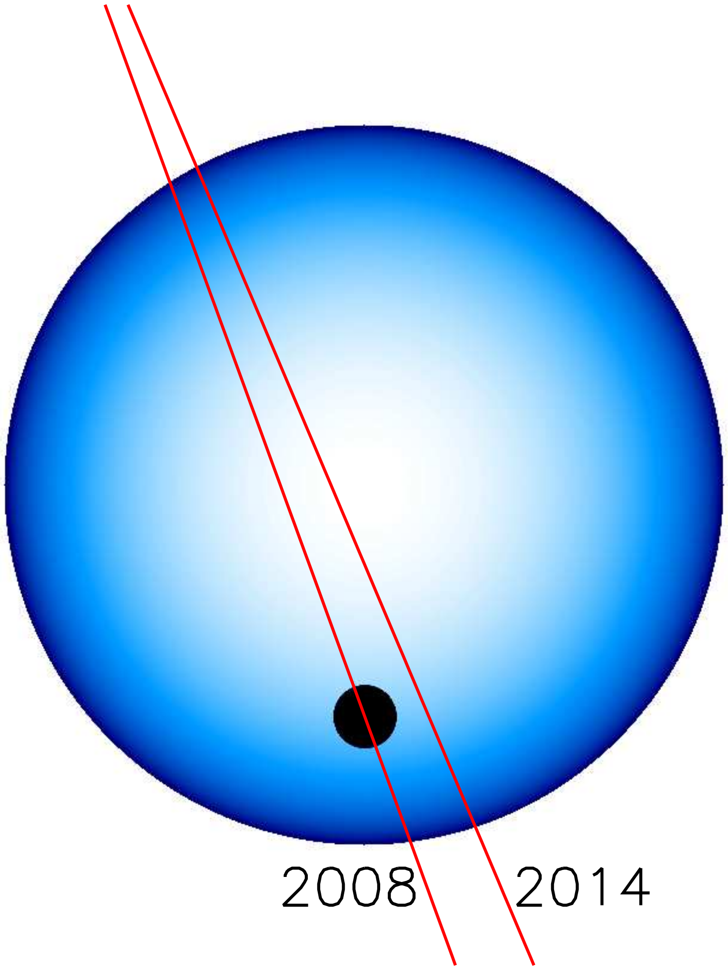

Figure 5.4 Schematic showing the transit chord crossing WASP-33 at the 2008 and 2014 epochs. The stellar rotation axis is vertical, and the north pole is at the top, such that star rotates from left to right. The planet moves along the red lines from bottom to top. I show the silhouette of the planet for a 2008 transit. The limb darkening shown on the star corresponds to that for my best-fit Doppler tomographic solution. I do not depict surface brightness variations due to the stellar pulsations.

moment J_2. This is

$$J_2 = -\frac{d\Omega}{dt}\frac{P}{3\pi}\left(\frac{a}{R_\star}\right)^2 \sec\psi \tag{5.4}$$

(e.g, from rearranging Eqn. 10 of Barnes et al. 2013). The full three-dimensional spin-orbit misalignment ψ can be expressed as (from Eqn. 25 of Iorio 2011),

$$\cos\psi = \cos i_\star \cos i_P + \sin i_\star \sin i_P \cos\lambda \tag{5.5}$$

and, while I do not know $i_\star$ or ψ, following Iorio (2011) I can set limits on these quantities, since I know λ and i_P and can set limits on $i_\star$. By requiring that WASP-33 rotate at less than the breakup velocity, and using the stellar parameters found by Collier Cameron et al. (2010b), Iorio (2011) set limits of $11.22^\circ \leq i_\star \leq 168.77^\circ$. Along with my values of i_P and λ, this implies a 1σ range of $93.06^\circ \leq \psi \leq 110.33^\circ$. Thus, I set limits of $9.4 \times 10^{-5} < J_2 < 6.1 \times 10^{-4}$. For comparison, the Solar value is $J_2 \sim 2 \times 10^{-7}$ (e.g., Roxburgh 2001).

After I published my measurement of the nodal precession of WASP-33 b (Johnson et al. 2015), Iorio (2016) were able to use my measurements to better constrain the system parameters of WASP-33. They were able to infer the stellar inclination $i_\star$, obtaining $i_\star = 142^{+10\circ}_{-11}$, and, consequently, $\psi = 99^{+5\circ}_{-4}$ in 2008 and $\psi = 103^{+5\circ}_{-4}$ in 2014. They used this to better constrain J_2, finding $J_2 = (2.1^{+0.8}_{-0.5}) \times 10^{-4}$, which is several times higher than the upper limit that I found.

The rate of change of the ascending node implies that WASP-33 b began transiting its host star as viewed from the Earth in 1974^{+8}_{-3}, and will transit until 2062^{+4}_{-10}; the precession period is $\sim 3,100$ years.

Chapter Six: Conclusions

Doppler tomography is one of the few methods that can validate transiting planet candidates around rapidly rotating stars, and measure their spin-orbit misalignments. In this dissertation I have developed a new suite of tools to reduce and analyze Doppler tomographic data, and applied it to a large set of data, mostly obtained at McDonald Observatory, on several transiting planets and planet candidates.

I was able to successfully measure the spin-orbit misalignment of the hot Jupiter Kepler-13 Ab, a particularly challenging measurement due to the superimposed, moving secondary line profile of the binary companion Kepler-13 B. I also measured the spin-orbit misalignments of the hot Jupiters HAT-P-41 b and WASP-79 b, and the warm Jupiter Kepler-448 b, but a detection of the transit of KELT-2 Ab eluded me. Kepler-13 Ab has a misaligned but prograde orbit; Kepler-448 b is well-aligned; WASP-79 b has a highly inclined, nearly polar orbit; and I found two degenerate solutions for HAT-P-41 b, both implying a prograde orbit but with either a mild or a large misalignment. I also used my best-fit solution for WASP-79 to suggest that, of the two compatible solutions for the system presented by Smalley et al. (2012), the main sequence solution is likely to be the correct one.

I also attempted to use my Doppler tomographic data to validate several *Kepler* planet candidates, KOI-366.01, KOI-368.01, and KOI-972.01. Unfortunately I was unable to detect the transits of KOI-972.01 and KOI-366.01, although this is not entirely unsurprising considering that these planet candidates have much smaller transit depths than any of those that I successfully detected. I achieved a tentative ($\sim 2\sigma$) detection of the transit signature of KOI-368.01 by utilizing my shifting and binning method (described in §2.2.1), but further observations are needed to confidently detect the transit signature and measure the spin-orbit misalignment.

Finally, I used Doppler tomography to detect and measure the nodal precession of the highly inclined hot Jupiter WASP-33 b, finding $d\Omega/dt = 0.373^{+0.031}_{-0.083}$ ° yr^{-1}. This is only the second time that precession has been measured for a confirmed exoplanet transiting a single star. I also used the precession rate to constrain the stellar gravitational quadrupole moment J_2, finding $9.4 \times 10^{-5} < J_2 < 6.1 \times 10^{-4}$.

In Table 6.1 I summarize the results from this dissertation–measurements of λ, b, and $v \sin i_\star$ for the systems that I have analyzed. I also show my results for λ and b graphically, for the systems where I have at least a tentative detection of the transit signature, in Fig. 6.1.

6.1 Future Prospects

Doppler tomography has seen limited utility thus far in part because most known transiting exoplanet host stars are rather faint ($V > 10$), and thus require highly competitive 8-10 m class telescope time for observations. The planet hosts found by the SuperWASP and HATNet projects typically have $V \sim 10-12$, while *Kepler* planet hosts are typically even fainter, often with $V > 13$, rendering Doppler tomographic observations even with the largest existing telescopes difficult or impossible.

This will soon change. The next planned space-based transit survey, the *Transiting Exoplanet Survey Satellite (TESS)* mission (Ricker et al. 2015), will observe nearly every star in the sky with $4 < I < 13$; it is currently scheduled to launch in 2017[1]. It will therefore produce a huge number of planet candidates around bright stars, and, due to Malmquist bias, the hot, bright stars for which Doppler tomography is

---

[1] http://space.mit.edu/TESS/TESS/TESS_Overview.html

Table 6.1. Summary of Results

Name	$v \sin i_\star$ (km s^{-1})	$\lambda\,(^\circ)$	b	Comments
HAT-P-41 b	$19.9^{+2.3}_{-1.1}$	$-57.2^{+8.4}_{-7.5}$ or $18.4^{+10.0}_{-8.5}$	...	bimodal solution in λ
KELT-2 Ab	...	...	...	transit not detected
Kepler-13 Ab	76.96 ± 0.61	58.6 ± 2.0	0.256 ± 0.030	...
Kepler-13 B	63.21 ± 1.00	...	...	binary companion to planet host
Kepler-448 b	66.43 ± 0.40	$-1.7^{+1.7}_{-2.1}$	$0.3676^{+0.0025}_{-0.0030}$	...
KOI-366.01	$34.15^{+0.89}_{-0.83}$	...	...	transit not detected
KOI-368.01	$81.20^{+0.43}_{-0.30}$	$\sim 55 - 80$?	...	$\sim 2\sigma$ detection
KOI-972.01	$117.1^{+2.1}_{-1.9}$	...	...	transit not detected
WASP-33 b (2008)	$86.63^{+0.37}_{-0.32}$	$-110.06^{+0.40}_{-0.47}$	$0.218^{+0.011}_{-0.029}$	...
WASP-33 b (2014)	...	$-112.93^{+0.23}_{-0.21}$	$0.0840^{+0.0020}_{-0.0019}$	precession detected
WASP-79 b	$17.347^{+0.073}_{-0.043}$	-98.3 ± 1.9	0.541 ± 0.016	data from Addison et al. (2013)

Note. — Except in the case of λ and b for Kepler-13 Ab, uncertainties are purely statistical and do not take into account systematic sources of error.

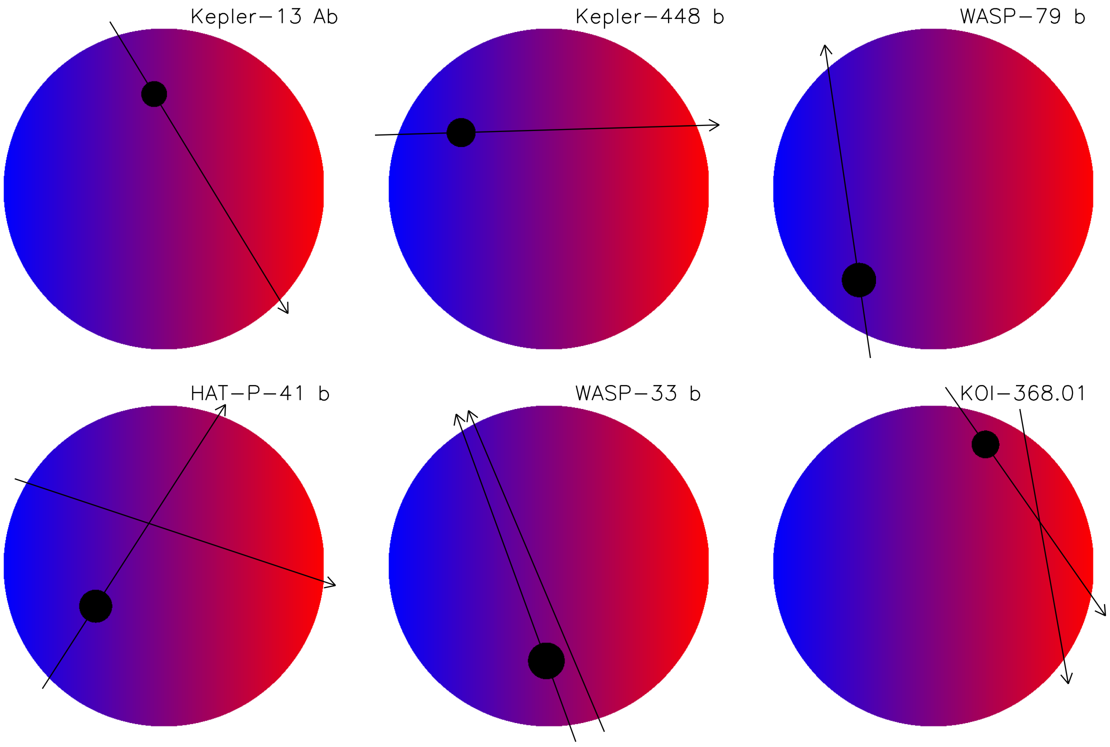

Figure 6.1 Schematics showing the measured transit chords for each of the six planets or planet candidates for which I measure the spin-orbit misalignment. Each panel is marked with the name of the planet or planet candidate, and each transiting companion is shown to scale with respect to its own host star, but the stars are not to scale with each other. For HAT-P-41 b, the two arrows show the transit chords corresponding to the two degenerate solutions for λ that I find; the planetary silhouette is shown on the very slightly preferred high-λ solution. For WASP-33 b, the two chords shown are those in 2008 and 2014; the planetary silhouette is shown on the 2014 chord. For KOI-368.01 I only achieved a $\sim 2\sigma$ detection of the transit and a rough qualitative range of $\lambda \sim 55 - 80°$; the two transit chords shown here correspond to $\lambda = 55°$ and $\lambda = 80°$, with the silhouette of the transiting companion shown on the former chord.

most effective will be overrepresented in the *TESS* sample. Furthermore, due to the brightness of the target sample, many of these planet candidates will be amenable to Doppler tomographic observations with 2-4 m class telescopes, such as the HJST and TS23. The combination of *TESS* planet candidates and Doppler tomographic follow-up has the potential to revolutionize our understanding of the short-period ($P < 150$ days) planetary population of intermediate-mass stars. Furthermore, 8-10 m class telescopes will be able to gather sufficient signal to detect even small transiting planets around these bright stars.

Doppler tomography will also be critical for measuring the spin-orbit misalignment distribution of warm Jupiters. To date there are only four published spin-orbit misalignment measurements for warm Jupiters (Narita et al. 2009a; Hébrard et al. 2010; Santerne et al. 2014; Bourrier et al. 2015), one of which is only a 2σ detection of the Rossiter-McLaughlin effect and two others are on highly eccentric orbits. Due to their smaller orbital velocities (as compared to hot Jupiters), the transits of warm Jupiters last longer (typically $\sim 6 - 12$ hours). For radial velocity Rossiter-McLaughlin observations, it is necessary to observe through the entirety of a single transit in order to securely measure λ. This, however, is not the case for Doppler tomography, which can easily allow the measurement of λ even with observations during part of a transit (although the more of the transit is covered, the more precise the measurement of λ will be; cf. my well-constrained measurement of λ from the full-transit observations WASP-79 b versus my two degenerate and less precise solutions from one-third of a transit for HAT-P-41 b). As I demonstrated with my observations of Kepler-448 b (§3.2), Doppler tomography is well-suited to the observation of warm Jupiters.

Furthermore, very high resolution spectrographs ($R > 100,000$), such as PEPSI on the 2×8.4 m Large Binocular Telescope (Strassmeier et al. 2015), HARPS on the 3.6 m ESO telescope at La Silla (Mayor et al. 2003), and HARPS-N on the 3.58 m Telescopio Nazionale Galileo (Cosentino et al. 2012), allow the use of Doppler tomography for stars with only modest rotation ($v \sin i_\star \sim 3-10$ km s^{-1}; e.g., Collier Cameron et al. 2010a). Doppler tomographic observations with these instruments are the best way to compile a statistically significant sample of spin-orbit misalignment measurements for warm Jupiters transiting both hot and cool stars.

Further into the future, one of the next anticipated revolutionary developments in observational astronomy is the construction of thirty meter-class ground-based telescopes. High-resolution spectrographs on these telescopes, such as the optical G-CLEF (Szentgyorgyi et al. 2014) and near-infrared GMTNIRS (Jaffe et al. 2014), both planned for the Giant Magellan Telescope, will enable Doppler tomography not only of very faint targets, but also a host of other applications requiring very high signal-to-noise or very high time resolution.

Given the rate of change of the impact parameter of Kepler-13 Ab found by Szabó et al. (2012) and the uncertainty on b that I measured in §3.1, I expect that the precession of Kepler-13 Ab will be measurable with Doppler tomography by 2017. This will be important as Masuda (2015) found that such a measurement will be able to unambiguously distinguish between the conflicting values of the system parameters that I found with Doppler tomography and found by Barnes et al. (2011) using the effects of stellar gravity darkening on the lightcurve. The other known transiting planets around rapidly-rotating stars which could be amenable to the detection of precession are KELT-17 b, HAT-P-57 b and WASP-79 b. KELT-17 b is the best case, as it has a highly misaligned orbit ($\lambda = -115.9 \pm 4.1^\circ$; Zhou et al. 2016b), but the star is more slowly rotating than WASP-33 ($v \sin i_\star = 44.2^{+1.5}_{-1.3}$ km s^{-1}) and this planet is newly published, so several more years must elapse before precession could be detected. The spin-orbit misalignment of HAT-P-57 b (Hartman et al. 2015) is only roughly constrained, but λ could be as high as 57.4° (2σ confidence); however, the planet might also be aligned. WASP-79 b (§3.3) has a highly inclined orbit ($\lambda = -98.2 \pm 1.9^\circ$), but its star is much more slowly rotating than either WASP-33 or Kepler-13 A, and should therefore be less dynamically oblate, and so the planetary precession should be much slower.

No other known planet is currently amenable to the detection of orbital precession with Doppler tomography, as all other planets with published Doppler tomographic observations have approximately aligned orbits and thus should display much slower precession than WASP-33 b (Collier Cameron et al. 2010a; Miller et al. 2010; Gandolfi et al. 2012; Brown et al. 2012b; Bieryla et al. 2015; Bourrier et al. 2015; Zhou et al. 2016a). These measurements, however, are the sky-projected spin-orbit misalignment λ, and, in most cases, the stellar inclination $i_\star$, and hence the full three-dimensional spin-orbit misalignment ψ, are not known. If precession was detected for one of these planets, it would be an indication that either ψ is large and $\sin i_\star << 1$, or another perturbing body is present in the system. Current and future transit surveys can provide more targets amenable for the detection of precession via Doppler tomography over the next decade.

Doppler tomography is a technique that will see a great deal of applicability over the coming years. With the planet candidates provided by *TESS*, the push to measure the spin-orbit misalignment distribution of warm Jupiters, further potential for addressing problems in stellar and planetary astrophysics, and new and forthcoming spectroscopic facilities, Doppler tomography is a technique with a bright future.

Appendix A: Spin-Orbit Misalignments from the Literature

In this Appendix I present compilations of spin-orbit misalignment measurements from the literature. I list the data for short-period giant planets–hot Jupiters ($P <$ 10 days, $0.3M_J < M_P < 13M_J$), plus two less massive giant planets (the hot Neptune HAT-P-11 b and the hot super-Neptune/sub-Saturn HAT-P-18 b)–in Table A.1, and for warm Jupiters ($P >$ 10 days, $0.3M_J < M_P < 13M_J$) in Table A.2. I am indebted to René Heller's Holt-Rossiter-McLaughlin Encyclopaedia (http://www2.mps.mpg.de/homes/heller/) for assistance in assembling this compilation of literature data. These data were used in making Figs. 1.7, 1.8, 1.9, 1.10, and 1.11.

Table A.1. Hot Jupiter Spin-Orbit Misalignments and System Parameters from the Literature

Name	$T_{\rm eff}$ (K)	$v \sin i_\star$ (km s^{-1})	P (days)	R_P (R_J)	M_P (M_J)	Par. Ref.	λ (°)	Method	λ Ref.	Comp.?	Comp. Ref.
CoRoT-1 b	5950 ± 150	5.2 ± 1.0	1.509	1.49 ± 0.08	1.03 ± 0.12	1	77 ± 11	RM	2	T	1
CoRoT-2 b	5625 ± 120	11.85 ± 0.50	1.743	1.465 ± 0.029	3.31 ± 0.16	3	7.1 ± 5.0	RM	3; 4		
CoRoT-11 b	6440 ± 120	40.0 ± 0.5	2.994	1.43 ± 0.03	2.33 ± 0.34	5	0.1 ± 2.6	DT	6		
CoRoT-18 b	5440 ± 100	8.0 ± 1.0	1.900	1.31 ± 0.18	3.47 ± 0.38	7	10 ± 20	RM	7		
CoRoT-19 b	6090 ± 70	6 ± 1	3.897	1.29 ± 0.03	1.11 ± 0.06	8	-52^{+27}_{-22}	RM	8		
HAT-P-1 b/ HD 147506 b	6290 ± 110	19.8 ± 1.6	5.633	$0.982^{+0.038}_{-0.105}$	9.04 ± 0.50	9	3.7 ± 2.1	RM	10	S	10
HAT-P-2 b	6290 ± 60	20.8 ± 0.3	5.633	$1.157^{+0.073}_{-0.062}$	9.09 ± 0.24	11	9 ± 10	RM	12	T	13
HAT-P-4 b	5860 ± 80	5.5 ± 0.5	3.056	1.27 ± 0.05	0.68 ± 0.04	14	-4.9 ± 11.9	RM	15	T	15
HAT-P-6 b	6570 ± 80	8.7 ± 1.0	3.853	1.330 ± 0.061	1.057 ± 0.119	16	165 ± 6	RM	12	T	13
HAT-P-7 b	6350 ± 80	3.8 ± 0.5	2.205	$1.363^{+0.195}_{-0.087}$	$1.776^{+0.077}_{-0.049}$	17	155 ± 37	RM	12	T, S	18; 19
HAT-P-8 b	6200 ± 80	11.5 ± 0.5	3.076	$1.50^{+0.08}_{-0.06}$	$1.52^{+0.18}_{-0.16}$	20	$-9.7^{+9.0}_{-7.7}$	RM	21	S	19
HAT-P-9 b	6350 ± 150	11.9 ± 1.0	3.923	1.40 ± 0.06	0.78 ± 0.09	22	-16 ± 8	RM	23		
HAT-P-11 b	4780 ± 50	1.5 ± 1.5	4.888	0.422 ± 0.014	0.081 ± 0.009	24	103^{+26}_{-10}	RM	25	T	24
HAT-P-13 b	5653 ± 90	2.9 ± 1.0	2.916	1.281 ± 0.079	$0.853^{+0.029}_{-0.046}$	26	1.9 ± 8.6	RM	27	1P, T	26; 13
HAT-P-14 b	6600 ± 90	8.4 ± 0.5	4.628	1.150 ± 0.052	2.232 ± 0.059	28	189.1 ± 5.1	RM	15	S	19
HAT-P-16 b	6158 ± 80	3.5 ± 0.5	2.776	1.289 ± 0.066	4.193 ± 0.094	29	-10.0 ± 16	RM	23	S	19
HAT-P-17 b	5246 ± 80	0.3 ± 0.5	10.339	1.010 ± 0.029	0.534 ± 0.018	30	19^{+14}_{-16}	RM	31	1P	31
HAT-P-18 b	4870 ± 50	1.40 ± 0.35	5.508	0.947 ± 0.044	0.196 ± 0.008	32	132 ± 15	RM	32		
HAT-P-23 b	5905 ± 80	8.1 ± 0.5	1.213	1.368 ± 0.090	2.090 ± 0.111	33	-15 ± 22	RM	23		

continued on next page

Table A.1, cont.

Name	T_{eff} (K)	$v \sin i_\star$ (km s^{-1})	P (days)	R_P (R_J)	M_P (M_J)	Par. Ref.	λ (°)	Method	λ Ref.	Comp.?	Comp. Ref.
HAT-P-24 b	6373 ± 80	10.0 ± 0.5	3.355	1.242 ± 0.067	0.685 ± 0.033	34	20 ± 16	RM	12	S	19
HAT-P-30 b	6304 ± 88	3.07 ± 0.24	2.811	1.340 ± 0.065	0.711 ± 0.028	35	73.5 ± 9.0	RM	35	S	19
HAT-P-32 b	6207 ± 88	20.7 ± 0.5	2.150	1.789 ± 0.025	0.860 ± 0.164	36	85.0 ± 1.5	RM	12	T, S	13; 19
HAT-P-34 b	6442 ± 88	24.0 ± 0.5	5.453	$1.197^{+0.128}_{-0.092}$	3.328 ± 0.211	37	0 ± 14	RM	12	T	37
HAT-P-36 b	5620 ± 40	3.12 ± 0.75	1.327	1.304 ± 0.021	1.852 ± 0.088	38	-14 ± 18	RM	38		
HAT-P-56 b	6566 ± 50	40.06 ± 0.50	2.791	1.466 ± 0.040	2.18 ± 0.25	39	7 ± 2	DT	40		
HAT-P-57 b	7500 ± 250	102.1 ± 1.3	2.465	1.413 ± 0.054	< 1.85	41	-16.7 to 3.3 or 27.6 to 57.4	DT	41		
HATS-3 b	6351 ± 76	9.12 ± 1.31	3.548	1.381 ± 0.035	1.071 ± 0.136	42	3 ± 25	RM	43		
HATS-14 b	5408 ± 65	3.1 ± 0.5	2.767	$1.04^{+0.03}_{-0.02}$	1.07 ± 0.07	44	76^{+4}_{-5}	RM	44		
HD 149026 b	6147 ± 50	6.0 ± 0.5	2.877	0.725 ± 0.05	0.36 ± 0.03	45	12 ± 7	RM	12		
HD 189733 b	5040 ± 50	$3.316^{+0.017}_{-0.067}$	2.219	1.138 ± 0.027	$1.144^{+0.057}_{-0.056}$	46; 47	$0.85^{+0.32}_{-0.28}$	RM	47	S	48
HD 209458 b	6065 ± 50	4.4 ± 0.2	3.525	$1.359^{+0.016}_{-0.019}$	$0.685^{+0.015}_{-0.014}$	46; 12	-5 ± 7	RM	12		
K2-29 b/ WASP-152 b	5222 ± 40	3.8 ± 0.1	3.259	$1.000^{+0.071}_{-0.067}$	$0.613^{+0.027}_{-0.026}$	49	1.5 ± 8.7	RM	50	S	50
K2-34 b	6087 ± 38	5.65 ± 0.33	3.000	1.44 ± 0.16	1.726 ± 0.085	51	4^{+11}_{-10}	RM	51	S	51
KELT-6 b	6272 ± 61	4.53 ± 0.26	7.846	1.18 ± 0.11	0.442 ± 0.019	52	-36 ± 11	RM	52	1P	52
KELT-7 b	6789^{+50}_{-49}	$65.0^{+6.0}_{-5.9}$	2.735	$1.533^{+0.046}_{-0.047}$	1.28 ± 0.18	53	2.7 ± 0.6	RM	40		
KELT-17 b	7454 ± 49	$44.2^{+1.5}_{-1.3}$	3.080	$1.525^{+0.065}_{-0.060}$	$1.31^{+0.28}_{-0.29}$	54	-115.9 ± 4.1	DT	54		
Kepler-8 b	6213 ± 150	10.5 ± 0.7	3.523	$1.419^{+0.056}_{-0.058}$	$0.603^{+0.13}_{-0.19}$	55	5 ± 7	RM	12		
Kepler-13 Ab	8511^{+401}_{-383}	65 ± 10	1.764	2.042 ± 0.080	7.95 ± 0.27	56; 57	58.6 ± 2.0	DT	58	S	59
Kepler-63 b	5576 ± 50	5.6 ± 0.8	9.434	0.545 ± 0.018	< 0.38	60	-110^{+22}_{-14}	RM	60		

continued on next page

Table A.1, cont.

Name	$T_{\rm eff}$ (K)	$v \sin i_\star$ (km s^{-1})	P (days)	R_P (R_J)	M_P (M_J)	Par. Ref.	λ (°)	Method	λ Ref.	Comp.?	Comp. Ref.
Qatar-1 b	4910 ± 100	1.7 ± 0.3	1.420	1.18 ± 0.09	1.33 ± 0.05	61	-8.4 ± 7.1	RM	61		
TrES-1 b	5250 ± 200	1.3 ± 0.3	3.030	$1.08^{+0.18}_{-0.04}$	0.75 ± 0.07	62; 63	30 ± 21	RM	63		
TrES-2 b	5960 ± 100	2.0 ± 1.5	2.470	$1.24^{+0.09}_{-0.06}$	$1.28^{+0.09}_{-0.04}$	64	-9 ± 12	RM	65	S	19
TrES-4 b	6200 ± 75	9.5 ± 1.0	3.554	1.799 ± 0.063	0.919 ± 0.073	66; 67	6.3 ± 4.7	RM	68	S	67; 19
WASP-1 b	6200 ± 200	5.77 ± 0.35	2.520	$1.52^{+0.052}_{-0.25}$	0.918 ± 0.091	69; 21	$-79.0^{+4.5}_{-4.3}$	RM	21	S	19
WASP-2 b	5150 ± 80	1.6 ± 0.7	2.152	$1.077^{+0.055}_{-0.058}$	$0.866^{+0.076}_{-0.084}$	70	-153^{+15}_{-11}	RM	70	S	19
WASP-3 b	6332 ± 105	13.9 ± 0.03	1.847	$1.20^{+0.05}_{-0.03}$	$1.90^{+0.10}_{-0.09}$	71	5^{+6}_{-5}	DT	71	S	19
WASP-4 b	5500 ± 100	2.0 ± 1.0	1.338	$1.304^{+0.054}_{-0.042}$	$1.21^{+0.13}_{-0.08}$	72	-1^{+14}_{-12}	spots	73		
WASP-5 b	5700 ± 100	3.5 ± 1.0	1.628	$1.087^{+0.068}_{-0.071}$	$1.58^{+0.13}_{-0.10}$	72	$12.1^{+8.0}_{-10.0}$	RM	70		
WASP-6 b	5450 ± 100	1.4 ± 1.0	3.361	$1.224^{+0.051}_{-0.052}$	$0.503^{+0.019}_{-0.038}$	74	-11^{+18}_{-14}	RM	74		
WASP-7 b	6400 ± 100	17 ± 2	4.955	$0.915^{+0.046}_{-0.040}$	$0.96^{+0.12}_{-0.18}$	75	86.6 ± 6	RM	76		
WASP-8 b	5600 ± 80	2.0 ± 0.6	8.159	$1.038^{+0.007}_{-0.047}$	$2.244^{+0.079}_{-0.093}$	77	$-123.3^{+3.4}_{-3.3}$	RM	77	S, T	77
WASP-11 b/ HAT-P-10 b	4900 ± 65	1.04 ± 0.15	3.722	0.990 ± 0.022	0.492 ± 0.023	38	7 ± 5	RM	38		
WASP-12 b	6300^{+200}_{-100}	$1.6^{+0.8}_{-0.4}$	1.091	1.79 ± 0.09	1.41 ± 0.10	78; 12	59^{+15}_{-20}	RM	12	S	19
WASP-13 b	5989 ± 48	5.74 ± 0.38	4.353	1.407 ± 0.052	0.500 ± 0.037	79	8^{+13}_{-12}	RM	80		
WASP-14 b	6475 ± 100	4.9 ± 1.0	2.244	1.28 ± 0.08	7.3 ± 0.5	81	-33.1 ± 7.4	RM	82	S	19
WASP-15 b	6300 ± 100	4 ± 2	3.752	1.428 ± 0.077	0.542 ± 0.050	83	$-139.6^{+4.3}_{-5.2}$	RM	70		
WASP-16 b	5700 ± 150	3.0 ± 1.0	3.119	$1.008^{+0.083}_{-0.060}$	$0.855^{+0.043}_{-0.076}$	84	11^{+26}_{-19}	RM	12		
WASP-17 b	6650 ± 80	9.8 ± 0.5	3.735	$1.986^{+0.089}_{-0.074}$	$0.453^{+0.043}_{-0.035}$	70	$-148.5^{+4.2}_{-5.1}$	RM	70		
WASP-18 b	6400 ± 100	11.0 ± 1.5	0.941	$1.106^{+0.072}_{-0.054}$	10.30 ± 0.69	85	13 ± 7	RM	12		
WASP-19 b	5500 ± 100	4 ± 2	0.789	1.31 ± 0.06	1.15 ± 0.08	86	15 ± 11	RM	12		

continued on next page

Table A.1, cont.

Name	$T_{\rm eff}$ (K)	$v \sin i_\star$ (km s^{-1})	P (days)	R_P (R_J)	M_P (M_J)	Par. Ref.	λ (°)	Method	λ Ref.	Comp.?	Comp. Ref.
WASP-20 b	6000 ± 100	3.5 ± 0.5	4.900	1.462 ± 0.059	0.311 ± 0.017	87	12.7 ± 4.2	RM	87		
WASP-22 b	6000 ± 100	4.5 ± 0.4	3.533	$1.158^{+0.061}_{-0.038}$	0.588 ± 0.017	88	22 ± 16	RM	88	T	88
WASP-24 b	6075 ± 100	7.0 ± 1.0	2.341	$1.3^{+0.039}_{-0.038}$	$1.071^{+0.036}_{-0.038}$	89	-4.7 ± 4.0	RM	21		
WASP-25 b	5750 ± 100	3.0 ± 1.0	3.765	$1.22^{+0.06}_{-0.05}$	0.58 ± 0.04	90	14.6 ± 6.7	RM	91		
WASP-26 b	5950 ± 100	3.9 ± 0.4	2.757	1.281 ± 0.075	1.028 ± 0.021	88	-34^{+36}_{-26}	RM	12		
WASP-28 b	6100 ± 150	3.1 ± 0.6	3.409	1.213 ± 0.042	0.907 ± 0.043	87	8 ± 18	RM	87		
WASP-31 b	6300 ± 100	7.9 ± 0.6	3.406	1.549 ± 0.050	0.478 ± 0.029	92	-6 ± 6	RM	12	S	92
WASP-32 b	6100 ± 100	4.8 ± 0.8	2.719	1.18 ± 0.07	3.60 ± 0.07	93	$10.5^{+6.4}_{-.65}$	DT	94		
WASP-33 b	7430 ± 100	90 ± 10	1.220	1.497 ± 0.045	2.1 ± 0.2	95; 96	$-112.93^{+0.23}_{-0.21}$	DT	97	T	95
WASP-38 b	6150 ± 80	8.6 ± 0.4	6.872	$1.094^{+0.029}_{-0.028}$	2.691 ± 0.058	98	$7.5^{+4.7}_{-6.1}$	DT	94		
WASP-41 b	5545 ± 33	2.64 ± 0.25	3.052	1.18 ± 0.03	0.94 ± 0.05	99	-29^{+14}_{-10}	RM	99	1P	99
WASP-47 b	5400 ± 100	3.0 ± 0.6	4.159	$1.15^{+0.04}_{-0.02}$	1.14 ± 0.05	100	0 ± 24	RM	101	3P	102; 99
WASP-52 b	5000 ± 100	3.6 ± 0.9	1.750	1.27 ± 0.03	0.46 ± 0.02	103	24^{+17}_{-9}	RM	103		
WASP-66 b	6600 ± 150	13.4 ± 0.9	4.086	1.39 ± 0.09	2.32 ± 0.13	100	-4 ± 22	RM	104		
WASP-71 b	6050 ± 100	9.4 ± 0.5	2.904	1.46 ± 0.13	2.242 ± 0.080	105	20.1 ± 9.7	RM	105		
WASP-79 b	6600 ± 100	19.1 ± 0.7	3.662	1.70 ± 0.11	0.90 ± 0.09	106	-84^{+23}_{-30}	RM	107		
WASP-80 b	4143^{+92}_{-94}	$1.27^{+0.14}_{-0.17}$	3.068	$0.999^{+0.030}_{-0.031}$	$0.538^{+0.035}_{-0.036}$	108	-14^{+14}_{-15}	RM	108		
WASP-84 b	5300 ± 100	4.1 ± 0.3	8.524	0.942 ± 0.022	0.694 ± 0.028	109	-0.3 ± 1.7	RM	110		
WASP-87 b	6450 ± 120	9.6 ± 0.7	1.683	1.385 ± 0.060	2.18 ± 0.15	111	-8 ± 11	RM	104	S	111
WASP-94 Ab	6170 ± 80	4.2 ± 0.5	3.950	$1.72^{+0.06}_{-0.05}$	$0.452^{+0.035}_{-0.032}$	112	151^{+16}_{-23}	RM	112	S	112
WASP-103 b	6110 ± 160	10.6 ± 0.9	0.9255	$1.528^{+0.073}_{-0.047}$	1.490 ± 0.088	113	3 ± 33	RM	104		
WASP-111 b	6400 ± 150	11.2 ± 0.8	2.311	1.442 ± 0.094	1.83 ± 0.15	111	-5 ± 16	RM	111		

continued on next page

Table A.1, cont.

Name	T_{eff} (K)	$v \sin i_\star$ (km s^{-1})	P (days)	R_P (R_J)	M_P (M_J)	Par. Ref.	λ (°)	Method	λ Ref.	Comp.?	Comp. Ref.
WASP-117 b	6040 ± 90	1.55 ± 0.44	10.022	$1.021^{+0.076}_{-0.065}$	0.2755 ± 0.0090	114	44 ± 11	RM	114		
WASP-121 b	6460 ± 140	13.5 ± 0.7	1.275	1.807 ± 0.039	$1.183^{+0.064}_{-0.062}$	115	$-257.8^{+5.5}_{-5.3}$	RM	115		
XO-2 b	5340 ± 32	1.4 ± 0.3	2.616	$0.98^{+0.03}_{-0.01}$	0.57 ± 0.06	116	10 ± 72	RM	117	S, T	116; 117
XO-3 b	6429 ± 50	18.54 ± 0.17	3.192	1.217 ± 0.073	11.79 ± 0.59	118; 119	37.3 ± 3.0	RM	120		
XO-4 b	6397 ± 70	8.8 ± 0.5	4.125	1.34 ± 0.048	1.72 ± 0.20	121	$-46.7^{+8.1}_{-6.1}$	RM	122		

Note. — Method abbreviations: RM: Rossiter-McLaughlin Effect; DT: Doppler tomography. Companion abbreviations: S: stellar; P: planet, preceded by number of known additional planets; T: radial velocity trend; CS: candidate stellar. References: 1: Barge et al. (2008); 2: Pont et al. (2010); 3: Alonso et al. (2008); 4: Bouchy et al. (2008); 5: Gandolfi et al. (2010); 6: Gandolfi et al. (2012); 7: Hébrard et al. (2011b); 8: Guenther et al. (2012); 9: Bakos et al. (2007); 10: Johnson et al. (2008); 11: Pál et al. (2010); 12: Albrecht et al. (2012b); 13: Knutson et al. (2014); 14: Kovács et al. (2007); 15: Winn et al. (2011); 16: Noyes et al. (2008); 17: Pál et al. (2008); 18: Winn et al. (2009c); 19: Ngo et al. (2015); 20: Latham et al. (2009); 21: Simpson et al. (2011); 22: Shporer et al. (2009); 23: Moutou et al. (2011); 24: Bakos et al. (2010); 25: Winn et al. (2010c); 26: Bakos et al. (2009); 27: Winn et al. (2010b); 28: Torres et al. (2010); 29: Buchhave et al. (2010); 30: Howard et al. (2012); 31: Fulton et al. (2013); 32: Esposito et al. (2014); 33: Bakos et al. (2011); 34: Kipping et al. (2010); 35: Johnson et al. (2011); 36: Hartman et al. (2011); 37: Bakos et al. (2012); 38: Mancini et al. (2015); 39: Huang et al. (2015); 40: Zhou et al. (2016a); 41: Hartman et al. (2015); 42: Bayliss et al. (2013); 43: Addison et al. (2014); 44: Zhou et al. (2015); 45: Sato et al. (2005); 46: Torres et al. (2008); 47: Triaud et al. (2009); 48: Roell et al. (2012); 49: Johnson et al. (2016); 50: Santerne et al. (2016); 51: Hirano et al. (2016); 52: Damasso et al. (2015); 53: Bieryla et al. (2015); 54: Zhou et al. (2016b); 55: Jenkins et al. (2010); 56: Szabó et al. (2011); 57: Esteves et al. (2013); 58: Johnson et al. (2014); 59: Santerne et al. (2012); 60: Sanchis-Ojeda et al. (2013); 61: Covino et al. (2013); 62: Alonso et al. (2004); 63: Narita et al. (2007); 64: O'Donovan et al. (2006); 65: Winn et al. (2008b); 66: Mandushev et al. (2007); 67: Daemgen et al. (2009); 68: Narita et al. (2010b); 69: Collier Cameron et al. (2007); 70: Triaud et al. (2010); 71: Miller et al. (2010); 72: Gillon et al. (2009b); 73: Sanchis-Ojeda et al. (2011); 74: Gillon et al. (2009a); 75: Hellier et al. (2009b); 76: Albrecht et al. (2012a); 77: Queloz et al. (2010); 78: Hebb et al. (2009); 79: Gómez Maqueo Chew et al. (2013); 80: Brothwell et al. (2014); 81: Joshi et al. (2009); 82: Johnson et al. (2009); 83: West et al. (2009); 84: Lister et al. (2009); 85: Hellier et al. (2009a); 86: Hebb et al. (2010); 87: Anderson et al. (2015a); 88: Anderson et al. (2011a); 89: Street et al. (2010); 90: Enoch et al. (2011); 91: Brown et al. (2012a); 92: Anderson et al. (2011b); 93: Maxted et al. (2010); 94: Brown et al. (2012b); 95: Collier Cameron et al. (2010b); 96: Lehmann et al. (2015); 97: Johnson et al. (2015); 98: Barros et al. (2011); 99: Neveu-VanMalle et al. (2016); 100: Hellier et al. (2012); 101: Sanchis-Ojeda et al. (2015); 102: Becker et al. (2015); 103: Hébrard et al. (2013); 104: Addison et al. (2016); 105: Smith et al. (2013); 106: Smalley et al. (2012); 107: Addison et al. (2013); 108: Triaud et al. (2015); 109: Anderson et al. (2014b); 110: Anderson et al. (2015b); 111: Anderson et al. (2014a); 112: Neveu-VanMalle et al. (2014); 113: Gillon et al. (2014); 114: Lendl et al. (2014); 115: Delrez et al. (2016); 116: Burke et al. (2007); 117: Narita et al. (2011); 118: Johns-Krull et al. (2008); 119: Winn et al. (2008a); 120: Hirano et al. (2011a); 121: McCullough et al. (2008); 122: Narita et al. (2010a).

Table A.2. Warm Jupiter Spin-Orbit Misalignments and System Parameters from the Literature

Name	$T_{\rm eff}$ (K)	$v \sin i_\star$ (km s^{-1})	P (days)	R_P (R_J)	M_P (M_J)	Par. Ref.	λ (°)	Method	λ Ref.	Comp.?	Comp. Ref.
HD 17156 b	6079 ± 80	2.6 ± 0.5	21.217	$1.023^{+0.070}_{-0.055}$	$3.212^{+0.069}_{-0.082}$	1	10.0 ± 5.1	RM	2		
HD 80606 b	5573 ± 44	1.80 ± 0.5	111.436	0.9 ± 0.10	4.0 ± 0.3	3; 4	42 ± 8	RM	5	S	6
Kepler-420 b	5520 ± 80	4.6 ± 0.2	86.648	0.94 ± 0.12	1.45 ± 0.35	7	74^{+32}_{-46}	RM	7	S	7
Kepler-448 b	6820 ± 20	$60.0^{+0.8}_{-0.9}$	17.855	1.43 ± 0.13	< 10	8	$12.5^{+3.0}_{-2.9}$	DT	8		

Note. — Method abbreviations: RM: Rossiter-McLaughlin Effect; DT: Doppler tomography. Companion abbreviations: S: stellar; P: planet, preceded by number of known additional planets; T: radial velocity trend; CS: candidate stellar. References: 1: Winn et al. (2009a); 2: Narita et al. (2009a); 3: Valenti & Fischer (2005); 4: Moutou et al. (2009); 5: Hébrard et al. (2010); 6: Naef et al. (2001); 7: Santerne et al. (2014); 8: Bourrier et al. (2015).

Bibliography

Adams, E. R., Ciardi, D. R., Dupree, A. K., Gautier, III, T. N., Kulesa, C., & McCarthy, D. 2012, AJ, 144, 42

Addison, B. C., Tinney, C. G., Wright, D. J., & Bayliss, D. 2014, ApJ, 792, 112

—. 2016, ApJ, 823, 29

Addison, B. C., Tinney, C. G., Wright, D. J., et al. 2013, ApJ, 774, L9

Aerts, C., Puls, J., Godart, M., & Dupret, M.-A. 2009, A&A, 508, 409

Ahlers, J. P., Barnes, J. W., & Barnes, R. 2015, ApJ, 814, 67

Ahlers, J. P., Seubert, S. A., & Barnes, J. W. 2014, ApJ, 786, 131

Aitken, R. G. 1904, Lick Observatory Bulletin, 3, 6

Albrecht, S., Winn, J. N., Butler, R. P., et al. 2012a, ApJ, 744, 189

Albrecht, S., Winn, J. N., Johnson, J. A., et al. 2012b, ApJ, 757, 18

Albrecht, S., Winn, J. N., Marcy, G. W., Howard, A. W., Isaacson, H., & Johnson, J. A. 2013, ApJ, 771, 11

Albrecht, S., Winn, J. N., Torres, G., et al. 2014, ApJ, 785, 83

Alonso, R., Auvergne, M., Baglin, A., et al. 2008, A&A, 482, L21

Alonso, R., Brown, T. M., Torres, G., et al. 2004, ApJ, 613, L153

Ammler-von Eiff, M. & Reiners, A. 2012, A&A, 542, A116

Anderson, D. R., Brown, D. J. A., Collier Cameron, A., et al. 2014a, arXiv:1410.3449

Anderson, D. R., Collier Cameron, A., Delrez, L., et al. 2014b, MNRAS, 445, 1114

Anderson, D. R., Collier Cameron, A., Gillon, M., et al. 2011a, A&A, 534, A16

Anderson, D. R., Collier Cameron, A., Hellier, C., et al. 2011b, A&A, 531, A60

—. 2015a, A&A, 575, A61

Anderson, D. R., Hellier, C., Gillon, M., et al. 2010, ApJ, 709, 159

Anderson, D. R., Triaud, A. H. M. J., Turner, O. D., et al. 2015b, ApJ, 800, L9

Bakos, G. Á., Hartman, J., Torres, G., et al. 2011, ApJ, 742, 116

Bakos, G. Á., Hartman, J. D., Torres, G., et al. 2012, AJ, 144, 19

Bakos, G. Á., Howard, A. W., Noyes, R. W., et al. 2009, ApJ, 707, 446

Bakos, G. Á., Kovács, G., Torres, G., et al. 2007, ApJ, 670, 826

Bakos, G. Á., Lázár, J., Papp, I., Sári, P., & Green, E. M. 2002, PASP, 114, 974

Bakos, G. Á., Torres, G., Pál, A., et al. 2010, ApJ, 710, 1724

Balona, L. A. 2013, MNRAS, 431, 2240

Barge, P., Baglin, A., Auvergne, M., et al. 2008, A&A, 482, L17

Barnes, J. W. 2009, ApJ, 705, 683

Barnes, J. W., Ahlers, J. P., Seubert, S. A., & Relles, H. M. 2015a, ApJ, 808, L38

Barnes, J. W., Linscott, E., & Shporer, A. 2011, ApJS, 197, 10

Barnes, J. W., van Eyken, J. C., Jackson, B. K., Ciardi, D. R., & Fortney, J. J. 2013, ApJ, 774, 53

Barnes, R., Deitrick, R., Greenberg, R., Quinn, T. R., & Raymond, S. N. 2015b, ApJ, 801, 101

Barros, S. C. C., Faedi, F., Collier Cameron, A., et al. 2011, A&A, 525, A54

Batalha, N. M., Rowe, J. F., Bryson, S. T., et al. 2013, ApJS, 204, 24

Bate, M. R., Lodato, G., & Pringle, J. E. 2010, MNRAS, 401, 1505

Batygin, K. 2012, Nature, 491, 418

Batygin, K. & Adams, F. C. 2013, ApJ, 778, 169

Bayliss, D., Zhou, G., Penev, K., et al. 2013, AJ, 146, 113

Beatty, T. G., Pepper, J., Siverd, R. J., et al. 2012, ApJ, 756, L39

Beck, J. G. & Giles, P. 2005, ApJ, 621, L153

Becker, J. C., Vanderburg, A., Adams, F. C., Rappaport, S. A., & Schwengeler, H. M. 2015, ApJ, 812, L18

Bieryla, A., Collins, K., Beatty, T. G., et al. 2015, AJ, 150, 12

Borucki, W. J., Koch, D., Basri, G., et al. 2010, Science, 327, 977

Borucki, W. J., Koch, D. G., Basri, G., et al. 2011, ApJ, 736, 19

Bouchy, F., Queloz, D., Deleuil, M., et al. 2008, A&A, 482, L25

Bourrier, V. & Hébrard, G. 2014, A&A, 569, A65

Bourrier, V., Lecavelier des Etangs, A., Hébrard, G., et al. 2015, A&A, 579, A55

Brogi, M., Snellen, I. A. G., de Kok, R. J., Albrecht, S., Birkby, J., & de Mooij, E. J. W. 2012, Nature, 486, 502

Brogi, M., Snellen, I. A. G., de Kok, R. J., Albrecht, S., Birkby, J. L., & de Mooij, E. J. W. 2013, ApJ, 767, 27

Brothwell, R. D., Watson, C. A., Hébrard, G., et al. 2014, MNRAS, 440, 3392

Brown, D. J. A., Cameron, A. C., Anderson, D. R., et al. 2012a, MNRAS, 423, 1503

Brown, D. J. A., Collier Cameron, A., Díaz, R. F., et al. 2012b, ApJ, 760, 139

Brown, T. M., Baliber, N., Bianco, F. B., et al. 2013, PASP, 125, 1031

Buchhave, L. A., Bakos, G. Á., Hartman, J. D., et al. 2010, ApJ, 720, 1118

Burke, C. J., Bryson, S. T., Mullally, F., et al. 2014, ApJS, 210, 19

Burke, C. J., McCullough, P. R., Valenti, J. A., et al. 2007, ApJ, 671, 2115

Campante, T. L., Lund, M. N., Kuszlewicz, J. S., et al. 2016, ApJ, 819, 85

Cantiello, M., Langer, N., Brott, I., et al. 2009, A&A, 499, 279

Chaplin, W. J., Sanchis-Ojeda, R., Campante, T. L., et al. 2013, ApJ, 766, 101

Charbonneau, D., Berta, Z. K., Irwin, J., et al. 2009, Nature, 462, 891

Charbonneau, D., Brown, T. M., Latham, D. W., & Mayor, M. 2000, ApJ, 529, L45

Chatterjee, S., Ford, E. B., Matsumura, S., & Rasio, F. A. 2008, ApJ, 686, 580

Ciardi, D. R., van Eyken, J. C., Barnes, J. W., et al. 2015, ApJ, 809, 42

Claret, A. 2004, A&A, 428, 1001

Cochran, W. D., Endl, M., McArthur, B., et al. 2004, ApJ, 611, L133

Collier Cameron, A., Bouchy, F., Hébrard, G., et al. 2007, MNRAS, 375, 951

Collier Cameron, A., Bruce, V. A., Miller, G. R. M., Triaud, A. H. M. J., & Queloz, D. 2010a, MNRAS, 403, 151

Collier Cameron, A., Guenther, E., Smalley, B., et al. 2010b, MNRAS, 407, 507

Colón, K. D. & Ford, E. B. 2011, PASP, 123, 1391

Cosentino, R., Lovis, C., Pepe, F., et al. 2012, in Proc. SPIE, Vol. 8446, Ground-based and Airborne Instrumentation for Astronomy IV, 84461V

Coughlin, J. L., Mullally, F., Thompson, S. E., et al. 2016, ApJS, 224, 12

Coughlin, J. L., Thompson, S. E., Bryson, S. T., et al. 2014, AJ, 147, 119

Covino, E., Esposito, M., Barbieri, M., et al. 2013, A&A, 554, A28

Crepp, J. R. & Johnson, J. A. 2011, ApJ, 733, 126

Daemgen, S., Hormuth, F., Brandner, W., et al. 2009, A&A, 498, 567

Damasso, M., Esposito, M., Nascimbeni, V., et al. 2015, A&A, 581, L6

Dawson, R. I. 2014, ApJ, 790, L31

Dawson, R. I. & Chiang, E. 2014, Science, 346, 212

Dawson, R. I. & Murray-Clay, R. A. 2013, ApJ, 767, L24

Dawson, R. I., Murray-Clay, R. A., & Johnson, J. A. 2015, ApJ, 798, 66

Delrez, L., Santerne, A., Almenara, J.-M., et al. 2016, MNRAS, 458, 4025

Donati, J.-F., Semel, M., Carter, B. D., Rees, D. E., & Collier Cameron, A. 1997, MNRAS, 291, 658

Dressing, C. D. & Charbonneau, D. 2013, ApJ, 767, 95

Eastman, J., Siverd, R., & Gaudi, B. S. 2010, PASP, 122, 935

Endl, M., Robertson, P., Cochran, W. D., et al. 2012, ApJ, 759, 19

Enoch, B., Cameron, A. C., Anderson, D. R., et al. 2011, MNRAS, 410, 1631

Esposito, M., Covino, E., Mancini, L., et al. 2014, A&A, 564, L13

Esteves, L. J., De Mooij, E. J. W., & Jayawardhana, R. 2013, ApJ, 772, 51

Fabrycky, D. & Tremaine, S. 2007, ApJ, 669, 1298

Fabrycky, D. C. & Winn, J. N. 2009, ApJ, 696, 1230

Fielding, D. B., McKee, C. F., Socrates, A., Cunningham, A. J., & Klein, R. I. 2015, MNRAS, 450, 3306

Figueira, P., Pepe, F., Lovis, C., & Mayor, M. 2010, A&A, 515, A106

Fischer, D. A., Anglada-Escude, G., Arriagada, P., et al. 2016, PASP, 128, 066001

Fischer, D. A. & Valenti, J. 2005, ApJ, 622, 1102

Foreman-Mackey, D., Hogg, D. W., Lang, D., & Goodman, J. 2013, PASP, 125, 306

Fossati, L., Ryabchikova, T., Shulyak, D. V., et al. 2011, MNRAS, 417, 495

Foucart, F. & Lai, D. 2011, MNRAS, 412, 2799

Fulton, B. J., Howard, A. W., Winn, J. N., et al. 2013, ApJ, 772, 80

Gandolfi, D., Collier Cameron, A., Endl, M., et al. 2012, A&A, 543, L5

Gandolfi, D., Hébrard, G., Alonso, R., et al. 2010, A&A, 524, A55

Gatewood, G. & Eichhorn, H. 1973, AJ, 78, 769

Gaudi, B. S. & Winn, J. N. 2007, ApJ, 655, 550

Gillon, M., Anderson, D. R., Collier-Cameron, A., et al. 2014, A&A, 562, L3

Gillon, M., Anderson, D. R., Triaud, A. H. M. J., et al. 2009a, A&A, 501, 785

Gillon, M., Jehin, E., Lederer, S. M., et al. 2016, Nature, 533, 221

Gillon, M., Smalley, B., Hebb, L., et al. 2009b, A&A, 496, 259

Gómez Maqueo Chew, Y., Faedi, F., Cargile, P., et al. 2013, ApJ, 768, 79

Goodman, J. & Weare, J. 2010, Commun. Appl. Math. Comput. Sci, 5, 65

Gray, D. F. 2005, The Observation and Analysis of Stellar Photospheres, 3rd edn. (Cambridge: Cambridge University Press)

Gray, D. F. & Brown, K. I. T. 2006, PASP, 118, 399

Groot, P. J. 2012, ApJ, 745, 55

Guenther, E. W., Díaz, R. F., Gazzano, J.-C., et al. 2012, A&A, 537, A136

Guenther, E. W., Hartmann, M., Esposito, M., Hatzes, A. P., Cusano, F., & Gandolfi, D. 2009, A&A, 507, 1659

Hartman, J. D., Bakos, G. Á., Béky, B., et al. 2012, AJ, 144, 139

Hartman, J. D., Bakos, G. Á., Buchhave, L. A., et al. 2015, AJ, 150, 197

Hartman, J. D., Bakos, G. Á., Torres, G., et al. 2011, ApJ, 742, 59

Hay, K. L., Collier-Cameron, A., Doyle, A. P., et al. 2016, arXiv:1607.00774

Hebb, L., Collier-Cameron, A., Loeillet, B., et al. 2009, ApJ, 693, 1920

Hebb, L., Collier-Cameron, A., Triaud, A. H. M. J., et al. 2010, ApJ, 708, 224

Hébrard, G., Collier Cameron, A., Brown, D. J. A., et al. 2013, A&A, 549, A134

Hébrard, G., Désert, J.-M., Díaz, R. F., et al. 2010, A&A, 516, A95

Hébrard, G., Ehrenreich, D., Bouchy, F., et al. 2011a, A&A, 527, L11

Hébrard, G., Evans, T. M., Alonso, R., et al. 2011b, A&A, 533, A130

Hellier, C., Anderson, D. R., Collier Cameron, A., et al. 2009a, Nature, 460, 1098

—. 2012, MNRAS, 426, 739

Hellier, C., Anderson, D. R., Gillon, M., et al. 2009b, ApJ, 690, L89

Henry, G. W., Marcy, G. W., Butler, R. P., & Vogt, S. S. 2000, ApJ, 529, L41

Herrero, E., Morales, J. C., Ribas, I., & Naves, R. 2011, A&A, 526, L10

Hirano, T., Narita, N., Sato, B., et al. 2011a, PASJ, 63, L57

Hirano, T., Narita, N., Shporer, A., Sato, B., Aoki, W., & Tamura, M. 2011b, PASJ, 63, 531

Hirano, T., Nowak, G., Kuzuhara, M., et al. 2016, ApJ, 825, 53

Holt, J. R. 1893, Astronomy and Astro-Physics, 12, 646

Howard, A. W., Bakos, G. Á., Hartman, J., et al. 2012, ApJ, 749, 134

Howarth, I. D. 2016, MNRAS, 457, 3769

Howell, S. B., Sobeck, C., Haas, M., et al. 2014, PASP, 126, 398

Huang, C. X., Hartman, J. D., Bakos, G. Á., et al. 2015, AJ, 150, 85

Huber, D., Carter, J. A., Barbieri, M., et al. 2013, Science, 342, 331

Iorio, L. 2011, Ap&SS, 331, 485

—. 2016, MNRAS, 455, 207

Jaffe, D. T., Barnes, S., Brooks, C., et al. 2014, in Proc. SPIE, Vol. 9147, Ground-based and Airborne Instrumentation for Astronomy V, 914722

Jenkins, J. M., Borucki, W. J., Koch, D. G., et al. 2010, ApJ, 724, 1108

Johns-Krull, C. M., McCullough, P. R., Burke, C. J., et al. 2008, ApJ, 677, 657

Johns-Krull, C. M., Prato, L., McLane, J. N., et al. 2016, arXiv:1606.02701

Johnson, J. A., Fischer, D. A., Marcy, G. W., et al. 2007, ApJ, 665, 785

Johnson, J. A., Morton, T. D., & Wright, J. T. 2013, ApJ, 763, 53

Johnson, J. A., Winn, J. N., Albrecht, S., Howard, A. W., Marcy, G. W., & Gazak, J. Z. 2009, PASP, 121, 1104

Johnson, J. A., Winn, J. N., Bakos, G. Á., et al. 2011, ApJ, 735, 24

Johnson, J. A., Winn, J. N., Narita, N., et al. 2008, ApJ, 686, 649

Johnson, M. C., Cochran, W. D., Albrecht, S., et al. 2014, ApJ, 790, 30

Johnson, M. C., Cochran, W. D., Collier Cameron, A., & Bayliss, D. 2015, ApJ, 810, L23

Johnson, M. C., Gandolfi, D., Fridlund, M., et al. 2016, AJ, 151, 171

Joshi, Y. C., Pollacco, D., Collier Cameron, A., et al. 2009, MNRAS, 392, 1532

Kaib, N. A., Raymond, S. N., & Duncan, M. J. 2011, ApJ, 742, L24

Kalas, P., Graham, J. R., Chiang, E., et al. 2008, Science, 322, 1345

Kallinger, T. & Matthews, J. M. 2010, ApJ, 711, L35

Kamiaka, S., Masuda, K., Xue, Y., et al. 2015, PASJ, 67, 94

Kipping, D. M. 2013, MNRAS, 435, 2152

Kipping, D. M., Bakos, G. Á., Hartman, J., et al. 2010, ApJ, 725, 2017

Kjeldsen, H. & Bedding, T. R. 1995, A&A, 293

Kley, W. & Nelson, R. P. 2012, ARA&A, 50, 211

Knutson, H. A., Fulton, B. J., Montet, B. T., et al. 2014, ApJ, 785, 126

Konacki, M., Torres, G., Jha, S., & Sasselov, D. D. 2003, Nature, 421, 507

Kostov, V. B., McCullough, P. R., Carter, J. A., et al. 2014, ApJ, 784, 14

Kovács, G., Bakos, G. Á., Torres, G., et al. 2007, ApJ, 670, L41

Kovács, G., Kovács, T., Hartman, J. D., et al. 2013, A&A, 553, A44

Kozai, Y. 1962, AJ, 67, 591

Kraft, R. P. 1967, ApJ, 150, 551

Kreidberg, L. 2015, PASP, 127, 1161

Kupka, F. G., Ryabchikova, T. A., Piskunov, N. E., Stempels, H. C., & Weiss, W. W. 2000, Baltic Astronomy, 9, 590

Lagrange, A.-M., Gratadour, D., Chauvin, G., et al. 2009, A&A, 493, L21

Lai, D. 2014, MNRAS, 440, 3532

Lai, D., Foucart, F., & Lin, D. N. C. 2011, MNRAS, 412, 2790

Lang, D., Hogg, D. W., Mierle, K., Blanton, M., & Roweis, S. 2010, AJ, 139, 1782

Latham, D. W., Bakos, G. Á., Torres, G., et al. 2009, ApJ, 704, 1107

Lehmann, H., Guenther, E., Sebastian, D., Döllinger, M., Hartmann, M., & Mkrtichian, D. E. 2015, A&A, 578, L4

Lendl, M., Triaud, A. H. M. J., Anderson, D. R., et al. 2014, A&A, 568, A81

Li, G. & Winn, J. N. 2016, ApJ, 818, 5

Lidov, M. L. 1962, Planet. Space Sci., 9, 719

Lillo-Box, J., Barrado, D., Mancini, L., et al. 2015, A&A, 576, A88

Lin, D. N. C., Bodenheimer, P., & Richardson, D. C. 1996, Nature, 380, 606

Lister, T. A., Anderson, D. R., Gillon, M., et al. 2009, ApJ, 703, 752

Lloyd, J. P. 2011, ApJ, 739, L49

—. 2013, ApJ, 774, L2

Loeillet, B., Shporer, A., Bouchy, F., et al. 2008, A&A, 481, 529

Lomb, N. R. 1976, Ap&SS, 39, 447

López-Morales, M., Triaud, A. H. M. J., Rodler, F., et al. 2014, ApJ, 792, L31

Macintosh, B., Graham, J. R., Barman, T., et al. 2015, Science, 350, 64

Mancini, L., Esposito, M., Covino, E., et al. 2015, A&A, 579, A136

Mandushev, G., O'Donovan, F. T., Charbonneau, D., et al. 2007, ApJ, 667, L195

Mann, A. W., Gaidos, E., Lépine, S., & Hilton, E. J. 2012, ApJ, 753, 90

Markwardt, C. B. 2009, in Astronomical Society of the Pacific Conference Series, Vol. 411, Astronomical Data Analysis Software and Systems XVIII, ed. D. A. Bohlender, D. Durand, & P. Dowler, 251

Marois, C., Macintosh, B., Barman, T., et al. 2008, Science, 322, 1348

Marois, C., Zuckerman, B., Konopacky, Q. M., Macintosh, B., & Barman, T. 2010, Nature, 468, 1080

Masuda, K. 2015, ApJ, 805, 28

Mathias, P., Le Contel, J.-M., Chapellier, E., et al. 2004, A&A, 417, 189

Matsakos, T. & Königl, A. 2015, ApJ, 809, L20

Maxted, P. F. L., Anderson, D. R., Collier Cameron, A., et al. 2010, PASP, 122, 1465

Mayor, M., Pepe, F., Queloz, D., et al. 2003, The Messenger, 114, 20

Mayor, M. & Queloz, D. 1995, Nature, 378, 355

Mazeh, T., Nachmani, G., Sokol, G., Faigler, S., & Zucker, S. 2012, A&A, 541, A56

Mazeh, T., Perets, H. B., McQuillan, A., & Goldstein, E. S. 2015, ApJ, 801, 3

McArthur, B. E., Benedict, G. F., Barnes, R., et al. 2010, ApJ, 715, 1203

McCullough, P. R., Burke, C. J., Valenti, J. A., et al. 2008, arXiv:0805.2921

McCullough, P. R., Stys, J. E., Valenti, J. A., et al. 2006, ApJ, 648, 1228

McLaughlin, D. B. 1924, ApJ, 60, 22

McQuillan, A., Aigrain, S., & Mazeh, T. 2013, MNRAS, 432, 1203

Miller, G. R. M., Collier Cameron, A., Simpson, E. K., et al. 2010, A&A, 523, A52

Mislis, D. & Hodgkin, S. 2012, MNRAS, 422, 1512

Morton, T. D., Bryson, S. T., Coughlin, J. L., et al. 2016, ApJ, 822, 86

Moutou, C., Díaz, R. F., Udry, S., et al. 2011, A&A, 533, A113

Moutou, C., Hébrard, G., Bouchy, F., et al. 2009, A&A, 498, L5

Mugrauer, M., Neuhäuser, R., Mazeh, T., Guenther, E., Fernández, M., & Broeg, C. 2006, Astronomische Nachrichten, 327, 321

Mulders, G. D., Pascucci, I., & Apai, D. 2015, ApJ, 798, 112

Naef, D., Latham, D. W., Mayor, M., et al. 2001, A&A, 375, L27

Naoz, S., Farr, W. M., Lithwick, Y., Rasio, F. A., & Teyssandier, J. 2011, Nature, 473, 187

—. 2013, MNRAS, 431, 2155

Naoz, S., Farr, W. M., & Rasio, F. A. 2012, ApJ, 754, L36

Narita, N., Enya, K., Sato, B., et al. 2007, PASJ, 59, 763

Narita, N., Hirano, T., Sanchis-Ojeda, R., et al. 2010a, PASJ, 62, L61

Narita, N., Hirano, T., Sato, B., et al. 2009a, PASJ, 61, 991

—. 2011, PASJ, 63, L67

Narita, N., Sato, B., Hirano, T., & Tamura, M. 2009b, PASJ, 61, L35

Narita, N., Sato, B., Hirano, T., Winn, J. N., Aoki, W., & Tamura, M. 2010b, PASJ, 62, 653

Neveu-VanMalle, M., Queloz, D., Anderson, D. R., et al. 2014, A&A, 572, A49

—. 2016, A&A, 586, A93

Ngo, H., Knutson, H. A., Hinkley, S., et al. 2015, ApJ, 800, 138

—. 2016, arXiv:1606.07102

Noyes, R. W., Bakos, G. Á., Torres, G., et al. 2008, ApJ, 673, L79

O'Donovan, F. T., Charbonneau, D., Mandushev, G., et al. 2006, ApJ, 651, L61

Pál, A., Bakos, G. Á., Torres, G., et al. 2008, ApJ, 680, 1450

—. 2010, MNRAS, 401, 2665

Pepper, J., Pogge, R. W., DePoy, D. L., et al. 2007, PASP, 119, 923

Petigura, E. A., Howard, A. W., & Marcy, G. W. 2013, PNAS, 110, 19273

Petrovich, C. 2015, ApJ, 805, 75

Piskorz, D., Knutson, H. A., Ngo, H., et al. 2015, ApJ, 814, 148

Placek, B., Knuth, K. H., & Angerhausen, D. 2014, ApJ, 795, 112

Poleski, R., McCullough, P. R., Valenti, J. A., Burke, C. J., Machalek, P., & Janes, K. 2010, ApJS, 189, 134

Pollacco, D. L., Skillen, I., Collier Cameron, A., et al. 2006, PASP, 118, 1407

Pont, F., Endl, M., Cochran, W. D., et al. 2010, MNRAS, 402, L1

Queloz, D., Anderson, D. R., Collier Cameron, A., et al. 2010, A&A, 517, L1

Queloz, D., Eggenberger, A., Mayor, M., et al. 2000, A&A, 359, L13

Raetz, S., Schmidt, T. O. B., Czesla, S., et al. 2016, arXiv:1605.05091

Rasio, F. A. & Ford, E. B. 1996, Science, 274, 954

Redfield, S., Endl, M., Cochran, W. D., & Koesterke, L. 2008, ApJ, 673, L87

Reffert, S., Bergmann, C., Quirrenbach, A., Trifonov, T., & Künstler, A. 2015, A&A, 574, A116

Reiners, A. & Schmitt, J. H. M. M. 2002, A&A, 384, 155

Ricker, G. R., Winn, J. N., Vanderspek, R., et al. 2015, Journal of Astronomical Telescopes, Instruments, and Systems, 1, 014003

Roberts, S., Osborne, M., Ebden, M., et al. 2013, RSPTA, 371, 20110550

Robertson, P., Horner, J., Wittenmyer, R. A., et al. 2012, ApJ, 754, 50

Roell, T., Neuhäuser, R., Seifahrt, A., & Mugrauer, M. 2012, A&A, 542, A92

Rogers, T. M. & Lin, D. N. C. 2013, ApJ, 769, L10

Rogers, T. M., Lin, D. N. C., & Lau, H. H. B. 2012, ApJ, 758, L6

Rogers, T. M., Lin, D. N. C., McElwaine, J. N., & Lau, H. H. B. 2013, ApJ, 772, 21

Rossiter, R. A. 1924, ApJ, 60, 15

Rowe, J. F., Bryson, S. T., Marcy, G. W., et al. 2014, ApJ, 784, 45

Roxburgh, I. W. 2001, A&A, 377, 688

Sanchis-Ojeda, R., Fabrycky, D. C., Winn, J. N., et al. 2012, Nature, 487, 449

Sanchis-Ojeda, R. & Winn, J. N. 2011, ApJ, 743, 61

Sanchis-Ojeda, R., Winn, J. N., Dai, F., et al. 2015, ApJ, 812, L11

Sanchis-Ojeda, R., Winn, J. N., Holman, M. J., Carter, J. A., Osip, D. J., & Fuentes, C. I. 2011, ApJ, 733, 127

Sanchis-Ojeda, R., Winn, J. N., Marcy, G. W., et al. 2013, ApJ, 775, 54

Santerne, A., Hébrard, G., Deleuil, M., et al. 2014, A&A, 571, A37

Santerne, A., Hébrard, G., Lillo-Box, J., et al. 2016, ApJ, 824, 55

Santerne, A., Moutou, C., Barros, S. C. C., et al. 2012, A&A, 544, L12

Sato, B., Fischer, D. A., Henry, G. W., et al. 2005, ApJ, 633, 465

Scargle, J. D. 1982, ApJ, 263, 835

Schlaufman, K. C. 2010, ApJ, 719, 602

Schlaufman, K. C. & Winn, J. N. 2013, ApJ, 772, 143

Seager, S. & Mallén-Ornelas, G. 2003, ApJ, 585, 1038

Shporer, A., Bakos, G. Á., Bouchy, F., et al. 2009, ApJ, 690, 1393

Shporer, A., Brown, T., Mazeh, T., & Zucker, S. 2012, New A, 17, 309

Shporer, A., Jenkins, J. M., Rowe, J. F., et al. 2011, AJ, 142, 195

Shporer, A., O'Rourke, J. G., Knutson, H. A., et al. 2014, ApJ, 788, 92

Simón-Díaz, S. & Herrero, A. 2014, A&A, 562, A135

Simpson, E. K., Pollacco, D., Cameron, A. C., et al. 2011, MNRAS, 414, 3023

Sing, D. K., Fortney, J. J., Nikolov, N., et al. 2016, Nature, 529, 59

Slawson, R. W., Prša, A., Welsh, W. F., et al. 2011, AJ, 142, 160

Smalley, B., Anderson, D. R., Collier-Cameron, A., et al. 2012, A&A, 547, A61

Smith, A. M. S., Anderson, D. R., Bouchy, F., et al. 2013, A&A, 552, A120

Socrates, A., Katz, B., Dong, S., & Tremaine, S. 2012, ApJ, 750, 106

Southworth, J. 2011, MNRAS, 417, 2166

Spalding, C. & Batygin, K. 2015, ApJ, 811, 82

Spalding, C., Batygin, K., & Adams, F. C. 2014, ApJ, 797, L29

Stello, D., Bruntt, H., Kjeldsen, H., et al. 2007, MNRAS, 377, 584

Strassmeier, K. G., Ilyin, I., Järvinen, A., et al. 2015, Astronomische Nachrichten, 336, 324

Street, R. A., Simpson, E., Barros, S. C. C., et al. 2010, ApJ, 720, 337

Szabó, G. M., Pál, A., Derekas, A., Simon, A. E., Szalai, T., & Kiss, L. L. 2012, MNRAS, 421, L122

Szabó, G. M., Simon, A., & Kiss, L. L. 2014, MNRAS, 437, 1045

Szabó, G. M., Szabó, R., Benkő, J. M., et al. 2011, ApJ, 736, L4

Szentgyorgyi, A., Barnes, S., Bean, J., et al. 2014, in Proc. SPIE, Vol. 9147, Ground-based and Airborne Instrumentation for Astronomy V, 914726

Torres, G., Bakos, G. Á., Hartman, J., et al. 2010, ApJ, 715, 458

Torres, G., Winn, J. N., & Holman, M. J. 2008, ApJ, 677, 1324

Triana, S. A., Moravveji, E., Pápics, P. I., Aerts, C., Kawaler, S. D., & Christensen-Dalsgaard, J. 2015, ApJ, 810, 16

Triaud, A. H. M. J., Collier Cameron, A., Queloz, D., et al. 2010, A&A, 524, A25

Triaud, A. H. M. J., Gillon, M., Ehrenreich, D., et al. 2015, MNRAS, 450, 2279

Triaud, A. H. M. J., Queloz, D., Bouchy, F., et al. 2009, A&A, 506, 377

Tull, R. G. 1998, in Proc. SPIE, Vol. 3355, Optical Astronomical Instrumentation, ed. S. D'Odorico, 387–398

Tull, R. G., MacQueen, P. J., Sneden, C., & Lambert, D. L. 1995, PASP, 107, 251

Valenti, J. A. & Fischer, D. A. 2005, ApJS, 159, 141

van de Kamp, P. 1963, AJ, 68, 515

van Eyken, J. C., Ciardi, D. R., von Braun, K., et al. 2012, ApJ, 755, 42

Vanderburg, A., Latham, D. W., Buchhave, L. A., et al. 2016, ApJS, 222, 14

Wagner, K., Apai, D., Kasper, M., et al. 2016, arXiv:1607.02525

Walker, G. A. H., Walker, A. R., Irwin, A. W., Larson, A. M., Yang, S. L. S., & Richardson, D. C. 1995, Icarus, 116, 359

West, R. G., Anderson, D. R., Gillon, M., et al. 2009, AJ, 137, 4834

Winn, J. N., Fabrycky, D., Albrecht, S., & Johnson, J. A. 2010a, ApJ, 718, L145

Winn, J. N. & Fabrycky, D. C. 2015, ARA&A, 53, 409

Winn, J. N., Holman, M. J., Henry, G. W., et al. 2007a, AJ, 133, 1828

—. 2009a, ApJ, 693, 794

Winn, J. N., Holman, M. J., Torres, G., et al. 2008a, ApJ, 683, 1076

Winn, J. N., Howard, A. W., Johnson, J. A., et al. 2009b, ApJ, 703, 2091

—. 2011, AJ, 141, 63

Winn, J. N., Johnson, J. A., Albrecht, S., et al. 2009c, ApJ, 703, L99

Winn, J. N., Johnson, J. A., Howard, A. W., et al. 2010b, ApJ, 718, 575

—. 2010c, ApJ, 723, L223

Winn, J. N., Johnson, J. A., Marcy, G. W., et al. 2006, ApJ, 653, L69

Winn, J. N., Johnson, J. A., Narita, N., et al. 2008b, ApJ, 682, 1283

Winn, J. N., Johnson, J. A., Peek, K. M. G., et al. 2007b, ApJ, 665, L167

Winn, J. N., Noyes, R. W., Holman, M. J., et al. 2005, ApJ, 631, 1215

Wittenmyer, R. A., Endl, M., Cochran, W. D., et al. 2006, AJ, 132, 177

Wolf, A. S., Laughlin, G., Henry, G. W., et al. 2007, ApJ, 667, 549

Wolszczan, A. & Frail, D. A. 1992, Nature, 355, 145

Xue, Y., Suto, Y., Taruya, A., Hirano, T., Fujii, Y., & Masuda, K. 2014, ApJ, 784, 66

Young, A. T. 1967, AJ, 72, 747

Yu, L., Winn, J. N., Gillon, M., et al. 2015, ApJ, 812, 48

Zechmeister, M. & Kürster, M. 2009, A&A, 496, 577

Zhou, G., Bayliss, D., Hartman, J. D., et al. 2015, ApJ, 814, L16

Zhou, G. & Huang, C. X. 2013, ApJ, 776, L35

Zhou, G., Latham, D. W., Bieryla, A., et al. 2016a, arXiv:1605.01991

Zhou, G., Rodriguez, J. E., Collins, K. A., et al. 2016b, arXiv:1607.03512

Vita

Marshall Caleb Johnson was born and raised in the Jemez Mountains of northern New Mexico. After graduating from high school in Santa Fe, NM, in 2007, he enrolled at Wesleyan University in Middletown, CT, in the fall of 2007. During his time at Wesleyan he participated in two Research Experience for Undergraduates programs. First, he spent the summer of 2008 at Vassar College through the Keck Northeast Astronomy Consortium program, working under the supervision of Prof. Allyson Sheffield on spectroscopy of giant stars in the Milky Way's thick disk and halo to probe the structure of these components. Second, he spent the summer of 2009 at the MIT Haystack Observatory, working under the supervision of Dr. Lynn Matthews on H I 21 cm observations of the circumstellar envelopes of asymptotic giant branch stars. During the academic year he conducted research at Wesleyan, working under the supervision of Prof. Seth Redfield on photometric observations of transiting exoplanets. He spent the spring of 2010 as a visiting student at the University of St. Andrews. Marshall graduated from Wesleyan in May 2011 with a Bachelor of Arts degree in astronomy and physics, earning high honors in astronomy with his senior thesis.

Marshall enrolled in the graduate program in astronomy at the University of Texas at Austin in the fall of 2011, and earned his Master of Arts degree from the program in August 2013 under the supervision of Dr. William Cochran and Prof. Sally Dodson-Robinson. Since that time he has continued to work on Doppler tomography under the supervision of the now-Prof. Cochran, as well as on other projects with the McDonald Observatory Planet Search team and various collaborations following up planet candidates from *Kepler* and K2.

In the fall of 2016 Marshall will take up the Columbus Prize Fellowship as a postdoctoral fellow in the Department of Astronomy at the Ohio State University.

This dissertation was typeset using LaTeX by the author.